Order Number 9218233

Electrochemical studies: Gas phase environments; the response of microelectrodes with thin shielding; and composite polymers

Fang, Yun, Ph.D.

City University of New York, 1992

U·M·I
300 N. Zeeb Rd.
Ann Arbor, MI 48106

ELECTROCHEMICAL STUDIES: GAS PHASE ENVIRONMENTS; THE RESPONSE OF MICROELECTRODES WITH THIN SHIELDING; AND COMPOSITE POLYMERS

by

YUN FANG

A Dissertation submitted to the Graduate Faculty in Chemistry in partial fulfillment of the requirements for the degree of Doctor of Philosophy. The City University of New York.

1992

This manuscript has been read and accepted by the Graduate Faculty in Chemistry in satisfaction of the dissertation requirement for the degree of Doctor of Philosophy.

27 Jan 92 — Date
Johna Leddy — Chair of Examining Committee

11 Feb. 92 — Date
Richard Pizer — Executive Officer

Ronald L. Birke — Supervisory Committee

Stephen W. Feldberg — Supervisory Committee

The City University of New York

Abstract

ELECTROCHEMICAL STUDIES: GAS PHASE ENVIRONMENTS; THE RESPONSE OF MICROELECTRODES WITH THIN SHIELDING; AND COMPOSITE POLYMERS

by

Yun Fang

Supervising Professor: Johna Leddy

Three different topics of electrochemical interest are addressed in this dissertation.

I) *Electrochemistry in Gas Phase Environments*

Signals generated at electrode assemblies inserted into flasks containing solvent vapors were shown to arise from solvents adsorbed across the surface of the electrode assemblies. No electrolyte was added. The magnitude and nature of the voltammetric signal varied with the solvent properties. Hexane exhibited only a capacitive response. Electrolysis currents were generated in higher dielectric solvents. The magnitude of the voltammetric current decreased monotonically with decreasing solvent autoprotolysis and acidity constants. Crude estimates with Gouy Chapman Stern models and the Frumkin correction suggest the electrochemical signal arises from the electrolysis of the solvent ions as opposed to the solvent molecules.

II) *Simulation of Cyclic Voltammetric Responses at Inlaid Microdisks with Radii Comparable to the Shielding Thickness*

A simulation was developed for the response of inlaid microdisks embedded in an insulator of thickness comparable to the electrode radius. Here, flux from behind the plane of the electrode affects the cyclic voltammetric response. The exponential expanding grid was modified to

provide finer resolution across the electrode/insulator and insulator/solution interfaces.

A complete range of scan rates, electrode radii, and shielding thicknesses were examined. Conditions for steady state and the magnitude of the steady state current are present. Voltammetric wave shapes are discussed and a method for finding the electrode radius and insulator thickness is presented.

III) *Surface Diffusion as a Mechanism of Flux Enhancement in Composite Ion Exchange Polymers Formed by Absorption of Nafion into Neutron Track Etched Membranes*

The flux of organic cations and neutrals through composites formed by absorbing Nafion, a cation exchange polymer, into neutron track etched membranes, was found by steady state rotating disk voltammetry. The flux through the Nafion portion of the composites was found to be higher than the flux through simple Nafion films, and to increase as the diameters of the pores in the neutron track etched membranes decreased to $\geq$ 30 nm. A phenomenalogical model based on surface diffusion along the pore walls was proposed to account for the flux enhancement. The data were analyzed according to a simple equation which accounts for the ratio of surface area to volume in the pores. Flux along the walls was found to be higher than flux through the Nafion in the center of the pores.

Acknowledgments

I would especially like to express my appreciation to my thesis advisor, Dr. Johna Leddy, for her guidance and assistance in the preparation of this dissertation, and for her constant concern and encouragement during the entire period of my graduate study at the City University of New York.

I would also like to thank my committee members, Dr. Stephen F. Feldberg and Dr. Ronald L. Birke, who guided and helped me in finishing my thesis work with their experience, and Dr. David Locke, who helped me to perform the gas chromatography/mass spectroscopy experiments and guided me in the use of other instrumentation.

I extend my thanks to all my colleagues, especially Eugene Wolkow, who provided valuable assistance in my research as well as a nice atmosphere in the laboratory. Thanks to all the other members of the department who offered their assistance.

Very special thanks to my wife and best friend, Lili Zhou, for her patience, understanding, and encouragement during these years.

Finally, I would like to acknowledge the financial support of National Science Foundation, (CHE88-15936).

Dedicated to those who made this thesis possible:

My research mentor, my parents, my wife, and my son.

Table of Contents

Chapter		Page
	Introduction	1
I	Electrochemistry in Gas Phase Environments	
	1.1 Introduction	10
	1.2 Experimental	12
	1.3 Results and Discussion	20
	1.4 Summary	64
II	Cyclic Voltammetric Responses for Inlaid Microdisks with Shields of Thickness Comparable to the Electrode Radius: Simulation and Experiments	
	2.1 Introduction	65
	2.2 Experimental	68
	2.3 Theory	69
	2.4 Results and Discussion	78
	2.5 Summary	101
III	Surface Diffusion in a Microstructured, Ion Exchange Matrix: Nafion/Nuclepore Composite Membranes	
	3.1 Introduction	102
	3.2 Experimental	106
	3.3 Results	107
	3.4 Proposed Model	115
	3.5 Discussion	117
	3.6 Conclusion	125

Appendix A: The Constraints of Developing the Irregular Expanding Grid ---------- 128

Appendix B: The Fortran Simulation Program ---------- 130

Reference ---------- 140

Glossary ---------- 149

List of Tables

Table — Page

Chapter I

1. Dimensions and Insulator Resistances of the Electrode Assemblies as Determined by EDX Spectroscopy ---------- 15
2. Diffusion Coefficients of Some Solvents in the Gas Phase ----- 22
3. Solvent Resistances ---------- 34
4. Solvent Ionization Constants and Ion Concentrations ---------- 36
5. Standard Addition Results to Determine H_2O in Ethanol ------ 41
6. Amounts of Trace H_2O in Test Solvents as Determined by GC/MS ---------- 41
7. Ion Concentrations in Autoprotolytic Solvents ---------- 44
8. Parameters of Importance in GCS Theory ---------- 48
9. Maximum Current Found for Various Solvents and Insulators at a Scan Rate of 1V/s ---------- 55

Chapter II

1. Dimensionless Diffusion Coefficients Used in Irregular Expanding Grid Simulations ---------- 77
2. Values of Some Constants Used in the Simulation ---------- 78
3. Comparison of Dimensionless Peak Currents Calculated from the Regular EESG and Irregular EESG Methods for a Disk Electrode Embedded in a Semi-Infinite Insulating Shield ------ 79

4. Comparison of Resolution as a Function of the Number of Grid Elements, N_{ra}, Used for the Active Area of the Disk Electrode ---------- 80
5. The Coefficients in Equation 28 to Evaluate b/a and b-a ------- 98
6. Comparison of Experimental and Simulation Results -------- 100
7. Comparison of Experimental and Simulation Results -------- 100

Chapter III

1. Solution Parameters ---------- 109
2. Membrane Parameters ---------- 111
3. Values of $i_{comp}l/nFAc^{*}\varepsilon$: Extracted from the Intercepts of the Koutecky-Levich Plots ---------- 113
4. Results of Analysis According to Equation 9 ---------- 119

List of Figures

Figure — Page

Chapter I

1-1 Schematic Diagrams of Glass and Sandwich Microelectrode Assemblies ---------- 13
1-2 Energy Disperse X-ray Spectroscopy of Teflon Sandwich Assembly ---------- 17
1-3 Schematic Diagram of Experimental Measuring System ----- 18
1-4 Three Possible Mechanisms for the Reaction of a Gas Phase Molecule at the Electrode Surface ---------- 21
1-5 Time Dependence of the Voltammetric Response of Aniline --- 24
1-6 Maximum Current as a Function of the Amount of Ethanol and Water Introduced ---------- 28
1-7 Crude Model for Approximating the Thickness of the Adsorbed Solvent Layer ---------- 30
1-8 GC/MS of Water in Ethanol ---------- 40
1-9 Voltammetric Responses as a Function of Scan Rate for Ethanol and Aniline ---------- 50
1-10 Voltammetric Responses as a Function of Scan Rate for Water and Acetonitrile ---------- 53
1-11 The Cyclic Voltammetric Response of Hexane ---------- 55
1-12 Maximum Current Responses as a Function of Autoprotolysis and Dielectric Constants ---------- 56
1-13 Cyclic Voltammograms for a Saturated Mixture of Ethanol and Aniline ---------- 59

Chapter II

2-1 Schematic Diagram of the Disk Electrode Used in Simulation -- 70
2-2 Schematic Diagram of the EESG Used in the Simulation ---- 73
2-3 Diagram of Concentration Profiles for Various Transport Regimes ---------- 83
2-4 Cyclic Voltammograms for Various Cases ---------- 85
2-5 Comparison of Simulated Cyclic Voltammograms for the Hemisphere and the Semi-Infinite Shielded Disk Electrodes ---------- 89
2-6 The Effect of the Ratio of Shielding to Disk Radii on the Dimensionless Peak Current ---------- 91
2-7 The Effect of the Ratio of Shielding to Disk Radii on $\Delta E_{1/2}$ ---- 92
2-8 The Relationship Between the Dimensionless Steady State Current and the Ratio of Disk to Shielding Radii ------- 94
2-9 Working Curve for the Prediction of the Radius of the Disk Electrode and the Shielding Thickness ---------- 96

Chapter III

3-1 Schematic Diagram of the Proposed Model of Flux Through the Pores of the Nafion/Nuclepore Composites ----- 105
3-2 Plot of the Intercepts of the Koutecky-Levich Plots as a Function of Log(d) ---------- 114
3-3 Plots of $i_{comp}l$ /nFAc*ε versus d^{-1}, According to Equation 10 ---------- 122

INTRODUCTION

This thesis discusses three different projects: electrochemistry in a gas phase environment; the simulation of the cyclic voltammetric responses of inlaid microdisks with shields of thickness comparable to the disk radii; and the effects of surface diffusion in the enhancing flux through ion exchange composites formed by sorbing Nafionn (Registered Trade Mark, DuPont) into neutron track etched membranes (Registered Trade Mark, Nuclepore). As these three projects have different background and history, each will be discussed separately.

Electrochemistry in Gas Phase Environments

It is always of interest make electrochemical measurements in unique media. In place of the normal electrolyte solutions,' electrochemists have made measurements in such unusual media [1] as solids, polymers without solvents, and frozen solutions. Bond, Fleischmann and Robinson [2] studied electrochemical reaction in frozen solutions using microelectrodes.

Studies have been done in gas phase environments. Murray and coworkers [3-5] coated electrode assemblies with thin layers of ionically conducting polymers. Molecules introduced into the gas phase partitioned into the polymer layers and were electrolyzed. Although some of these systems contained solvent vapor, no bulk solvent was present. Cook, et al., [6,7] described the reduction of gas phase carbon dioxide at high surface area metal electrodes coated on a Nafion membrane. Most hydrogen/ oxygen, solid polymer electrolyte fuel cells run under conditions where the anodes are fairly dry and hydrogen is present in the gas phase at the electrode surface. [8-10]

Recently, microelectrodes have been used to detect molecular species in

the gaseous effluent of a gas chromatograph. Pons and coworkers [11,13] used a microelectrode device to replace the thermal conductivity detector. The electrode potential was held at a high value, the current response correlated with the flow of gaseous effluent over the electrode surface. For a variety of species, the sensitivity of the microelectrode detector was many fold greater than that of a thermal conductivity detector. These measurements were possible because the microelectrodes can be used in highly resistive media, such as those associated with a gas phase environment, where there is neither electrolyte nor solvent.

However, these studies challenged traditional notions of electrochemistry and raised many questions as to the nature of electrochemistry in a gas phase environment. What supplies ionic contact between the electrodes? Is the electrochemical signal due to electron transfer or is it strictly a capacitive effect? Is a molecule actually present in the gas phase when it undergoes electrolysis or is it sorbed on the electrode surface? What is the relationship between the signal magnitude and the nature of reactant species?

The first chapter details the construction of special microelectrode assemblies and their use in various solvent vapors to address the above questions about the nature of electrochemistry in a gas phase environment. The microelectrode assembly consisted of an 8 μm diameter carbon fiber, the cross section of which served as the working electrode, embedded in a polymeric insulator which separated it from larger counter electrodes by approximately 10 μm. The counter electrode was a pair of gold band electrodes, one band on either side of the working electrode. Several different insulating materials were used: polystyrene, polyethylene, teflon, parafilm and glass. The glass electrode was formed by pulling a glass capillary around the carbon fiber and the counter electrode was then a conductive painted ring around the glass insulator.

The experimental studies were undertaken in a flask first evacuated to 10^{-5} torr. A few microliters of electroactive species were then injected. The

concentration could be varied up to saturation of the gas phase by introducing varying volumes of the electroactive species.

Three different physical mechanisms are considered for the generation of electrochemical signals in a gas phase environment. These are electrolysis of the electroactive species directly from the gas phase; adsorption of the electroactive species on the surface of the electrode assembly to from a solvent layer in which the electroactive species is then electrolyzed; and absorption of electroactive species into the polymeric insulator where the polymeric insulator acts as a solvent in which the adsorbed electroactive species is electrolyzed. The results show the adsorption of the solvent on the surface of the electrode assembly is necessary to generate an electrochemical signal and to maintain ionic contact between the electrodes through disassociation reactions of the adsorbed solvent. The magnitude of the electrochemical signal is shown to be dependent on the characteristics of solvent. The Gouy Chapman Stern model of the double layer was used to provide a qualitative description of the double layer in these systems of low ionic concentrations. The model is also shown to fail catastrophically for voltage perturbations of greater than a few tenths of a volt.

Simulation of Cyclic Voltammetric Responses for Inlaid Micro-Disk Electrodes with Shield of Thicknesses Comparable to the Electrode Radius

In the second chapter, the development of a simulation for the cyclic voltammetric response of inlaid microdisk electrodes with shields of thickness comparable to the electrode radius is presented. The development includes a modification of an exponential expanding spatial grid [14] to allow the grid to expand, contract and expand again. The results of the simulation were verified by comparison with experimental voltammetric responses of microelectrodes with different shielding thicknesses.

Microelectrodes have several advantages over larger electrodes [1]. As

the electrode radius becomes smaller, its perimeter increases relative to its area. This leads to enhanced radial (edge) diffusion, and thus, to higher mass transport rates than that observed for linear diffusion. The steady state flux associated with radial diffusion enhances the faradaic current. Capacitive or non-faradaic currents, on the other hand, decrease with increasing electrode area. Because the currents at microelectrode are small, voltage drops due to solution resistance are minimized. Reduced capacitive currents and ohmic losses, as well as the rapid onset of steady state current, make micro-electrodes an ideal choice for investigating electrochemical reaction mechanisms, both heterogeneous and homogeneous kinetics. The advantages are most pronounced when the kinetics are too rapid to be measured at traditional, larger electrodes.

Inlaid microdisk electrodes are the most commonly employed electrodes because they are most easily constructed [15-16]. Typically, electrodes are made by either drawing a glass capillary down around an electrically conducting fiber or dip coating the fiber in a polymeric insulator [17-19]. With these methods of construction, the thickness of the insulating shield and the radius of the disk are comparable.

When the electrode radius and the shield thickness are comparable, flux from behind the plane of the electrode will enhance the steady state current and reduce the time required for the electrode to reach steady state. Under steady state, Nernstian conditions, the shape of the cyclic voltammogram and the magnitude of the steady state current are determined by the ratio of the electrode radius and the shielding thickness. Thus, the interpretation of voltammetric responses at microelectrodes is complicated by both transitions from linear to radial diffusion and the relative size of the electrode and its shield.

Drawing on knowledge of polarographic response, electrochemists often interpret the voltammetric responses of microdisks using the current expected for spherical and hemispherical electrodes as the Nernstian

responses of these systems are parameterized by simple analytic expressions. Oldham and coworkers [20-22] successfully derived analytical equations to calculate the steady state current for several different electrode shapes, including the inlaid disk electrode. From these expressions, the steady state disk current for a semi-infinite shield is $4/\pi$ times the steady state current. However, the effects of shield thickness were not considered in these derivations. Amatore, Wightman and coworkers [23-24] used conformal mapping to predict the steady state current of inlaid disks under limiting cases of shielding thickness. For larger inlaid disks where the insulating shield is not large compared to either the electrode radius or the diffusion length generated during the course of the sweep, the approximation of the hemispherical current is limited.

Voltammetric responses for traditional electrodes are well characterized for a variety of electrode geometries, common voltammetric perturbations, and assorted conditions of chemical and electrode kinetics [25]. In these cases, the edge effect is not usually substantial because radial diffusion caused by the edges does not contribute substantially to the flux on the time scale of most transient measurements. As the edge flux becomes comparable to the total flux, as it usually does on the time scale of measurement of most inlaid microdisks, several questions are generated. First, how does the thickness of the insulating shield influence the voltammetric response? Second, how is steady state recognized at an inlaid microdisk? Third, how can the disk radius and the shield thickness be estimated from the voltammetric response? Last, what are the limitations of using the spherical approximation to interpret the voltammetric response of inlaid disk electrodes?

Chapter II presents a computer simulation for the effect of shield thickness on the cyclic voltammetric response of an inlaid microdisk. The simulation is a two dimensional, finite difference simulation in cylindrical coordinates. As the system is symmetric in the angular coordinate, cylindrical coordinates reduces the simulation to a two dimensional problem.

Expanding spatial grids [14,16] are employed in both the axial and radial coordinates. This dramatically reduces the computation time. As the edge effects are substantial in this system, two interfaces become pivotal. These are the electrode/insulator and insulator/solution interface. A non-uniform exponential grid was used to provide finer grids across these interfaces, which, in turn, improved the resolution and accuracy of the simulation. The method for defining this non-uniform grid is presented and its results compared with those of the uniform, exponential grid.

The simulation quantifies the effect of the ratio of disk radius to the shield thickness on the steady state and transient response. A method is presented to determine the radius of the electrode and the shield thickness from experimental results. The simulation results were evaluated by comparing the simulated results with the experimental signals generated at microdisks with various shielding thicknesses.

Effects of Surface Diffusion in Enhancing the Flux through Composite Ion Exchange Polymers Formed from Nafion and Neutron Track Etched Membranes

The development of systems with controlled chemical architecture has been an area of interest for the last several years. In these systems, the goal is to engineer devices with dimensions ranging from submicron to those approaching molecular. Efforts along these lines include the charge separation devices of Mallouk and coworkers [27-29]. Wrighton and coworkers [30,31] have been detailing the individual steps necessary for the construction of electronic devices with dimensions just slightly larger than molecular. Because of their small dimensions, molecular electronics would both speed computations and increase the density of stored information. Kulesza and Faulkner [32-33] have been working in the area of micro-structured matrices on electrodes. Many devices and systems can also be

envisioned which are engineered to capitalize on the small dimensions of the ultramicroelectrodes that electrochemists are now able to build.

In these systems, the focus has been on how to build small structures and how to shuttle electrons in a structured matrix where the molecular species are immobilized. If notions of systems with controlled chemical architecture are to be extrapolated to their limit, dynamic microstructured devices will be developed. That is, in addition to switches and electron collectors, microstructured chemical reactors will be considered. Such reactors have the additional complexities of arranging facile, selective transport of desired reactants and products through the microstructured matrix.

In Chapter III, a microstructured system is described which can serve as a prototype and model system for the design of selective, molecular pipes with facile transport. The system is formed by adsorbing Nafion (DuPont), a perfluorinated, sulfonic acid ion exchange polymer, into the straight, cylindrical pores of Nuclepore membranes [34]. The membranes are available commercially with diameters of 15, 30, 50, 80, 100 and 600 nm. The flux of cations and neutrals through these composites can be monitored by steady state, rotating disk voltammetry. The selectivity of these composites is governed by Nafion while the surface of the pore walls provides a zone of facile transport.

In all microstructured systems, as structures decrease in size, the ratio of surface area to volume increases. Thus, processes which are not important in bulk systems may come to play a major role in dictating the behavior of microstructural systems. The interfacial processes which are likely to be effective in microstructural systems are those which generate a steep, but short range gradient at the interface. Examples include electrostatic effects, migration, magnetic gradients, surface tension and surface diffusion. In designing microstructured transport systems, these interfacial effects can be capitalized on to build systems of rapid and selective transport.

For pores of 30 nm or greater, it was found that the flux through the

pores of the Nafion/Nuclepore composites increased as the diameter of the pores decreased. It is proposed that this increase in flux is due to surface diffusion along the pore walls of the Nuclepore support. Nafion acts as an extraction matrix, which concentrates cations within the pores. Transport rates in Nafion are relatively slow (of the order of 10^{-8} to 10^{-10} cm^2/s). If transport along the pore walls is more facile than transport in Nafion, then the following can be envision as a description of the environment within the composites. The concentration of ions near the wall will be depleted more rapidly than in the Nafion in the center of the pore. This will create a concentration gradient which will drive the redox species to move radially to the wall, where they are rapidly shuttled along the wall to the electrode by surface diffusion. Thus, the flux enhancement in these composites is a two component process: Nafion increases the concentration of cations by partitioning redox species into the pores and effective transport is supplied as surface diffusion along the pore walls of the Nuclepore support.

Based on this description, two things can be anticipated. First, that transport through the Nafion portion of the composites is more rapid than transport through a simple Nafion film. This is observed. Second, as the pore size shrinks, a diameter must be found where the volume of Nafion which extracts cations is optimized for the pore surface area available for surface diffusion. This is also observed. A phenomenalogical description of this combination of partitioning and surface diffusion is presented to model the experimental system. Some notions are outlined about what can be done to optimize transport and selectivity in these composites and in similar systems where surface diffusion plays a role. Interfacial gradients are pointed out as a unique asset of microstructural systems. With cleverness, interfacial effects can be capitalized upon to engineer tailored transport and selectivity into systems with controlled chemical architecture.

Appendices

Two Appendices are also included. Both relate to the simulation of the voltammetric response of inlaid microdisks. The formulas for generating the non-uniform exponential grids used in the radial coordinate to account for edge effects at the electrode/insulator and insulator/solution interfaces are summarized in Appendix A. Appendix B lists the Fortran program used to calculate the cyclic voltammograms for microdisks with semi-infinite and finite shielding lengths.

Chapter I

Electrochemistry in a Gas Phase Environment

1.1 INTRODUCTION

Recently, Pons and coworkers [1-3] used microelectrodes to detect molecular species in the effluent of a gas chromatograph. They termed the process "gas phase electrochemistry". Others have also used electrochemical techniques to examine system where at least one of the molecular components is present in the gas phase. Murray and coworkers [4-6] coated electrode assemblies with thin layers of ionically conducting polymers, such as poly(ethylene oxide). Molecules introduced into the gas phase partitioned into the polymer layers and were electrolyzed. Although some of these systems contained solvent vapors, no bulk solvent was present. Cook, et al., [7-8] described the reduction of gas phase carbon dioxide at high surface area metal electrodes coated on a Nafion membrane. Most hydrogen/oxygen, solid polymer electrolyte fuel cells run under conditions where the anodes are fairly dry and hydrogen is present in the gas phase at the electrode surface [9-11].

These studies raise some interesting questions as to the possibilities and limitations of electrochemistry in a gas phase environment. First, where is the molecule when it generates an electrochemical signal? Is the molecule present in the gas phase, adsorbed on the electrode surface or absorbed into the insulator between the electrodes? Second, how is ionic contact maintained between the electrodes? Third, in any electrochemical measurement, ions are needed to carry charge between the two electrodes, establish and maintain the interfacial potential, and compensate any charge generated during electrolysis. What is the source of ions? Fourth, is the electrochemical signal due to electrolysis or simple capacitive effects? Fifth,

what is the nature of the double layer and how does it influence the electrochemical response? Sixth, when electrolysis occurs, what is electrolyzed? To address some these questions, a cyclic voltammetric study of aqueous and organic solvent vapors was undertaken with microelectrodes. The results are briefly outlined as follows.

1) Adsorption of the solvent on the surface of the electrode assembly is necessary to generate an electrochemical response.

2) Ionic contact is maintained between the electrodes through disassociation reactions of the adsorbed solvent.

3) Ion concentration is determined by the disassociation reactions of the solvent. These reactions are classified as autoprotolysis, acid-base reactions with no autoprotolysis, and non-disassociation. If the solvent is able to undergo autoprotolysis, the ion concentration is roughly that generated by autoprotolysis alone, independent of the acid or base properties of the solvent. If the solvent cannot undergo autoprotolysis but it can be protonated by water and other protic impurities, then the majority of the ions in the system arise from protonation of the solvent by protic impurities. If the solvent is inert, ions arise only from impurities on the surface and in the bulk of the insulator.

4) Electrochemical signals for solvents which can be ionized by either autoprotolysis or acid-base reactions are due to heterogeneous electron transfer; in the absence of large concentrations of impurities, inert solvents generate a simple capacitive response.

5) Electrolysis signals are largest for species which are able to generate the most ions; the response is limited by the supply of available ions.

6) Gouy Chapman Stern (GCS) models of the double layer are limited to a qualitative description of potential profiles in low electrolyte systems.

7) Despite the low concentration of ions in pure solvents, GCS theory and the Frumkin correction show the ions to be likely candidates for electrolysis. Solvent ions may contribute more to the electrolysis current

than the neutral solvent molecules.

A more detailed discussion of these points follows.

1.2 EXPERIMENTAL

1.2-1 Chemicals

The solvents used as redox species in the gas phase environment include ethanol (EtOH), acetonitrile (ACN), aniline (ø-NH_2), hexane and dimethyl sulfoxide (DMSO). With the exception of ethanol (AAPER, Alcohol and Chemical Co.), all solvents were purchased from Fischer Scientific Co. All non-aqueous solvents were dried over 4Å molecular sieves. Water was purified through a Milli-Q, QM-140 (Millipore Corp.).

1.2-2 Electrode Assemblies

The microelectrode assemblies used in this study were two electrode systems. The working electrode was a carbon fiber microdisk, approximately 8 μm in diameter. The combination counter-reference electrodes were gold layers. The working and counter-reference electrodes were separated by insulators of various thicknesses. The insulating materials included glass, polyethylene, teflon, parafilm, and polystyrene. Two different types of electrode assemblies were constructed: sandwich assemblies and glass micropipet assemblies.

Glass insulated assemblies were constructed of micropipets, as shown in Figure 1-1a. A carbon fiber was inserted into a 5 μl micropipet (Becton Dichinson Co.). Vacuum was pulled on the end of the pipet and the mid section of the pipet was heated in a Bunsen burner flame. The vacuum (approximately 10^{-3} torr) enhanced the constriction of the glass around the carbon fiber. As the glass constricted, the fiber was well-sealed in the softened glass. By cutting through the constriction, perpendicular to the carbon fiber, two disk electrodes were formed. Diameters of the electrode

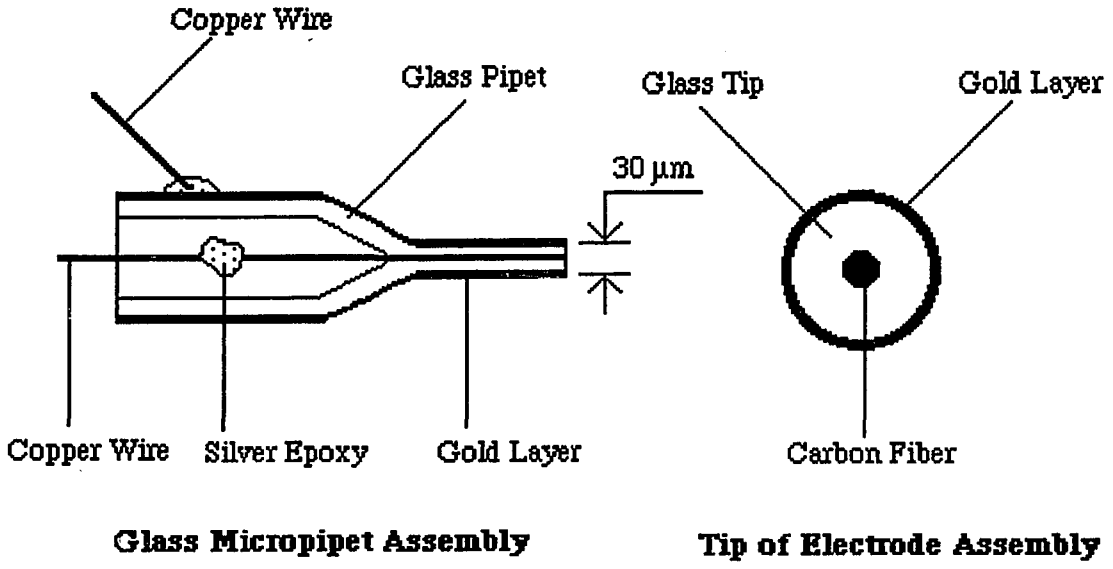

Figure 1a

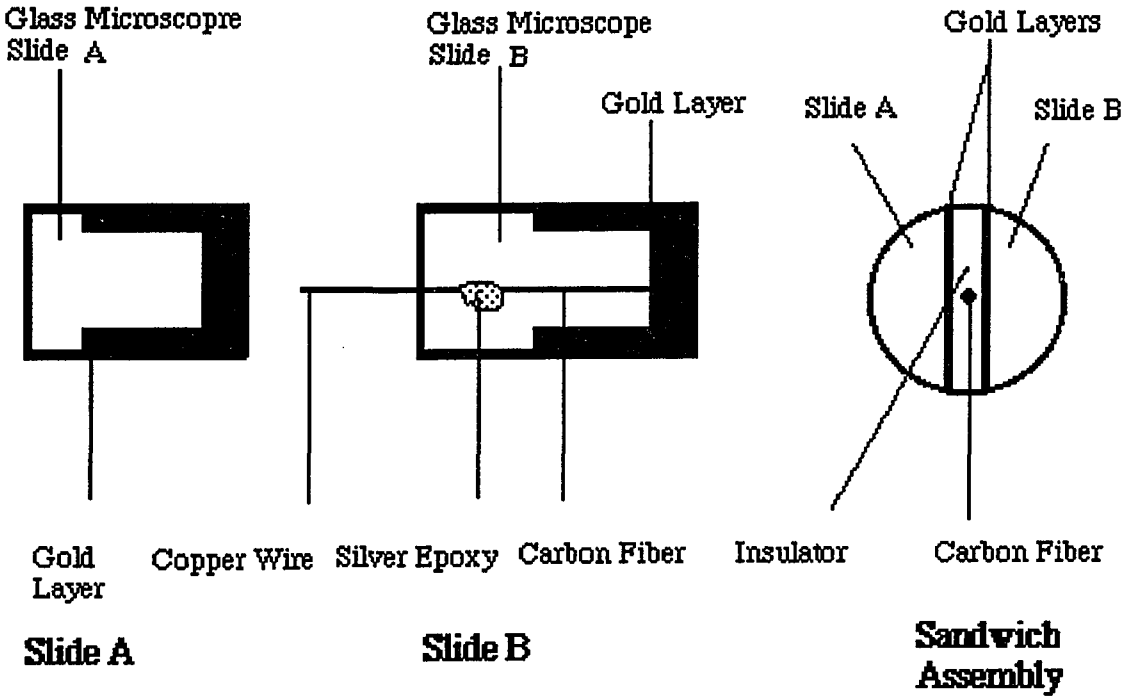

Figure 1b

Figure 1-1: Schematic Diagrams of Glass (Figure 1a) and Sandwich (Figure 1b) Microelectrode Assemblies.

assembly tips ranged from 30 to 60 μm. Bright Brushing Gold (AESAR, Johnson and Mattey Co.) was painted, as shown in Figure 1a, on the outer capillary surface, and dried with a heat gun at 400 to 500 °C for five minutes. The resulting gold layer, approximately 2 μm thick, served as the combined counter-reference electrode. Connection was made to the carbon fiber working electrode with silver epoxy (AESAR, Johnson Matthey Co.) and a fine copper wire. Another connection was similarly made to the gold counter-reference electrode. The electrode assembly was washed and cleaned with distilled water and acetone, and dried at 100 °C for two hours. The active surface of the assembly is shown on the right in Figure 1-1a.

Sandwich assemblies were constructed with various insulators: polyethylene, teflon, parafilm, and polystyrene. A schematic of the sandwich assembly is shown in Figure 1-1b. Two glass slides (Microscope Slides, Fisher Scientific) (1.0 x 2.0 x 0.15 cm; 1.0 x 1.5 x 0.15 cm) were painted with Bright Brushing gold, as shown for Slides A and B in Figure 1-1b, and then heated with a heat gun to form conductive layers, which served as counter-reference electrodes. A layer of insulating material was then applied to both glass sliders, and a carbon fiber was placed between the insulating layers to form a sandwich. Parafilm was dissolved in toluene. This solution was painted on both glass slides which had been placed in a vacuum dessicator (10^{-3} torr) for 2 hours. A carbon fiber was placed between the slides and the sandwich was closed. The polystyrene insulator electrode assembly was made in the same way as the parafilm assembly. The polyethylene insulator was made by heating the polyethylene polymer (high density) to the almost molten state, and then paint on to the glass slides. Before painting the slides, the carbon fiber is placed in the middle of the slides. The teflon insulator electrode assembly was made by putting teflon tape on the surface of the glass slides. Then the carbon fiber was put in the middle of the two slides, and a moderate pressure was applied. The active surface of the electrode assembly is shown in the rightmost diagram of Figure 1-1b. The working electrode

carbon disk is separated from the gold band counter-reference electrodes by the insulator. The dimensions of the assemblies were determined by energy dispersive x-ray spectroscopy, and are summarized in Table 1. Connections were made to the carbon working electrode and the two gold counter-reference electrodes with silver epoxy and copper wires. The assembly was polished with sandpaper of successive grits 300 to 600, and 0.05 μm alumina (Buchler, Ltd.). Before use, the electrodes were cleaned with distilled water and acetone, and dried in a vacuum desiccator for at least 12 hours.

Table 1: Dimensions and Insulator Resistances of the Electrode Assemblies as Determined by Energy Dispersive X-ray Spectroscopy

	Insulator Materials		
	Teflon	Polyethylene	Parafilm
Distance between Counter Electrode (μm)	30	28	32
Diameter of Carbon Fiber (μm)	8	8	8
Distance from Counter Electrode to Edge of Carbon Fiber (μm)	11	10	12
Thickness of Counter Electrodes (μm)	2	2	2
Resistance (Ω)	9×10^{11}	2×10^{11}	4×10^{10}

All microelectrodes were tested cyclic voltammetrically in acetonitrile solutions of 2 mM ferrocene and 0.1 M tetrabutyl ammonium tetrafluoroborate. Solutions were degassed with dry, presaturated nitrogen. Only electrodes which have been well sealed and give the anticipated sigmoidal response at reasonably slow scan rates were used in these studies.

The electrode dimensions were determined by scanning electron microscopy and energy dispersive x-ray spectroscopy performed on Hitachi S-570 scanning electron microscope. A typical spectrum is shown in Figure 1-2. The peaks correspond to the signal generated by the gold bands on either side of the electrode assembly. The distance between the maxima of the two peaks corresponds to the distance between the two bands, 30 μm. The width of the peaks at the half height is consistent with the gold layer thickness of 2 μm. The gaps between the working electrode and counter-reference electrodes were approximately 10 μm, and the ratios of counter to working electrode areas were roughly 640. The counter-reference electrodes in the sandwich assemblies were 2 μm x 8 mm.

1.2-3 Apparatus and Measurements

The measurement vessel was a one liter round bottom flask equipped with several ground glass joints to allow insertion of the electrode assembly, vacuum outlet, sample injection inlet and thermometer. The flask and electrode leads were mounted inside a Faraday cage to minimize electrical noise. See Figure 1-3. The flask was evacuated to $5x10^{-5}$ torr with a vacuum diffusion pump coupled to a piston pump. Test species were introduced into the evacuated flask with an oven dried microliter syringe. Except as noted, all measurements were made at room temperature.

Cyclic voltammetric and potential step experiments were performed with a potentiostat (Model 176, Princeton Applied Research Co.) and wave form generator (Model 175, Princeton Applied Research Co.). The signal

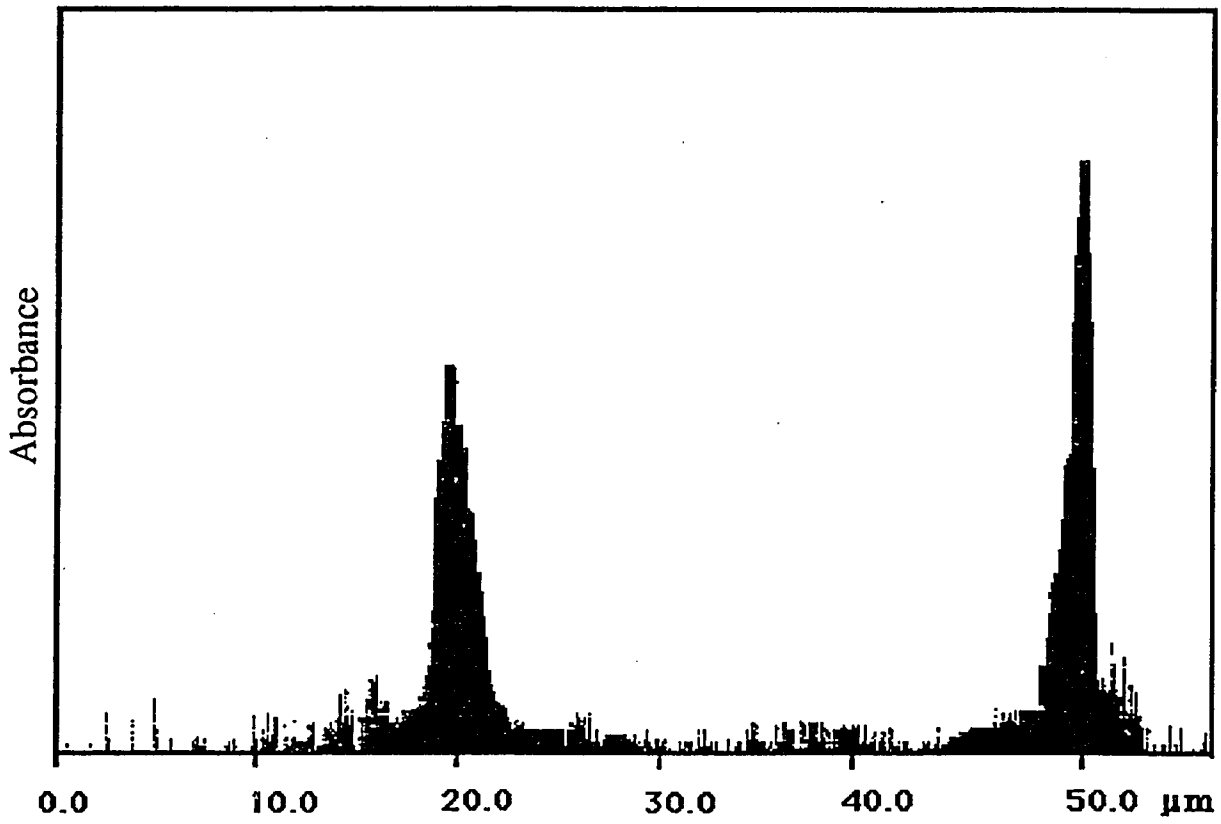

Figure 1-2: Energy Dispersive X-Ray Spectroscopy of Teflon Insulator Sandwich Microelectrode. The peaks correspond to the signal generated by the gold bands on either side of the electrode assembly. The distance between the maxima of the two peaks corresponds to the distance between the two bands, 30 µm. The width of the peaks at the half peak height is the thickness of gold layer, 2 µm.

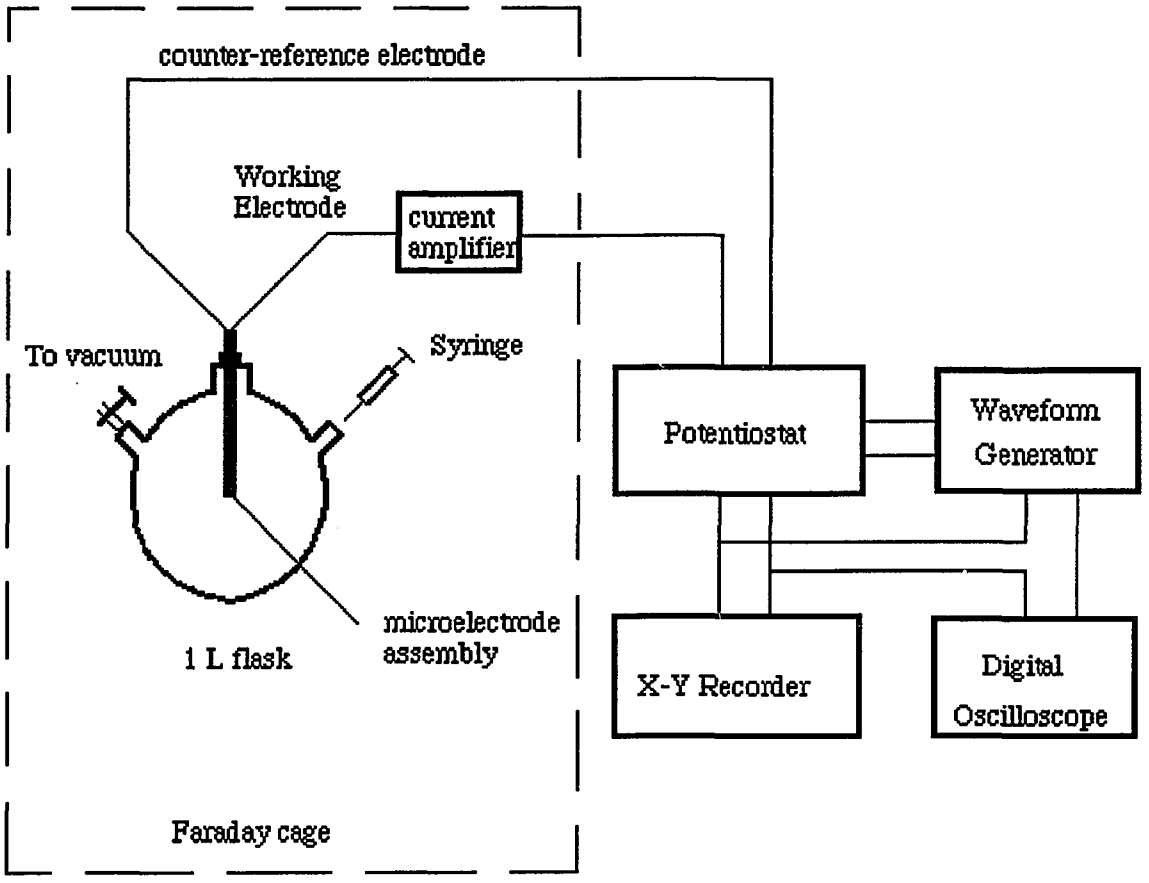

Figure 1-3: Schematic Diagram of the Experimental Measuring System.

was amplified with a current multiplier built according to the procedure of Huang, et al., [12]. The noise level was ± 2 pA. Results were recorded with both a chart recorder (Soltec VP-64245) and digital oscilloscope (Norland Corp.).

The trace water in each solvent was determined by gas chromatography/mass spectroscopy (MS: Model 88, GC: Model 5890. HP 5988A. Hewlett Packard Corp.). The operating conditions will be discussed in details in the following section.

1.3 RESULTS AND DISCUSSION

Several issues relevant to electrochemical measurements in a gas phase environment are addressed in this section. The problem is broken down into three parts. First, various experimental evidence is presented to demonstrate that the matrix for conduction between the electrodes is an adsorbed solvent layer. Second, the effects of ionic concentration on the electrochemical response are described. Ion generation through solvent disproportionation reactions is discussed. The correlation between the experimental results and the ion generating capacities of the adsorbed solvents are presented. Third, the nature of the electrochemical signal is considered. Electrochemical responses associated with both electrolysis and simple capacitive responses are expected. When sufficient ions are present to allow electrolysis, the nature of the electrolyzed species, ion or neutral solvent molecule, is considered.

1.3-1 The Role of Adsorption

Important to the characterization of electrochemistry in a gas phase environment is determining where the molecule is when it generates an electrochemical signal. There are three possibilities, as illustrated in Figure 1-4. The molecule may interact with the electrode surface directly from the gas phase. (Figure 1-4a) It may exist as a condensed layer, adsorbed on the surface of the electrodes and insulator. (Figure 1-4b) Or, the molecules may be absorbed from the gas phase into the bulk of the insulator, where the insulator serves as a bulk solvent. (Figure 1-4c) Systems of this type have been studied by Murray and coworkers [4-6].

Gas and Condensed Phases: Electrochemical signals generated by molecules in the gas phase can be differentiated from condensed molecules based on the more facile transport of gaseous species. Diffusion coefficients

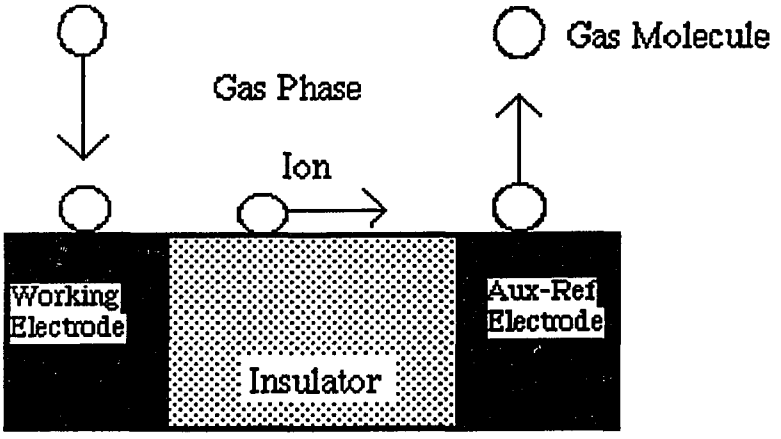

Figure 4a

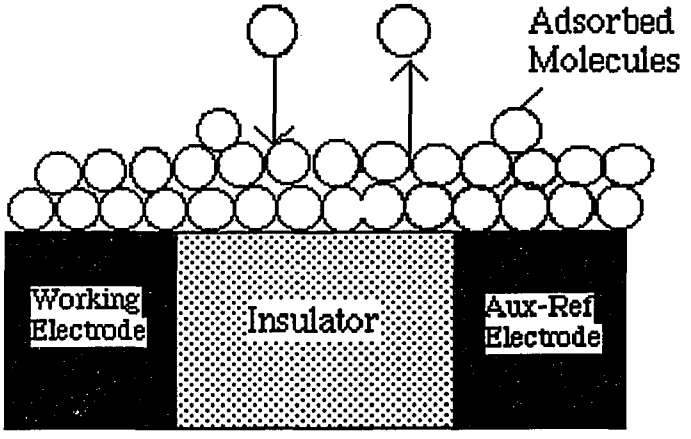

Figure 4b

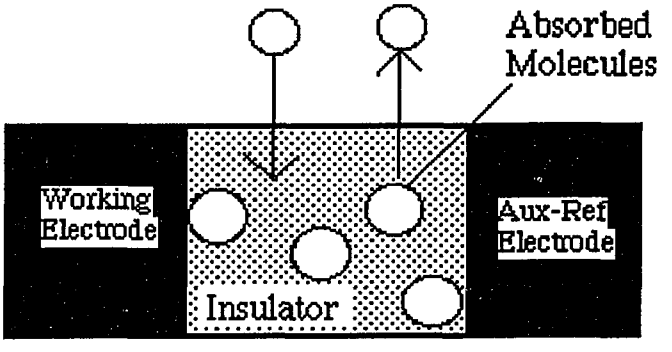

Figure 4c

Figure 1-4: The Three Possible Mechanisms for the Reaction of a Gas Phase Molecule at the Electrode Surface.

in the gas phase are roughly 0.2 cm^2/s, which is four to five orders of magnitude higher than liquid phase values. See Table 2.

Consider a redox active species introduced into the gas phase 2 cm from the electrode surface. It will take roughly 10 seconds for gaseous molecules to reach the electrode surface at 1 atm. of pressure. (For a diffusion length, δ = 2 cm, and a diffusion coefficient, D = 0.2 cm^2/s, the time for diffusion, $t = \delta^2/2D$.) If the electrochemical response is generated by molecules present in the gas phase, the response should be observed within a few seconds of introducing the electroactive species. Lag times greater than several seconds are indicative of sorption phenomena. In addition, for signals generated by species present in the gas phase, a steady state electrochemical response should be reached rapidly. The time required to reach steady state is the same as the time required for the molecules to become uniformly distributed within the reaction vessel.

Table 2: Diffusion Coefficient of Some Solvents in the Gas Phase at 1.0 atm. Pressure [14]

	H_2O	EtOH	ACN
Diffusion Coefficient (cm^2/s)	0.239	0.137	0.129
Temperature (^0C)	8.0	40.4	38.5

To determine if the electrochemical signal is generated by molecules as they collide with the electrode surface directly from the gas phase, the

following experiment was performed. A teflon sandwich assembly was suspended 2 cm above the bottom of an evacuated, 1 L round bottom flask. The cyclic voltammetric response for this electrode, recorded in vacuum at 1 V/s for a range of + 9.0 to - 9.0 V, is shown in Figure 1-5a. The voltammogram exhibits simple resistive-capacitive characteristics. At time, t = 0 s, 100 μl of aniline were introduced as a condensed liquid into the bottom of the flask. Cyclic voltammograms were recorded continuously at 1 V/s for a range of + 9.0 to - 9.0 V. These results are shown in Figure 1-5 b-g. The signal after one minute (Figure 1-5b) was difficult to distinguish from background (Figure 1-5a). After four minutes, there was a discernible increase in current (Figure 1-5c). The signal increased several orders of magnitude over the next hour, at which time the current stabilized (Figure 1-5g). Such behavior is consistent with sorption of the aniline either on the surface of the electrode assembly or into the insulator. If the molecules were present in the gas phase when they generated the electrochemical signal, the signal should be large and stable within a few seconds of introducing the molecular species. As this is not observed, sorption is important to the observed electrochemical signals. Further evidence for a sorption is provided by the total lack of electrochemical response observed when strictly gaseous species such as air, H_2, N_2, He and C_3H_3 are introduced into the flask.

Adsorption and Absorption: Two sorption mechanisms are possible: adsorption onto the electrode surface (Figure 1-4b) and absorption into the insulating layer (Figure 1-4c). To differentiate the contribution of each to the electrochemical signal, several experiments were undertaken. In the first experiment, the stable electrochemical signal, shown in Figure 1-5g, was perturbed by rapidly heating the flask. The electrochemical signal returned to background (Figure 1-5a, h) immediately. On cooling, the stable signal, shown in Figure 1-5g, was regenerated. Heating and cooling allowed the voltammetric response to be cycled between the background and stable responses. The rapid desorption is consistent with surface adsorbed layers.

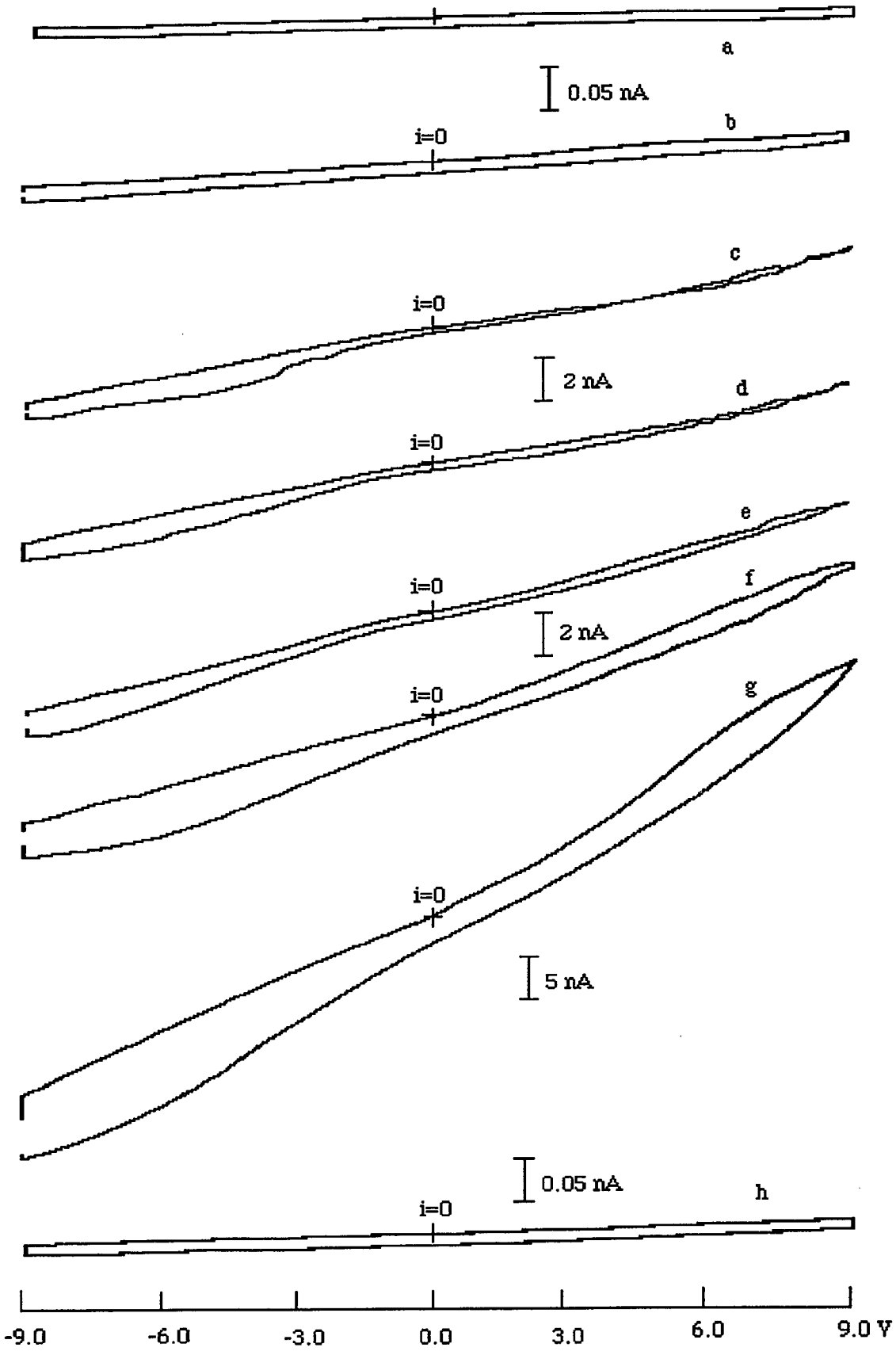
a
0.05 nA
b
i=0
c
i=0
2 nA
d
i=0
e
i=0
f
2 nA
i=0
g
i=0
5 nA
0.05 nA
h
i=0
-9.0
-6.0
-3.0
0.0
3.0
6.0
9.0 V

Figure 1-5: Time Dependence of the Voltammetric Response of Aniline. All cyclic voltammograms were recorded with a teflon sandwich assembly at 1 V/s over a potential range of +9.0 to -9.0 V. The system was first evacuated for one hour at the pressure of $5x10^{-5}$ torr. The zero point current is marked on each voltammogram.

a: The background response, recorded before any aniline was introduced.

b-g: 100 μl of aniline were introduced at time, t=0 s. b-g were recorded at successive times, (b): 1 min.; (c): 4 min.; (d): 6 min.; (e): 12 min.; (f): 25 min. and (g): 50 min., respectively. The voltammogram was stable after 50 min., as shown in Figure 1-5g.

h: The voltammetric response after five minutes of evacuation, or after the system was heated for a few minutes.

The desorption is driven by the increase in vapor pressure with temperature.

Similar results were observed for ethanol. In a second experiment, the stable, room temperature response of Figure 1-5g was perturbed by evacuating the flask. The signal observed after 5 minutes of evacuation is shown in Figure 1-5h. This signal is the same as that recorded in vacuum before any sample was introduced (Figure 1-5a). Again, the rapid desorption of aniline is consistent with surface adsorption of aniline. In the third experiment, absorption was precluded by using a glass insulator. The electrochemical signal was generated by the adsorbed aniline.

Absorption was evaluated by allowing the electrode to sit in a flask containing aniline vapor for two days. The resulting electrochemical signal was of substantially lower resistance, and the current was roughly one hundred-fold higher than that observed in Figure 1-5g. The flask was again evacuated. It required over four hours to remove the aniline and return the electrochemical response to background (Figure 1-5a). The time scale for absorptive behavior is dramatically different than the adsorptive behavior shown in Figure 1-5g. All these observations are consistent with the electrochemical signal being generated by aniline adsorbed on the surface of the electrodes assembly. All the following measurements were made within a time frame which precludes extensive absorption.

Concentration Dependence: The need for adsorption is also evident when the current response is evaluated as a function of the gas phase concentration of the redox species. If molecules are electrolyzed directly from the gas phase, the observed current should scale linearly with the concentration of gaseous redox molecules. If adsorption is critical to the observed electrochemical response, the current will not scale linearly with the concentration of gaseous redox molecules. There will be no electrolysis signal until the surface coverage has reached some critical, minimum value, where the adsorbed molecules bridge the gap between the electrodes, and are, thereby able to support a current. Short of saturation of the vapor with

redox material, the surface coverage is proportional to the volume of redox material added to the flask because of the equilibrium between the gaseous and adsorbed molecules.

In this experiment, a small amount of ethanol (10 μl) was introduced into an evacuated one liter flask. After allowing the electrochemical signal to stabilize, the maximum current at approximately +7.0 V was recorded. Another small sample of ethanol was then injected, and the procedure repeated. A plot of the observed current as a function of the total amount of added ethanol is shown in Figure 1-6a. No current above background was observed until at least 45 μl of ethanol were added to the flask. The current then increased with added ethanol until the vapor was saturated with ethanol, at approximately 200 μl of added ethanol. (200 μl is in good agreement with the 171 μl calculated for a one liter flask and a vapor pressure of 54.24 torr at 298 K.). The sigmoidal curve is consistent with an electrochemical signal being generated once sufficient ethanol has adsorbed on the surface of the electrode assembly to support a current. Results for a similar experiment on water are shown in Figure 1-6b. For the vapor pressure (23.76 torr) of water at 298 K, the vapor will be saturated with water when 74.9 μl of water have been injected. This correlates well with the 85 μl observed for water. The volumes where saturation is observed are probably slightly higher than the calculated volumes because the joints on the flask make the volume slightly larger than one liter. The ratios (200/171=1.17 and 85/74.9=1.13) are similar.

Adsorption on the Insulator: Adsorption on the insulator as well as on the electrode also plays a role in the electrochemical response. Electrochemical studies similar to those presented in Figure 1-5 for aniline were done using different insulators: teflon, polyethylene and glass. The times for the onset of discernible current correlate with how easily each of the insulators are wet. A steep contact angle is indicative of poor wetting while a small contact angle is associated with effective wetting. The contact

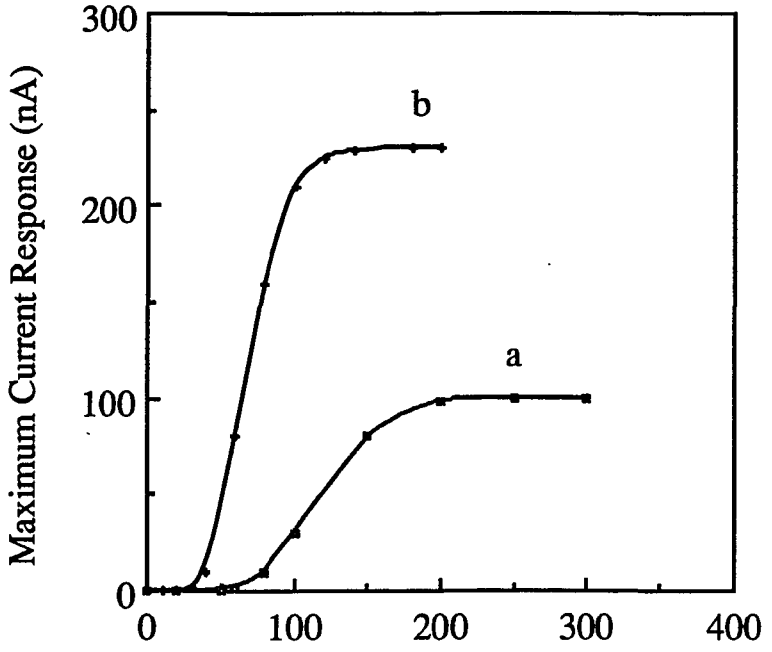

Figure 1-6: Maximum Current as Functions of the Amount of Ethanol and Water Introduced into the one liter Flask.

(a): The maximum stable current was recorded for volumes of ethanol (20 to 300 µl) added to a one liter flask. The maximum current as taken from voltammograms recorded with a teflon insulated sandwich, at 1 V/s, + 9.0 to - 9.0 V. No current above background was observed until the added volume of ethanol exceeded 45 µl. This is consistent with adsorption as a necessary step in current generation. Maximum current, recorded at greater than 200 µl, correspond to saturated ethanol vapor.

(b): The maximum stable current recorded for volumes of water (10 to 210 µl) added to a one liter flask. Other conditions were the same as (a). No current above background was observed until the added volume of water exceeded 35 µl.

angles for aniline, water and ethanol were roughly 90° on teflon. Glass was well wet by all three; polyethylene exhibited moderate contact angles. The onsets of discernible current were most rapid on glass and least rapid on teflon. Adsorption of the electroactive species on the insulator as well as the electrode is necessary to the generation of an electrochemical signal.

Amount of Adsorbed Material: Solvent may adsorb on the surface of the electrode assembly at monolayer or multilayer coverage. At monolayer coverage, two things are expected. First, the energetics of the insulator surface will govern the adsorption process up to saturation of the surface and maximum current. Second, for adsorption of non-interacting species on a two dimensional surface, no conduction will occur until surface coverage has reached 45% of a monolayer, as predicted by percolation theory [13]. The experimental evidence points to greater than monolayer coverage. For all solvents, the limiting current is set by the saturation of the vapor with solvent. The energetics of the insulator surface only determine the onset of discernible current. Also, the onset of discernible current for ethanol, as shown in Figure 6a, occurs at 45 μl of added ethanol. Based on percolation theory, if 45 μl occurs at 45 % of a monolayer, then the limiting current would be reached at approximately 100 μl. The maximum current occurs at 200 μl which corresponds to saturation vapor pressure and greater than one monolayer coverage. Similarly, the onset of current for water occurs at about 30 μl. If this corresponds to the onset of conduction through a partial monolayer, then percolation theory predicts monolayer coverage at about 65 μl. Saturation occurs at 85 μl. Again, suggesting greater than monolayer coverage. Given the following considerations, the thickness of the adsorbed solvent layer was crudely approximated. For the glass insulator electrodes, illustrated in Figure 1-7a, the distance, l, between the working and counter-reference electrode is small (approximately 10 μm). r_0, the electrode radius (approximately 4 μm), is comparable to l. When a potential sufficient to electrolyze solvent is maintained between the electrodes for a

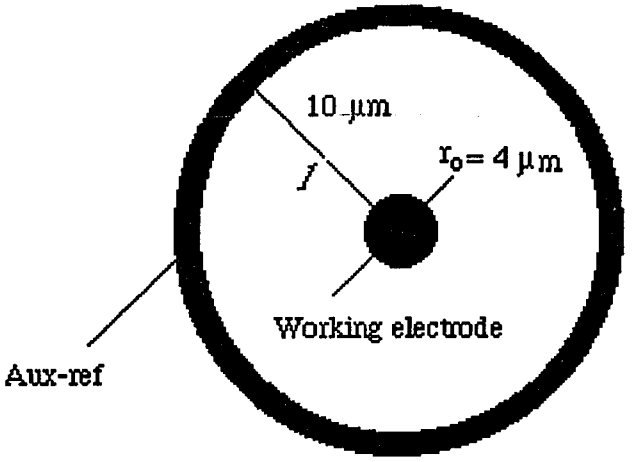

Figure 7a

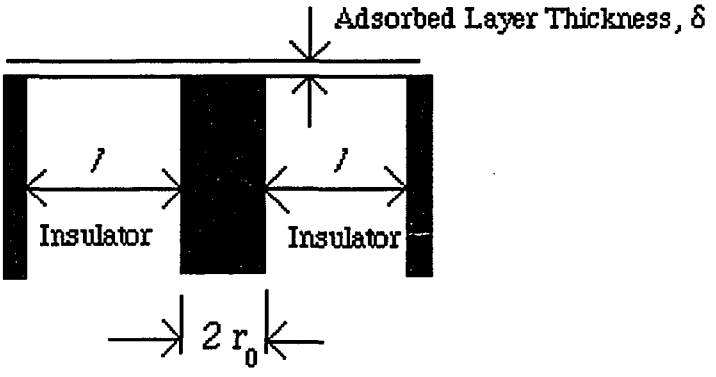

Figure 7b

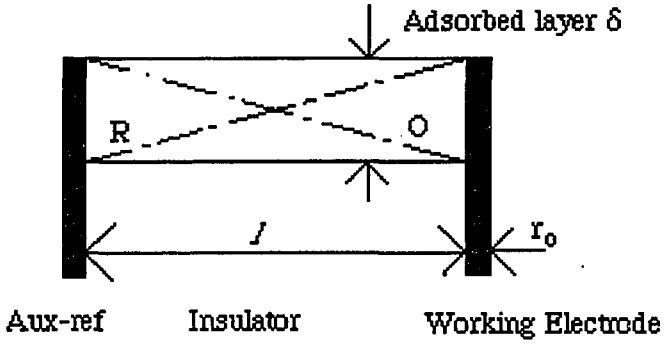

Figure 7c

Figure 1-7: Crude Model for Approximating the Thickness of the Adsorbed Solvent Layer.

Figure 7a illustrates the geometry for the glass capillary electrode. The working electrode has a radius, r_0, of 4 μm, separated by the insulator from the auxillary-reference electrode (aux-ref) by a distance, *l*, of 10 μm.

Figure 7b shows a cross section (perpendicular to the surface of the electrode) of the electrode with an adsorbed solvent layer of the thickness, δ.

Figure 7c: Under the assumptions discussed in the text, the mass transport limited electrolysis under steady state feedback between the working and auxillary-reference electrodes can be modeled as electrolysis in a planer thin layer configuration where the electrode area is $2\pi r_0\delta$. In Figure 7c, the model version of the left half of Figure 2b is shown. The dotted line is the steady state concentration profile of the electrolyzed species, O and R.

long enough period, a feedback situation develops between the electrodes and a steady state current, i_{ss}, arises. The solvent is adsorbed across the surface of the electrode assembly, as illustrated in Figure 1-7b, at a thickness, δ. Assume that when $l < 3r_0$, the radial effect is negligible. Also, allow that when $\delta << r_0$, all electrolysis is at the outer edge of the disk, and the area for electrolysis is well approximated by $2\pi\delta r_0$. This reduces the problem to a linear gradient between two electrodes of area $2\pi\delta r_0$, separated by a distance l. This is illustrated in Figure 1-7c. The appropriate equation is

$$i_{ss} = \frac{2nF\pi D\delta r_o c_b^*}{l} \qquad [1]$$

where c_b is the bulk solvent concentration. For 200 µl of injected ethanol, ethanol, i_{ss} = 7.5 µA for a step from 0 to + 6.0 V at a glass electrode. c_b = 0.017 moles/cm^3 and r_0 = 4 µm. For coverage above a monolayer, n of 1 and D = 5 x 10^{-6} cm^2/s, δ is the order of 30 to 200 nm from Equation 1. This is a very crude estimate of the adsorbed layer thickness because of the approximations involved in developing Equation 1 and the rough estimates of the diffusion coefficient. Give the estimate of the thickness and ethanol molecules of 4 Å, the adsorbed layer thickness is approximated as 5-100 adsorbed layers.

Conduction of the Insulator and Adsorbed Solvent Layer: For electrodes used in a gas phase environment, there are two parallel mechanisms for maintaining ionic contact between the electrodes. These are conduction through the insulator and conduction through species adsorbed on the surface of the insulator. The inherent conduction of the insulator may be either a bulk or surface conduction process. Short of producing a plasma, ionic contact cannot be supplied through the gas phase. Measurements were made to differentiate between the inherent conduction of the insulator and conduction through surface adsorbed species.

The inherent conduction of the insulator was evaluated by

voltammetric measurements made in vacuum. A cyclic voltammogram is shown in Figure 1-5a for a teflon insulator electrode. The cyclics for all insulating materials exhibited similar characteristics: high resistance and low capacitance. Resistances were calculated from slopes of the current-voltage curves for three insulators. The resistances, summarized in Table 1, were of the order of 10^{10} to 10^{11} Ω, and varied with insulator and insulator thickness.

The conduction of an adsorbed layer was measured at equilibrium surface coverage of the sorbed material. Ethanol, water, DMSO, and aniline were studied. The vapor was saturated with the species of interest and a stable voltammetric response was recorded, as in Figure 1-5g. By measuring the slope of the current-voltage curves in a zone where there is no electron transfer behavior, the resistance of the absorbed layer was determined. See Table 3. The resistances varied with the adsorbed solvent, and, with the exception of water, scaled with the known resistance of the bulk solvent. As shown in Table 3, the resistances of the adsorbed solvents were three to six orders of magnitude lower than the inherent resistance of the insulators. Of the two parallel paths of conduction between the working and counter electrodes, conduction through the adsorbed solvent layer is markedly more efficient than conduction through the insulator. In the presence of these adsorbed solvents, the conduction of the insulator contributes negligibly to maintaining ionic contact between the electrodes.

1.3-2 The Influence of the Ion Concentration in the Adsorbed Layer

It has been established that the solvent is adsorbed on the surface of the electrodes. In the absence of adventitious impurities and trace water, the adsorbed solvent serves as the source of ions. The ions generated by the solvent serve several purposes. First, the ions complete the electrochemical circuit by providing charge carriers between the two electrodes. Second, the solvent ions and dipoles establish and maintain the interfacial potential and

Table 3: Solvent Resistance

	Solvent			
	H_2O	EtOH	ACN	ϕ-NH_2
Resistance[a] (Ω)	$5x10^7$	$1x10^8$	$8x10^8$	$4x10^9$
Bulk solvent Resistance[b] (Ω)	$1x10^{10}$	$2x10^9$	$2x10^8$	$2x10^9$

a) Resistances were determined with a teflon insulator sandwich assembly from a cyclic voltammogram taken between -0.5 and +0.5 V, at a scan rate of 0.05 V/s.

b) Values approximated from Reference [20] based on the teflon sandwich electrode with 36 nm thickness of the adsorbed layer.

double layer. Third, if sufficient interfacial potential is established to drive an electron transfer reaction, the solvent must provide the necessary ions to compensate the charge generated during the electrolysis. Fourth, the ions as well as the neutral solvent molecules serve as potential electroactive species.

In the following, solvent reactions, such as autoprotolysis and acid-base reactions, are identified as major sources of ions. Solvent properties critical to characterizing ion concentrations are discussed. Effects of trace water are also considered. The nature of the double layer in low electrolyte systems, its influence on the electrochemical response, and the critical solvent parameters are discussed.

Time constants: As the ionic conductivity drops, the response time of the system to a voltage perturbation increases. This characteristic time, or time constant, is expressed as the product of the double layer capacitance and the solution resistance. In the solvents studied here, all the measured capacitances range from 1 to 4 x 10^{-11} F. These values are high and relatively invariant, which suggests the capacitance is associated with the cables rather than the electrode solution interface. Experimentally determined solvent resistance are cited in Table 3. Ethanol (R = 100 MΩ) has a time constant of roughly 1 ms; aniline (4 GΩ) has a value of 45 ms. These values are larger than those encountered in electrolyte solutions. Thus, the response time of these systems to a voltage perturbation will be longer.

Source and Concentration of Ions in Pure Protic Solvents: Ions are generated by disproportionation reactions of the solvent. In a dry, protic solvent, HS, the principal reaction of this type is autoprotolysis,

$$2HS \rightleftharpoons H_2S^+ + S^- \qquad [2]$$

which is characterized by the autoprotolysis constant, $K_{auto}=[H_2S^+][S^-]$. In the absence of added electrolyte and adventitious impurities, the total concentration of cations or anions in the solvent, c*, will be $c^* = K_{auto}^{1/2}$. In

Table 4, pK_{auto} and c* are listed for several solvents. Values of pK_{auto} are not listed for aniline and hexane as neither undergoes significant auto-protolysis.

Table 4: Solvent Ionization Constants and Ion Concentration

	Solvent					
	H_2O	EtOH	ACN	DMSO	ϕ-NH_2	C_6H_{14}
pK_{auto}	14.0	19.1	28.5	33.3		
$c_b = K_{auto}^{1/2}$ (M)	$1x10^{-7}$	$2.8x10^{-10}$	$5.6x10^{-15}$	$2.2x10^{-17}$		
c_b (M)	55.5	17.1	19.1	14.0	11.0	7.65
ε	78.5	24.3	36.0	46.7	6.89	1.86
$pK_{a,HS}$		20.2[a]				
$pK_{b,HS}$		17.9[b]	26.2[c]	33.6[d]		
$pK_{a,H2O}$	15.7	18[e]	25[e]	35.1	25[e]	44[e]
$pK_{b,H2O}$	15.7	16[e]	24[e]		9.4	

a) Reference [15].
b) Reference [16] and [17].
c) Reference [18-19].
d) Reference [21].
e) Reference [22].

Under normal electrochemical conditions, the electrolyte is maintained at roughly a 100-fold higher concentration than the redox species. This insures adequate ions are present to sustain the electrode reaction and the redox species is restricted to diffusive transport. In a pure solvent, the concentration of ions is low, as discussed above. In addition, a likely electroactive moiety is the neutral solvent molecule. The molar concentration of the solvent, c_b, calculated from the density and molecular weight, is listed in Table 4. It is immediately obvious that the concentration of ions is much below the concentration of the neutral solvent, and that the normal electrochemical condition of a large ratio of electrolyte to redox moieties is reversed. Thus, the voltammetric response can be restricted, and, even dictated, by the supply and motion of ions.

Source and Concentration of Ions in Organic Solvents with Trace Water: In the presence of trace adsorbed water and other proton sources, a second method of generating ions is present. Ions can be generated by acid-base reactions of the adsorbed solvents with the trace impurities. The importance of these reactions in increasing ionic conductivity depends, first, on whether the solvent undergoes autoprotolysis, and, second, on the extent of reaction between the impurity and the adsorbed solvent. As will be shown later, the magnitude of the currents observed on different insulators varied little. This suggests the insulators and electrode materials are not major sources of ionic impurities. The rest of the discussion will focus on trace water in the solvents as the major source of ionic impurities. If the impurity is trace water, the disassociation processes involve acid-base reactions of trace water in bulk organic solvent. The two main reactions are as follows.

$$HS + H_2O \rightleftharpoons H_2S^+ + OH^- \qquad [3]$$

$$HS + H_2O \rightleftharpoons S^- + H_3O^+ \qquad [4]$$

These reactions are characterized by acidity and basicity constants for water in the bulk organic solvent, denoted here as $K_{a,HS}$ and $K_{b,HS}$, respectively. These are defined as

$$K_{a,HS} = \frac{[H_2S^+]\,[OH^-]}{[H_2O]} \qquad [5]$$

$$K_{b,HS} = \frac{[S^-]\,[H_3O^+]}{[H_2O]} \qquad [6]$$

If the analytic concentration of water is C_{H2O}, and x and y are, respectively, the concentrations of hydroxide and hydronium ions generated in the acid and base reactions, then these can be expressed as

$$K_{a,HS} = \frac{x^2}{C_{H_2O} - x} \qquad [7]$$

$$K_{b,HS} = \frac{y^2}{C_{H_2O} - y} \qquad [8]$$

Organic solvents are generally less able to support substantial ion concentrations than water, as reflected in their lower dielectric constants and polarities. See Table 4. Given the lower ion concentrations, a reasonable approximation is $C_{H2O} \gg x, y$. Then,

$$x \approx [K_{a,HS}\, C_{H_2O}]^{\frac{1}{2}} \qquad [9]$$

$$y \approx [K_{b,HS}\, C_{H_2O}]^{\frac{1}{2}} \qquad [10]$$

In general, values of $pK_{a,HS}$ and $pK_{b,HS}$ are not known for a wide range of solvents. For the solvents studied here, a few values are listed in Table 4.

Disassociation constants for organic solutes in bulk water are more commonly known. K_a and K_b are defined as

$$K_a = \frac{[H_3O^+][S^-]}{[HS]} \qquad [11]$$

$$K_b = \frac{[OH^-][H_2S^+]}{[HS]} \qquad [12]$$

In principle, $K_a/c_b(H_2O)$ and $K_{b,HS}/c_b(HS)$ are equal and provide a mechanism for calculating $K_{b,HS}$ from K_a. Similarly, $K_b/c_b(H_2O)$ should be equal to $K_{a,HS}/c_b(HS)$. However, because of differences in the dielectric properties and polarizability of the solvents, attempts to estimate the disassociation constants of trace water in the organic solvents from the acid and base constants for the organic in bulk water yield values of $K_{b,HS}$ and $K_{a,HS}$ which are, in general, too high. Note in Table 4, $K_{a,H2O} > K_{b,HS}$; similarly, except for DMSO, $K_{b,H2O} \geq K_{a,HS}$. Thus, in the absence of values for $K_{b,HS}$ and $K_{a,HS}$ approximations can be made using K_a and K_b. However, the K_a and K_b values will be high by as much as several orders of magnitude. So, for example, if K_a and K_b were substituted for $K_{b,HS}$ and $K_{a,HS}$ in Equations 9 and 10, then the values calculated for x and y would, in general, be too high.

Concentration of Trace Water in the Test Solvents: Given Equations 9 and 10, any discussion of the concentration of ions generated by reactions with trace water will depend on the concentration of water in the solvents, C_{H2O}. The concentration of water in the test solvents was determined by GC/MS. The operational conditions are listed in the chromatogram shown in Figure 1-8 for water in EtOH. Mass fragments from 16 to 18 were collected. The amount of water was determined by standard addition of water to EtOH. Primary data are shown in Table 5. Linear regression of these data yields:

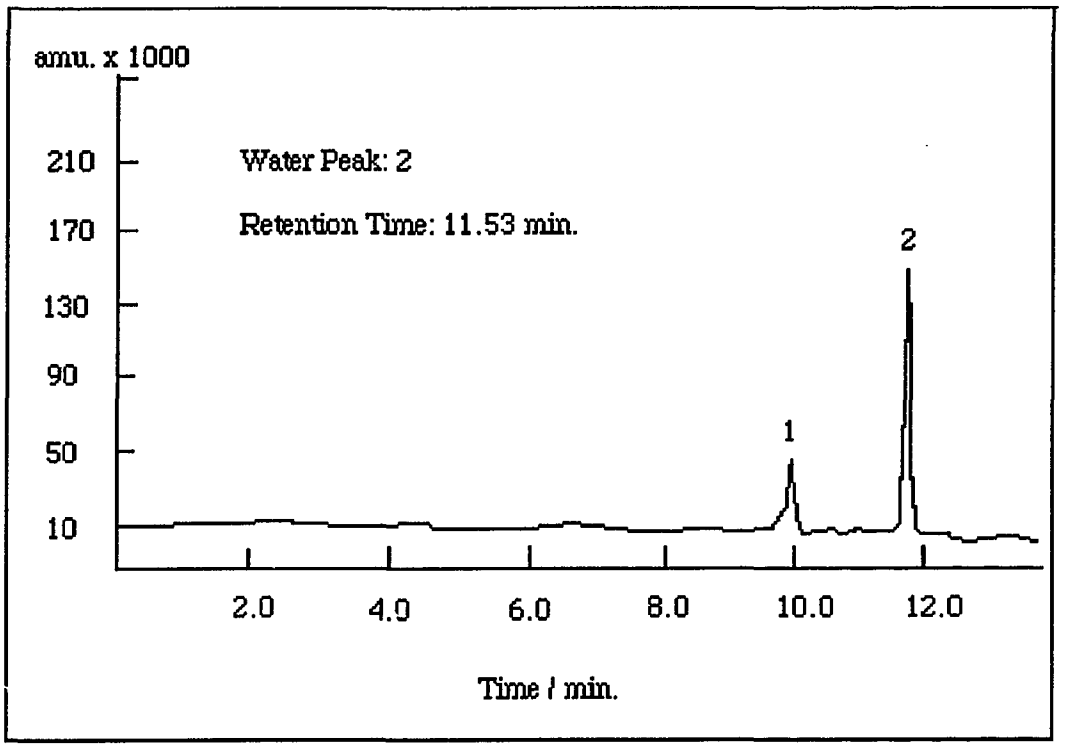

Figure 1-8: GC/MS Chromatogram of H_2O in Ethanol.

GC/Mass Operating Conditions:

Sample: 0.4 µl of H_2O/ml of EtOH. Injection Vol.: 0.5 µl split injection.

Mass: Collected fragments: 16, 17, 18.

Source temp.: 270 °C. Analyzer temp.: 150 °C.

GC Column temp.: 35-100 °C. Temp. grad.: 10 deg./min.

Peak 2 is the H_2O peak, identified by standard addition of H_2O. Peak 1 is an unknown species.

Table 5: Standard Addition Method to Determine H_2O in Ethanol

	H_2O added in ethanol (µl/ml)			
	0.0	0.4	1.0	2.0
Signal of H_2O peak area	1.7×10^5	5.5×10^5	1.9×10^6	3.6×10^6

$$\text{Signal} = 1.78 \times 10^6 \times [\mu l \text{ of added } H_2O/ml \text{ of solvent}] + 4.38 \times 10^4$$

correlation coefficient = 0.994 [13]

For this plot, the x intercept is the negative of the concentration of water in EtOH. This is reported in Table 6. Equation 13 can be modified to determine the concentration of water in the other solvents. The results are summarized in Table 6. In all cases except DMSO, the concentration of trace water was below 1.4 mM. In non-polar hexane, the concentration was difficult to determine as the method was approaching the detection limit. The limit of detection is 0.1 ppm.

Table 6: Amounts of Trace H_2O in Test Solvents Determined by GC/MS

	EtOH	ACN	ø-NH_2	DMSO	C_6H_{14}
H_2O (ppm)	< 25	< 11	< 25	< 110	< 0.14
C_{H2O} (M)	$< 1.4 \times 10^{-3}$	$< 8.1 \times 10^{-4}$	$< 1.4 \times 10^{-3}$	$< 8.1 \times 10^{-3}$	9.3×10^{-6}

Concentration of Ions Generated in the Solvents by Trace Water: In the following, the relative importance of the acid-base reactions in enhancing the concentration of ions in each system will be discussed. Organic solvents fall into three categories: autoprotolytic; not autoprotolytic but able to undergo acid-base reactions with the trace water; and inert. The importance of the acid-base reaction in contributing to the ion concentration of each class will be considered in turn.

1) Autoprotolytic: Autoprotolytic solvents necessarily undergo acid-base reactions. The question is whether the acid-base reactions with trace water substantially increases the concentration of ions in an autoprotolytic solvent. As indicated in the autoprotolytic reaction shown in Equation 2, the concentration of ions generated by autoprotolysis, $c^* = K_{auto}^{1/2}$. The concentration of ions generated by acid-base reactions are x and y, as defined in Equations 9 and 10. The concentration of water at which the values of x and y are greater than or equal to c^* are:

$$C_{H_2O} \geq \frac{K_{auto}}{K_{a,HS}} \qquad [14]$$

$$C_{H_2O} \geq \frac{K_{auto}}{K_{b,HS}} \qquad [15]$$

To address the question of whether acid-base reactions with trace water substantially enhance the ion concentration in autoprotolytic solvents, the values calculated for C_{H_2O} must be compared to the experimentally determined values listed in Table 6. Values calculated for C_{H_2O} are listed in Table 7. Where values of $K_{a,HS}$ and $K_{b,HS}$ are known, C_{H_2O} values are listed. Table 7 also contains values calculated with K_{b,H_2O} and K_{a,H_2O}. As discussed previously, this calculation will underestimate the value of C_{H_2O} at which the number of ions generated by acid-base reactions will equal those

generated by autoprotolysis. For ease of comparison, the Table 7 also lists c^* and the experimentally determined values of C_{H_2O}.

The calculated values of C_{H_2O} are the critical concentrations of trace water at which the ions generated by acid-base reactions are equal in number to the ions generated by autoprotolysis. First, note higher critical concentrations are calculated using $K_{a,HS}$ and $K_{b,HS}$ than K_{a,H_2O} and K_{b,H_2O}, with the exception of DMSO. Second, note the experimentally determined values of C_{H_2O} are all less than the critical values calculated using $K_{a,HS}$ and $K_{b,HS}$. This means the majority of the ions arise from autoprotolysis, not acid-base reactions. The critical values calculated using K_{a,H_2O} and K_{b,H_2O} are comparable to the experimentally determined C_{H_2O}, but this reflects the underestimate of C_{H_2O} expected with the aqueous acidity and basicity constants.

In the lower portion of Table 7, the concentrations of ions generated by autoprotolysis and the acid-base reactions at the experimentally determined concentration of trace water, C_{H_2O}, are listed. In each case, the concentration of ions generated by autoprotolysis outstrips the acid-base reactions. In summary, for trace water dissolved in autoprotolytic solvents at concentrations below $K_{auto}/K_{a,HS}$ and $K_{auto}/K_{b,HS}$, the concentration of ions generated by acid-base reactions will be less than or equal to the concentration of ions generated by autoprotolysis of the bulk solvent. When the solvent contains a small fraction of water, the total number of ions present will still be comparable to the number generated by autoprotolysis. Thus, acid-base reactions with trace water will not dramatically increase the concentration of ions in autoprotolytic solvents.

2) Not Autoprotolytic But Able to Undergo Acid-Base Reactions: The only solvent we have studied in this class is aniline. Aniline is aprotic, and, therefore, unable to autoprotolyze. However, aniline can act as a weak base (pK_{b,H_2O}= 9.4), and, as such, may exhibit a significant enhancement of ion concentration through acid-base reactions in the presence

Table 7: Ion Concentrations in Autoprotolytic Solvents

	Solvent		
	EtOH	ACN	DMSO
Experimentally Determined C_{H2O} (m)	$< 1.4x10^{-3}$	$< 8.1x10^{-4}$	$< 8.1x10^{-3}$
$C_{H2O} \approx K_{auto}/K_{a,HS}$ (m)	12.6		
$C_{H2O} \approx K_{auto}/K_{b,HS}$ (m)	0.063	$5x10^{-3}$	2.00
$C_{H2O} \approx K_{auto}/K_{b,H2O}$ (m)	$8x10^{-4}$	$3.2x10^{-4}$	
$C_{H2O} \approx K_{auto}/K_{a,H2O}$ (m)	0.08	$3.2x10^{-5}$	63
$c^* = K_{auto}^{1/2}$ (m)	$2.8x10^{-10}$	$5.6x10^{-15}$	$2.2x10^{-17}$
$x = [K_{a,HS}\ C_{H2O}]^{1/2}$	$< 3.0x10^{-12}$		
$y = [K_{b,HS}\ C_{H2O}]^{1/2}$	$< 4.2x10^{-11}$	$< 2.3x10^{-15}$	$< 1.4x10^{-18}$

of a proton donor, such as water. The $pK_{a,H2O}$ of aniline is approximated at 25, so the reaction of aniline with trace water to generate H_3O^+ is expected to contribute relatively little to the total ion concentration.

As the $K_{a,HS}$ for water in aniline is not known, the ion concentration in this solvent can only be approximated using $K_{b,H2O}$. As discussed previously, $K_{a,HS}$ is expected to have a lower value than $K_{b,H2O}$ because of the lower dielectric constant of aniline. So, $x \leq [K_{b,H2O} C_{H2O}]^{1/2}$ where, from Table 6, the experimentally determined value of C_{H2O} is less than 1.4 mM. $x \leq 0.74$ μM. Because of the low dielectric constant of aniline (ε = 6.89), there will be substantial ion pairing, and the free ion concentration will fall below this. However, the estimated ion concentration is actually greater than the values for any of the autoprotolytic solvents.

Pons and coworkers [1-3] cite disassociation through acid-base reactions of molecules with adsorbed water as a major source of ions in their gas chromatographic system. In the systems studied here, the amount of adsorbed water is minimized, although not completely eliminated, by evacuating the reaction flask for approximately an hour before any solvent is introduced.

3) Inert: Inert, aprotic species, such as hexane, cannot generate ions by either autoprotolysis or acid-base reactions. Even in the presence of added electrolyte, the ion concentration in the highly non-polar, low dielectric (ε = 1.86) solvent will support few free ions. In addition to the extremely low concentration of water ($\leq$ 9 μM) found in hexane, ion concentrations in this solvent will be extremely low.

These discussions of ion concentration are central to describing the nature of the voltammetric response. The ions establish the double layer, and, thus, the electric field at the electrode surface. It is the potential at the electrode surface which determines the nature of the voltammetric response. A discussion of the relationship between the double layer and the ion concentration follows.

The Nature of the Double Layer: It is difficult to have a clear picture of what is occurring in a low electrolyte system during cyclic voltammetric perturbations because many things are changing simultaneously. During electrolysis, the few ions present in solution are committed to doing many things (i.e., establish and maintain the double layer, compensate charge generated during electrolysis, and carry charge across the bulk of the solution) and, as a result, the potential experienced by molecules in the vicinity of the electrode is difficult to characterize. It is this potential which determines the magnitude and nature of the voltammetric response.

The Stern modification of Gouy-Chapman (GCS) theory [23-25] affords a static picture of the potential profile at the electrode surface. Application of GCS theory to a system without added electrolyte is at best qualitative. Here, the equations appropriate to a planar electrode will be used, although the disks under consideration are in transition between linear and radial responses during the time of interest. All will be developed assuming the only source of ions is autoprotolysis of the solvent. Effects of trace water and other impurities will be commented on separately. Account will not be taken of either solution resistance or back diffusion between the closely spaced electrodes which occurs during extended periods of electrolysis. Despite these restrictions, the development does identify critical solvent properties, and correlates solvent properties with the magnitude of the current response. GCS theory is useful in discriminating between heterogeneous electron transfer phenomena and simple capacitive effects as the source of the current response.

According to GCS theory, when an electrode of potential ϕ_0 is placed in a solution of potential ϕ_S, ions and dipoles near the electrode surface redistribute to form a double layer and establish the potential profile in the solution near the electrode interface. The double layer is composed of two parts: the compact layer of thickness x_2, and the diffuse layer of thickness κ^{-1}

κ^{-1} is the Debye length. In pure solvents of moderate to low dielectric constants, a substantial concentration of ions with charges greater than one seems unlikely. So, the expression for a 1:1 electrolyte is appropriate.

$$\kappa = \left[\frac{2N_A c^* z^2 e^2}{1000\varepsilon\varepsilon_o kT}\right]^{1/2} \qquad [16]$$

where N_A - Avogadro's number, z - the charge (1), e - electronic charge (esu), k - Boltzmann's constant, T - temperature in degrees Kelvin, ε_o - permittivity of free space, taken here as $(4\pi)^{-1}$. c^* is the molar concentration of either the cations or anions in the bulk, and ε is the dielectric constant. The thickness of the diffuse layer is set by c^* and ε. In a pure redox solvent, where ions are only generated by autoprotolysis, the Debye length is set by $c^*/\varepsilon = K_{auto}^{1/2}/\varepsilon$, a fundamental property of the solvent. Values of κ^{-1}, c^*, ε and c^*/ε are cited in Table 8. In water with 0.1 M electrolyte, the Debye length is roughly 1 nm. κ^{-1} is substantially larger in pure solvents where the double layer is established and the potential is maintained only by dipoles and ions generated in the system by autoprotolysis. When the Debye length and the distance of separation between electrodes become comparable, a large fraction of the ions present in the solution are needed to maintain the interfacial potential.

Molecules at x_2 from the electrode surface experience a potential ϕ_2 with respect to ϕ_s. ϕ_2 is critical to determining the nature of the voltammetric response and the magnitude of the current. ϕ_2 has two major effects on the behavior of electrochemical systems; it influences the concentration of charged species near the electrode surface and it affects measured heterogeneous electron transfer rates. In high electrolyte solutions, ϕ_2 approaches zero. In pure solvents, the scarcity of ions is reflected in a non-zero value of ϕ_2. That is, the potential profile at the electrode surface falls off less rapidly because there are fewer ions available to balance the charge on the electrode. Based on GCS theory, ϕ_2 is related to

Table 8: Parameters of Importance in GCS Theory

	Solvent			
	H_2O	EtOH	ACN	DMSO
$c^* = K_{auto}^{1/2}$ (M)	1.0×10^{-7}	2.8×10^{-10}	5.6×10^{-15}	2.2×10^{-17}
ε	78.5	24.3	36.0	46.7
c^*/ε	1.3×10^{-9}	1.2×10^{-11}	1.6×10^{-16}	4.7×10^{-19}
κ^{-1} (cm)	9.6×10^{-5}	1.0×10^{-3}	0.28	5.0
ϕ_2[a] (V)	0.538	0.645	0.879	0.965

a) ϕ_2 calculated for $\phi_o = 1$ V and $x_2 = 0.5$ nm.

ϕ_o as:

$$\phi_o = \phi_2 + \frac{x_2\kappa}{a} \sinh [a\phi_2] \qquad [17]$$

where a = ze/2kT = z 19.42 V^{-1} at room temperature. In a pure solvent, it is clear that ϕ_2 is set by three factors: z, x_2, and c^*/ε. z is taken as 1. x_2 is difficult to estimate, but it is taken as 0.5 nm. Values of ϕ_2 are cited in Table 8 for ϕ_2 = 1 V and x_2= 0.5 nm. However, if x_2 is taken as 0.3 or 1.0 nm, ϕ_2 changes by less than 5 % for the four pure solvents considered here. Again, the critical properties of the solvent, pK_{auto} and ε, are central to describing the behavior of the system.

Correlation of Experimental Results with K_{auto} and ε: The influence of pK_{auto} and ε on the current response is illustrated with the stable, cyclic voltammetric responses of aniline (Figure 1-9a) and ethanol (Figure 1-9b). In both cases, the vapor was saturated. The potential was swept between -9.0 and +9.0 V. The insulator was teflon, although similar results were observed with other insulators. At each scan rate, the current response for ethanol is roughly fifty-fold higher than the signal for aniline. Ethanol is able to generate ions by autoprotolysis; pK_{auto}= 19.1. Although aniline is able to generate ions by base disassociation in water ($pK_{b,H2O}$= 9.4), it generates few ions as a pure liquid because it does not undergo significant autoprotolysis. Ion generation is required both to maintain the electrode potential and to compensate charges generated during electrolysis. A necessary, but less effective mechanism for charge compensation, is solvent polarization, as characterized by the dielectric constant. The current response is also correlated with the dielectric constants of ethanol (24.3) and aniline (6.9). Because of the limited supply of ions, aniline has a larger resistive drop and higher value of ϕ_2 than ethanol. This is reflected in the cyclic voltammetric response by lower currents and larger shifts in peak potentials with scan rate. Similar analyzes were performed for several solv-

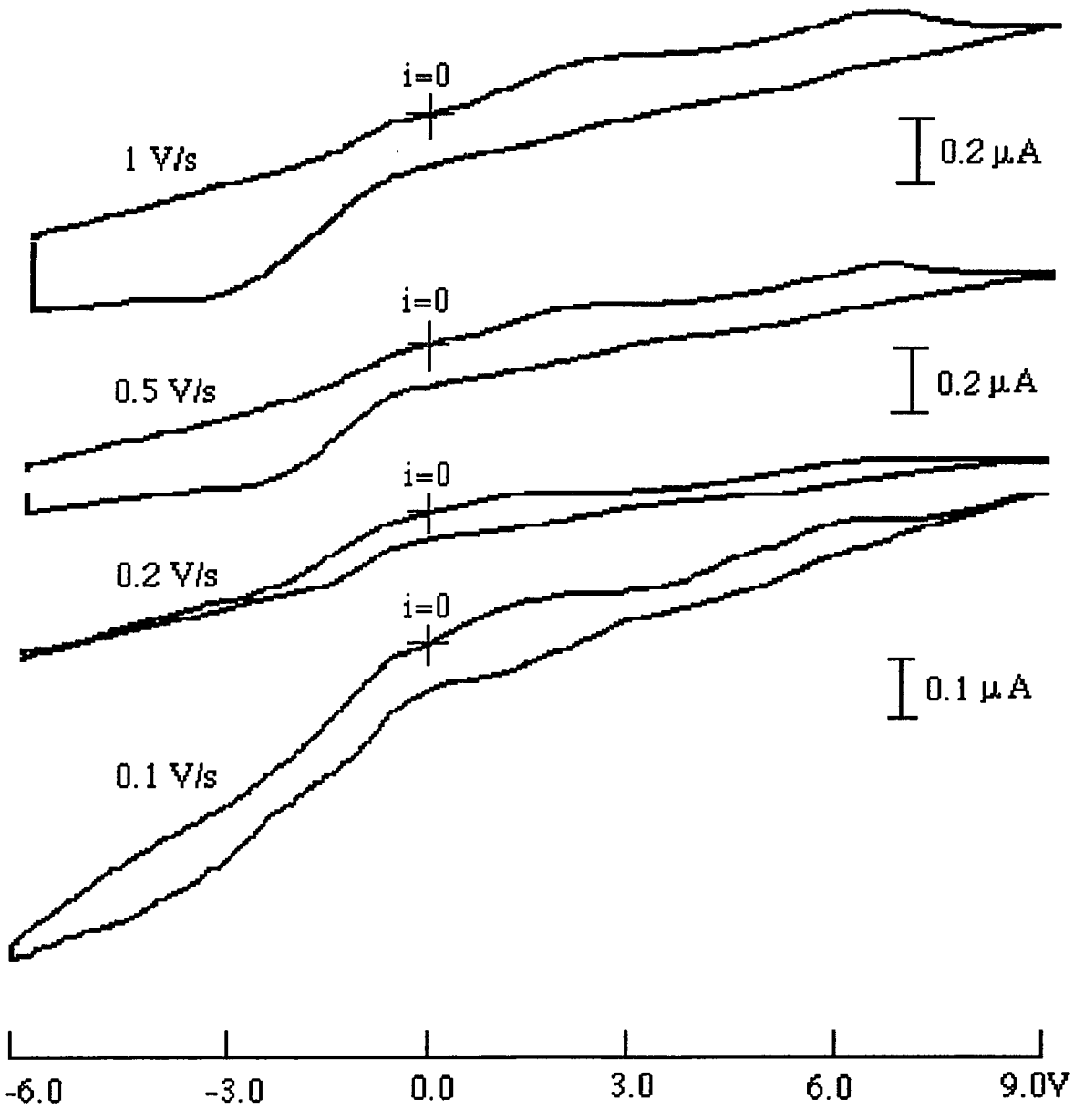

Figure 1-9a

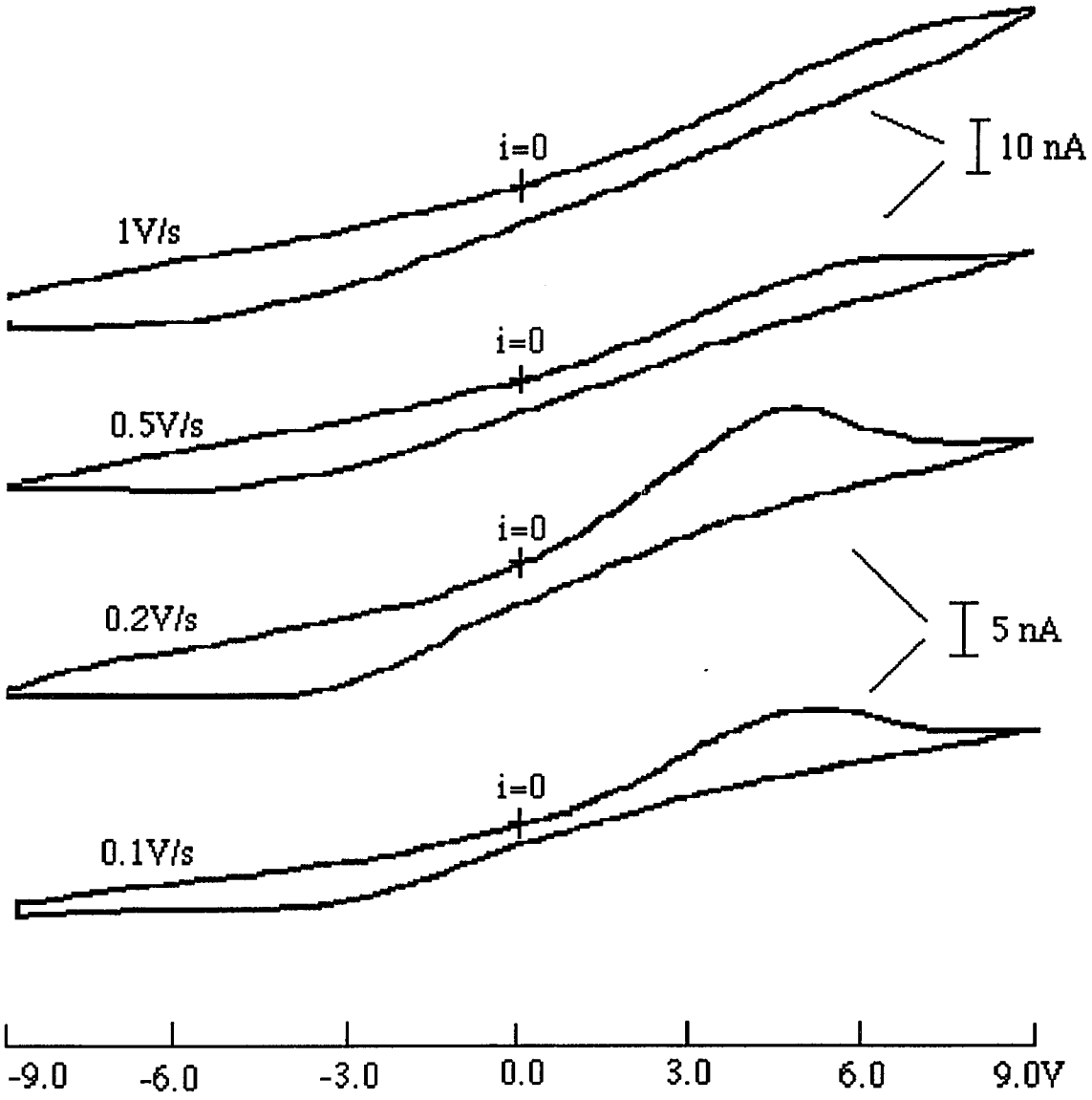

Figure 1-9b

Figure 1-9: Voltammetric Responses as a Function of Scan Rate for Ethanol (Figure 1-9a) and Aniline (Figure 1-9b).

Voltammograms were recorded in a one liter flask with a teflon sandwich electrode over a range of +9.0 to -9.0 V. In both cases, the vapor was saturated with solvent: 300 µl of ethanol; 100 µl of aniline. The ethanol response is better resolved because of the higher concentration of ions and stronger solvent polarity, as reflected in pK_{auto} and ε.

ents. Results for the autoprotolytic solvents, water and ACN, are shown in Figure 1-10. The inert solvent, hexane, is shown in Figure 1-11. The maximum currents observed for each at a scan rate of 1V/s, and three insulators are shown in Table 9. Note, the insulators vary in thickness by about 10%. (See Table 1.) There is clear correlation between the autoprotolysis constant and the maximum current response, as shown in Figure 1-12a. Hexane, which is unable to undergo either autoprotolysis or acid-base reactions, exhibits currents of only a few picoamperes. This current is of the order of the background current measured in vacuum. Hexane cannot generate ions to supply ionic conduction between the two electrodes or compensate ions generated by electrolysis. Data for the dielectric constant are also presented in Table 4 and Figure 1-12b. Species with dielectric constants greater than 5 to 10 are sufficiently polar to contribute to charge dissipation. The lower polarizability of aniline and hexane, are reflected in their lower current responses. Similar correlations between solvent ionization and polarizability are apparent in the gas chromatographic results of Pons and coworkers [1-3].

Acid-Base Reactions as a Source of Ions: As discussed above, the presence of trace water will not significantly enhance the conductivity of autoprotolytic solvents. For a species such as aniline, which is not autoprotolytic but can function as a weak base, the conductivity, and thus the current response, can be substantially enhanced by trace water. For a non-disassociating species like hexane, studied in the presence of only trace water, there are not enough ions to support electrolysis. However, under conditions where there is sufficient water present that the water can act as the solvent and the organic partitions into this electrolyte, electrolysis of the organic may be possible. High concentrations of water may have contributed to the signals observed by Pons and coworkers [1-3] for numerous inert species, where the ions are provided by the autoprotolysis of water.

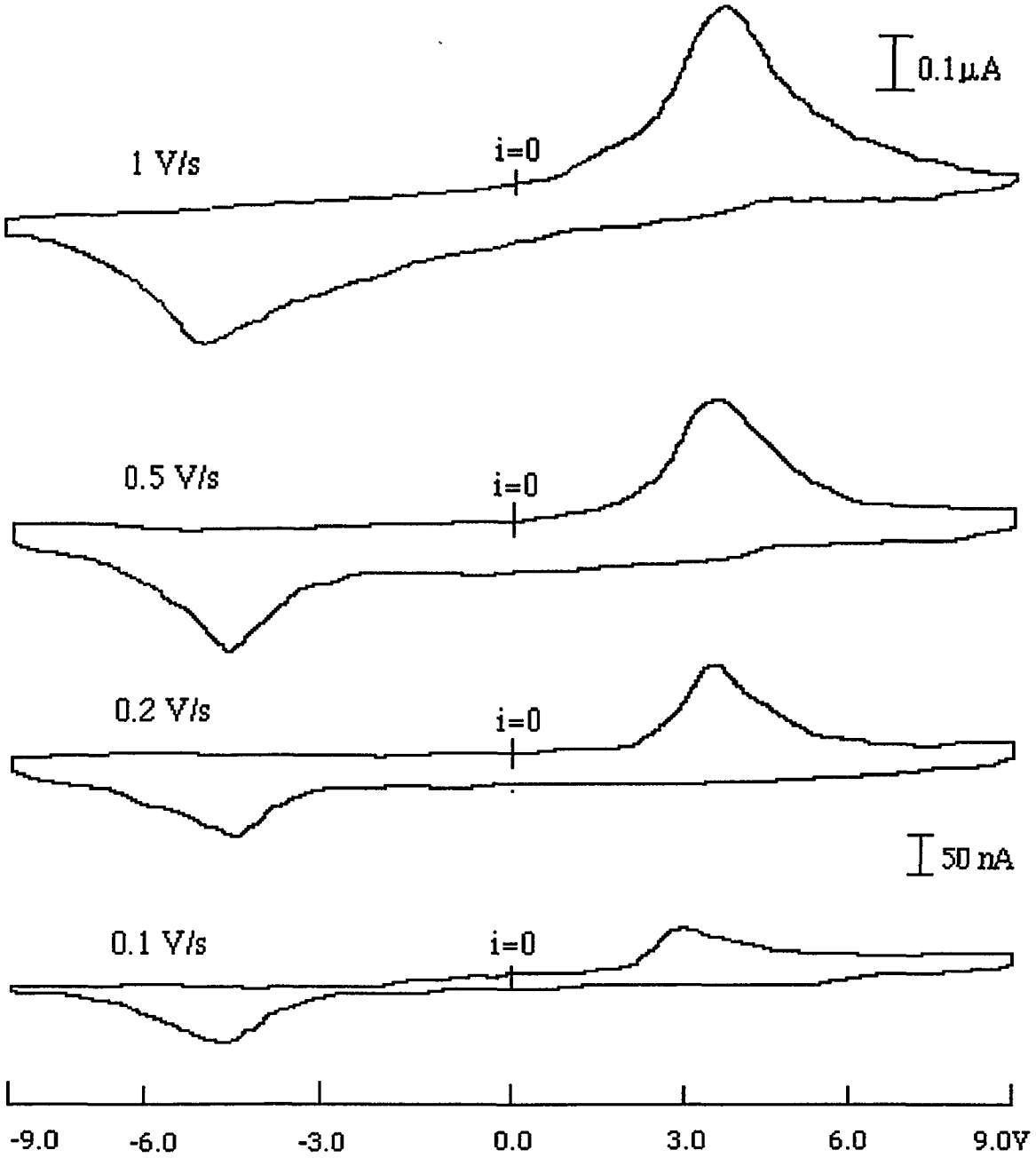

Figure 1-10a

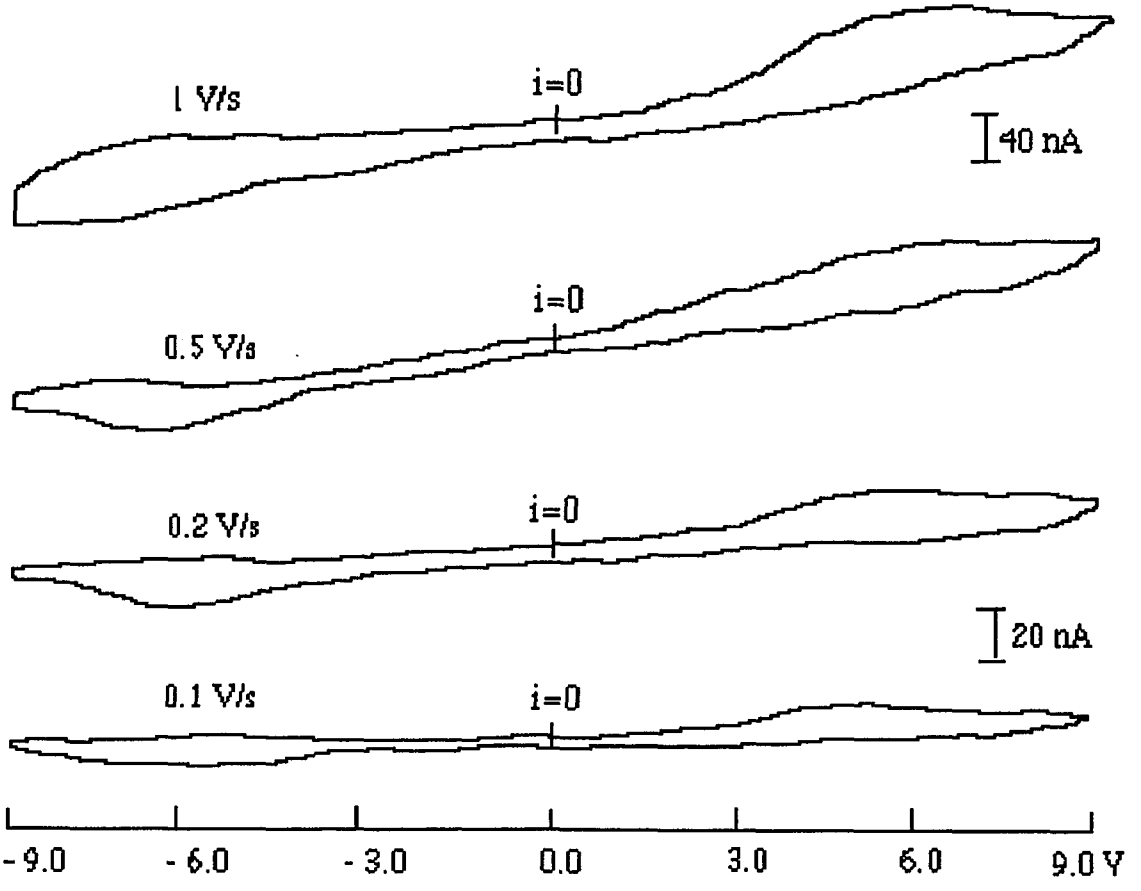

Figure 1-10b

Figure 1-10: Voltammetric Responses as a Function of Scan Rate for Water (Figure 1-10a) and ACN (Figure 1-10b).

Voltammograms were recorded in a one liter flask with a teflon sandwich electrode over a range of +9.0 to -9.0 V. In each case, the vapor was saturated with solvent: 150 µl of water; 250 µl of ACN.

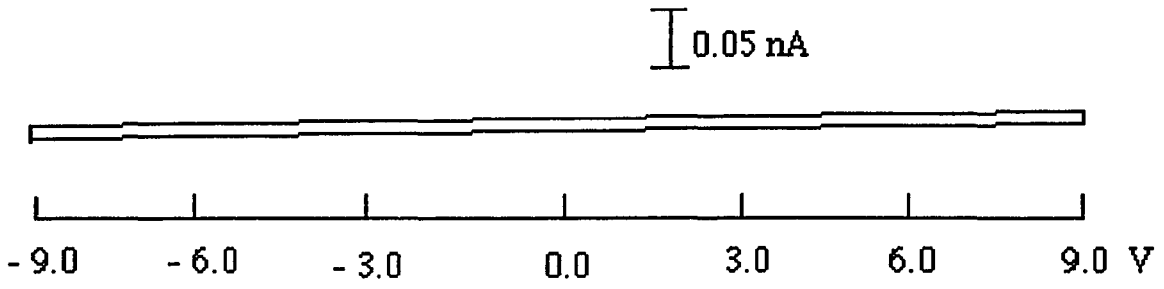

Figure 1-11: The Cyclic Voltammetric Response of Hexane.
The voltammogram was recorded at a teflon sandwich electrode after injecting 200 µl hexane into 1 liter flask scanning from -9.0 to +9.0 V at the scan rate 1.0 V/s. The voltammetric response is strictly capacitive because hexane cannot generate sufficient ions either by autoprotolysis or acid-base reactions to support electrolytic processes.

Table 9: Maximum Current (nA) Found for Various Solvents and Insulators at a Scan Rate of 1 V/s and a Potential of Approximately 7.0 V; Scan range +9.0 to -9.0 V.

	Maximum Current (nA)		
Solvent	Teflon	Polyethylene	Parafilm
H_2O	230	240	240
EtOH	100	105	95
ACN	33	22	24
DMSO	190*	15	16
ø-NH_2	8	9	7
C_6H_{14}	0	0	0

* DMSO was absorbed into the teflon

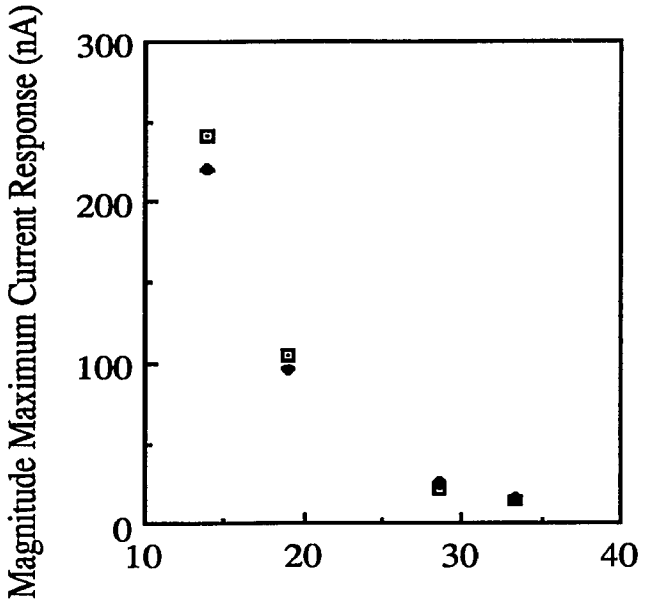

Figure 1-12a

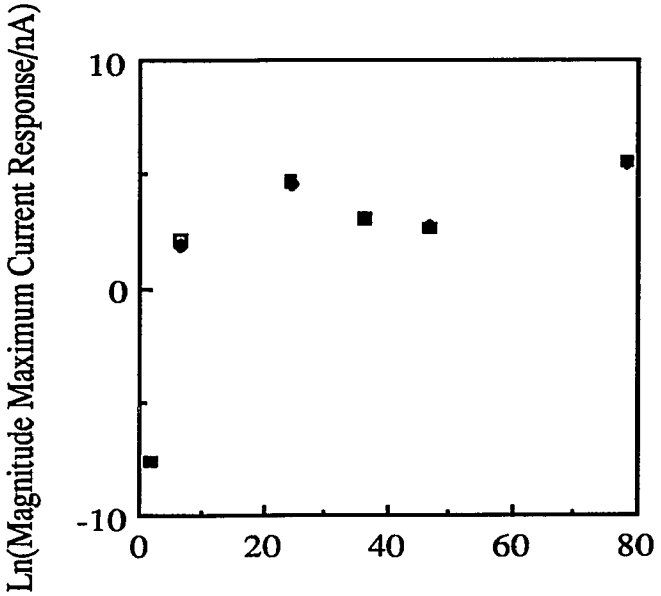

Figure 1-12b

Figure 1-12: Maximum Current Responses as a Function of Autoprotolysis (Figure 1-12a) and Dielectric Constants (Figure 1-12b).
Maximum currents recorded at 1 V/s over a range of +9.0 to -9.0 V for sandwich assemblies insulated with polyethylene (□) and parafilm (◆).
12a: The current magnitude as a function of the autoprotolysis constant for, sequentially, H_2O, EtOH, ACN and DMSO. The current decreases as the ion concentration falls with the autoprotolysis constant.
12b: Log of the maximum current as a function of dielectric constant for, sequentially C_6H_{14}, ø-NH_2, DMSO, ACN, EtOH and H_2O. Species with dielectric constants larger than 5 are sufficiently polar to support a current.

To investigate the effect of acid-base reactions between coadsorbed species, cyclic voltammetric studies were performed on a mixture of aniline and ethanol. The responses of each component alone are shown in Figure 1-9, where aniline exhibits lower current and higher resistance than ethanol because the concentration of ions is lower. Aniline undergoes no significant autoprotolysis. The stable cyclic voltammetric responses for a mixture of aniline and ethanol are shown in Figure 1-13. Note, the voltammograms of the mixture are better resolved than the voltammograms of either species alone.

Because of the autoprotolysis of ethanol, the conductivity of the mixture is greater than the conductivity of aniline. The ions generated by the ethanol also compensate the charge generated during aniline electrolysis. In addition, aniline contributes to the supply of ions by a base disassociation reaction with the ethanol.

$$C_6H_5NH_2 + CH_3CH_2OH \rightleftharpoons C_6H_5NH_3^+ + CH_3CH_2O^- \qquad [18]$$

The $pK_{b,EtOH}$ has been reported as 13.44 [26].

$$K_{b,EtOH} = \frac{[\text{ø-}NH_3^+]\,[EtO^-]}{[\text{ø-}NH_2]} = \frac{w^2}{c_{\text{ø-}NH_2} - w} \qquad [19]$$

By approximating the electrode surface to be covered with equal parts aniline and ethanol, and noting pure aniline is 10.97 M, the concentration of free ions, w, for a mixture of ethanol and aniline can be approximated. $w << c_{\text{ø-}NH_2} \approx 10.97/2$. $w \approx 5 \times 10^{-7}$ M. c^* for pure ethanol is 3×10^{-10} M. The ion concentration in the mixture of aniline and ethanol is roughly a thousand-fold higher than that in pure ethanol. The higher concentration of ionic species produces higher conduction, increased currents, better resolved peaks and smaller peak potential shifts associated with resistive drop. These effects are apparent when Figures 1-9 and 1-13 are compared.

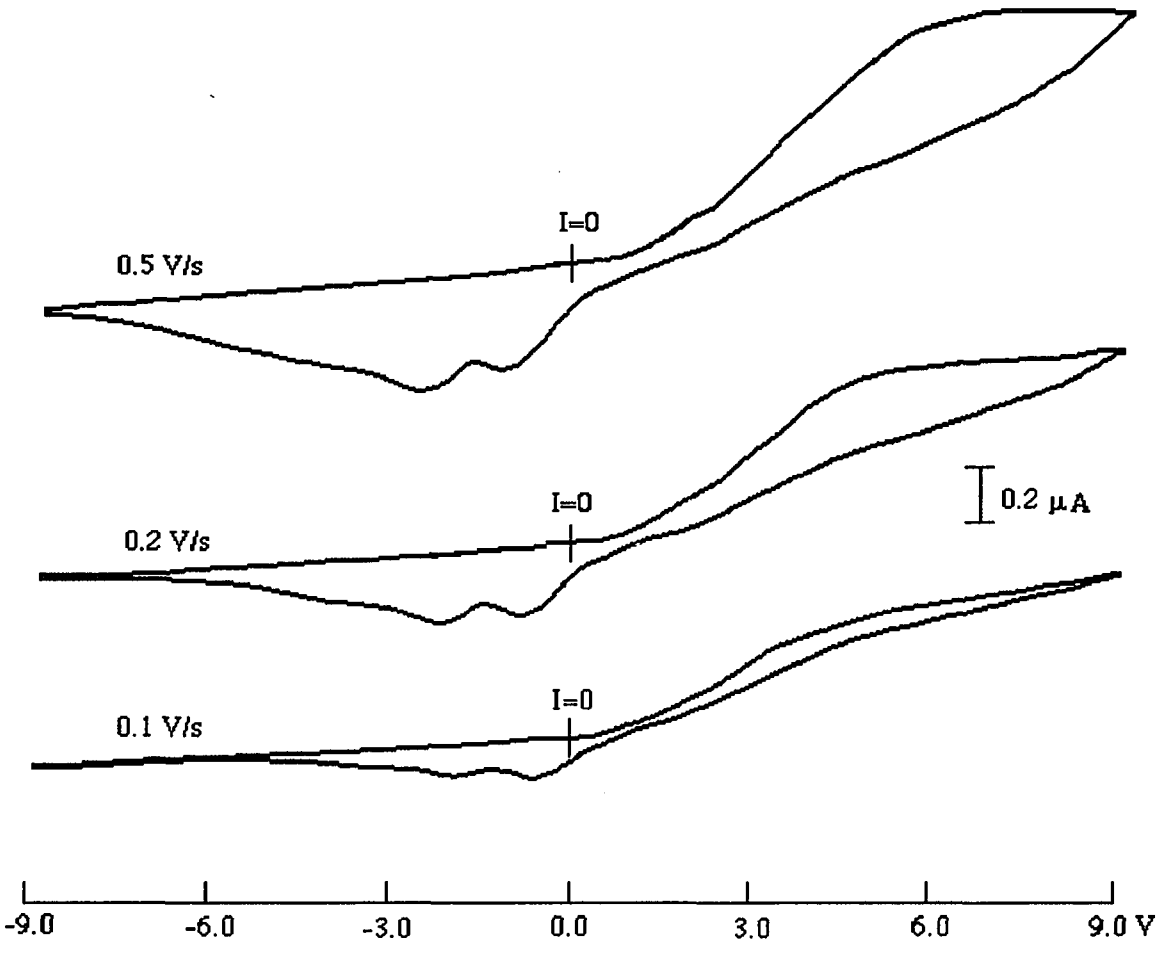

Figure 1-13: Cyclic Voltammograms for a Saturated Mixture of Ethanol and Aniline.

Voltammograms were recorded under the same experimental conditions as those in Figure 1-9. The vapor was saturated with aniline and ethanol by adding 100 and 200 µl, respectively. The voltammograms are better resolved than those of Figure 1-9 because of the increased conductivity associated with the ions generated by the acid-base reaction between ethanol and aniline.

1.3-3 The Nature of the Electrochemical Signal

In a gas phase environment, the electrochemical signal arises from either an electron transfer process or from a simple change in capacitance as molecules adsorb on the electrode surface. As discussed above, the ionizing capacity of the solvent will play a major part in determining whether a species undergoes electrolysis. For an electron transfer to occur, sufficient ions must be present to, first, establish and maintain the potential at the electrode surface, and, second, compensate any charges generated during the electrolysis. Electrolysis is most likely with species able to generate ions. The voltammetric response of a poorly ionizing species may be purely capacitive.

Experimental Evidence for Electrolysis Contributing to the Current Response: All of the species examined here, with the exception of hexane, are able to undergo ionization and electrolysis to some degree. For these species, several pieces of evidence point to an electron transfer as a major component of the current response. First, all species, except hexane, exhibit much higher currents than background. Second, the asymmetric shapes of the cyclic voltammograms also suggest electron transfer processes. This is particularly apparent in Figures 1-9b and 1-13 for ethanol and the ethanol/aniline mixture, as well as the water and ACN data in Figure 1-10. Third, preconcentration experiments were performed. The electrode was held at an extreme potential to electrolyze solvent and generate ions. Upon sweeping back to reverse the electrolysis reaction, large currents were found. The currents increased with the length of the preconcentration experiment. Such behavior is indicative of electrolyzing solvent to generate ions and then reversing the reaction on the reverse sweep. If the response were purely capacitive, the magnitude of the current response would have been independent of the length of electrolysis. Fourth, in Figure 1-9, the

cyclic voltammograms are better resolved at lower scan rates. This is consistent with the ions having time to respond to the change in electrode potential and to move to compensate the charge generated during electrolysis. Fifth, it is difficult to predict how peak currents associated with electrolysis should scale with scan rate in this electrode configuration. There are contributions from both radial and linear diffusion associated with the 8 μm disk. The solvent layer is roughly a hundred monolayers thick, so semi-infinite diffusion is not appropriate in the coordinate normal to the electrode. There is also the problem of feedback associated with the electrolysis products generated at the counter electrode in these systems. The transport processes include both diffusion and migration. However, it is not likely that the current should scale linearly with the scan rate. In the simplest models, capacitive currents have first order dependence on the scan rate. While it is difficult to determine precisely the dependence of the peak current for these systems on scan rate, it is not linear. This argues against a strictly capacitive response for these species.

Hexane is not able to ionize, either by autoprotolysis or protonation reactions with adsorbed water. Its voltammetric response is purely capacitive. See Figure 1-11. No peaks, indicative of electrolysis, are observed. In the gas chromatographic data of Pons and coworkers [1-3], the smallest responses were observed for species, which, like hexane, have no mechanism for generating ions. The small voltammetric responses in the gas chromatographic experiments, generated at a constant applied potential, were probably associated with capacitive responses.

Correlation of the Magnitude of the Electrolysis Current and the Solvent Properties: Consider the electrolysis of a neutral molecule. From GCS theory, the electrolysis is driven by $\phi_o - \phi_s - \phi_2$. As the concentration of ions decreases, ϕ_2 increases and the driving force for the reaction decreases. Thus, the magnitude of the current response is expected to decrease as ϕ_2 increases. Values of ϕ_2 calculated for ϕ_o= 1 V are listed in

Table 8 for several of the solvents considered here. Autoprotolysis is taken as the only source of ions. A comparison of ϕ_2 values with the current magnitudes in Table 9 shows the reduced driving force associated with higher ϕ_2 is manifested as lower current responses. ϕ_2 decrease and current increases with K_{auto} and ε.

The Electrolyzed Species: As stated previously, ϕ_2 has a major effect on the voltammetric response by affecting the concentration of ions near the electrode surface and by modifying the measured heterogeneous electron transfer rate. These effects are given mathematical expression in the Frumkin correction [27]. The correction can be expressed in two equations. The first equation quantifies the concentration of either the anions or the cations at x_2, $c_{\pm}(x)$, as

$$c_{\pm}(x_2) = c^* \exp[-zF\phi_2/RT] \qquad [20]$$

When the electrode potential is positive, ($\phi_2 > 0$), the concentration of anions will increase near the electrode surface, while the concentration of cations will decrease. For the pure solvents considered here, the description must remain qualitative because in GCS theory the volume of ions in the diffuse layer is not taken into account, and the concentration of ions at x_2 can grow without bounds. However, Equation 21 does indicate the concentration of anions around the anode is high, probably approaching a few percent of c_b, the concentration of the neutral solvent molecules. The second equation of the Frumkin correction relates the measured heterogeneous electron transfer rate, k_m^o, for some nonzero value of ϕ_2 to the standard heterogeneous rate, k^o, measured when ϕ_2 is zero. For α the transfer coefficient, n the number of electrons transferred, z the charge on the reactant,

$$k_m^o = k^o \exp[(\alpha n - z)F\phi_2/RT] \qquad [21]$$

Consider a situation where ϕ_o = 1 V, $\phi_2 > 0$, and a species can be

oxidized in a single electron transfer step. Let $\alpha = 0.5$. If the oxidized species is the neutral solvent molecule, k_m^o will be reduced compared to k^o. For $\phi_2 = 0.5$, $n = -1$, $k_m^o \approx 6x10^{-5}\ k^o$. Alternatively, if the anions clustered at x_2 are oxidized, $z = -1$, and $k_m^o \approx 1.6x10^4\ k^o$.

If the standard heterogeneous rate is similar for the neutral and monovalent anion of the solvent, the question arises as to what is actually oxidized. The concentration of anions at x_2 is less than that of the neutral solvent molecules, but it is not four orders of magnitude smaller. On the other hand, it is not clear that the system can maintain sufficient flux or generation of anions at x_2 to support the oxidation current solely by the electrolysis of anions. Alternatively, if the neutral solvent is electrolyzed, a positive ion is generated. An anion has to be present to compensate this charge. Where does the anion come from? Does it diffuse from the bulk solvent, or does a solvent molecule autoprotolyze with the anion compensating the charge generated by the electrolysis and the cation migrating into the bulk? Both processes are of equal energetic cost. Finally, if the anions at x_2 are involved in either the electrolysis or charge compensation process, what ions are maintaining the potential at the electrode interface? It quickly becomes clear that the ions involved in the electrolysis are the same ions involved in maintaining interfacial potential. The ion concentration and potential profiles are coupled in a highly convoluted manner. It is not possible to separate these effects in any simple way. Similar questions have been noted by Malmsten, et al., [28] for the electrolysis of pure, bulk solvents, such as nitrobenzene. The difficulty, as noted by Oldham [29], is that the diffuse layer (κ^{-1}) and the mass transport layer are of comparable thickness. It is not clear whether the current reflects the electrolysis of ions, neutral species or a combination of both.

1.4 SUMMARY

The results of these studies on voltammetric responses in a gas phase environment are summarized as follows.

(1) In a gas phase environment, the electrolysis of solvent molecules is carried out within a few layers of solvent adsorbed on the surface of the electrode assembly.

(2) Ionic contact is maintained between the two electrodes by autoprotolysis of the adsorbed solvent and acid-base disassociation reactions between the adsorbed solvent and sorbed protic species, such as water.

(3) The current response of species able to generate ions via disassociation reactions is correlated with the autoprotolysis and dielectric constants of the solvent. The current is due to an heterogeneous electron transfer process.

(4) The current response of species which cannot generate ions, such as hexane, is a strictly capacitive response.

(5) Trace water will not have a dramatic effect on the conductivity and current response of autoprotolytic species. The response of weak bases which cannot undergo autoprotolysis, can be enhanced by disassociation reactions with protic impurities.

(6) A description of electrolysis processes in the absence of added electrolyte are complex because the ions which establish and maintain the double layer and interfacial potential are also involved in the electrolysis process as either the redox species itself or the ions which compensate charge generated during the electrolysis.

(7) In the absence of added electrolyte, Gouy Chapman Stern models and the Frumkin correction support a qualitative description of the double layer and electron transfer processes, but they fail to describe the system quantitatively because the models do not account for the volume of ions in the diffuse layer. The calculated ion concentration at x_2 is unbounded and exceeds reasonable values in the absence of added electrolyte.

Chapter II

Cyclic Voltammetric Responses for Inlaid Microdisks with Shields of Thickness Comparable to the Electrode Radius: Experiments and Simulation

2.1 INTRODUCTION

Microelectrodes have become a major tool for studying nonstandard electrochemical systems. Solutions without added electrolyte [1-5], frozen solutions [6], and gas phase environments [7-12] are examples of matrices which the use of microelectrodes has opened to inspection by electrochemical methods. Drawing on knowledge of polarographic responses, electrochemists often interpret the voltammetric responses of microelectrodes using the current response expected for spherical and hemispherical electrodes. This approximation is appropriate for spherical microelectrodes. Oldham and Zoski [13] have shown the hemispherical current and the steady state current at a disk inlaid in a semi-infinite insulator are the same with in a multiplicative constant ($4/\pi$) when the radius of the sphere and disk are equal. For larger inlaid disks and disks where the insulating shield is not large compared to either the electrode radius or the diffusion length generated during the course of the sweep, this approximation has limitations.

Voltammetric responses for large, traditional electrodes are well characterized for a variety of electrode geometries, common voltammetric perturbations, and assorted conditions of chemical and electrode kinetics [14]. For large inlaid disk electrodes, radial diffusion is not a concern on the time scale of most transient measurements because the vast majority of the flux which contributes to the current occurs normal to the electrode surface. In modeling these systems, the insulating shield around the disk is assumed to

be large compared to the thickness of the diffusion layer. This precludes the diffusion field from being established from behind the plane of the electrode. In experimental systems, if this condition is not satisfied, the effect is not usually substantial because radial diffusion contributes so little to the total current at a large inlaid disk. For macroscopic, spherical electrodes, radial diffusion is the only mode of mass transport. Questions about how the flux to a mercury electrode, and thus the current, are disrupted by the capillary which supports the electrode have long been considered in modeling spherical electrodes [15].

Microelectrodes have been constructed as inlaid disks with a wide range of diameters. Electrode radii small as 10Å have been made [16], but standard diameters are typically 100 nm to 100 microns. Two common methods of electrode construction are either to draw down a capillary around a wire [1] or to dip coat an insulating polymer on the outer surface of a cylindrical conductor such as a carbon fiber [17]. With these methods of construction, the thickness of the insulating shield and the radius of the disk are comparable. On the time scale of standard voltammetric perturbations, the diffusion field at these electrodes undergoes a transition from linear to radial symmetry and the diffusion field is established radially behind the plane of the electrode and shield. How much the flux from behind the plane of the electrode enhances the current will depend on the size of the electrode and the shield. Thus, both the thickness of the insulating shield and the radius of the inlaid disk are important in evaluating voltammetric responses.

Consider a typical carbon fiber microelectrode constructed by drawing down a glass capillary around the conducting fiber. The radius of the fiber is about 3 μm, and the thickness of the concentric shield might be about 7 μm. The diameter of the entire microdisk assembly is then 20 μm. For a voltammetric sweep at 0.1 V/s over 1 V, the diffusion length will be established for roughly 10 s. If the voltammetric response is to be interpreted using the steady state response for a hemispherical electrode, two

conditions must be met. First, the system must be at steady state. Steady state is established when the diffusion length, $\delta = (2Dt)^{1/2}$, is large compared to the disk radius, r_o. For, t = 10 s, and D = $5x10^{-6}$ cm^2/s, δ = 100 μm. Then, δ/r_o= 33; the system is at steady state. Second, diffusion from around the edges of the insulating shield from behind the plane of the electrode must be avoided. Given, δ =100 μm and a shield thickness of 7 μm, diffusion around the edges will definitely occur. If the scan rate is increased so diffusion from behind the plane of the shield is prevented, then δ will be reduced to about 7 μm and the system will no longer be at steady state because δ/r_o= 2.3. From this system, it is apparent that longer times are needed to establish steady state, but the increased times lead to a second transport regime where current enhancements associated with flux from behind the plane of the electrode occur. Thus, the interpretation of voltammetric responses at inlaid disks constructed with shields which are not effectively semi-infinite in thickness will not be well represented by the spherical or hemispherical approximations.

Here, we present a computer simulation for the effect of shield thickness on the cyclic voltammetric response of an inlaid microdisk. The simulation is restricted to Nernstian kinetics. The simulation is a two dimensional, finite difference simulation in cylindrical coordinates; there is no angular dependence. Expanding spatial grids are employed in both the axial and radial coordinates. The axial coordinate is expanded with a uniform, exponential grid. The radial grid is not uniform. Because there are two pivotal interfaces in the simulation, the electrode/insulator and insulator/solution interfaces, more refined grids are needed at two places across the plane of the electrode. This is accomplished by creating a radial grid which expands from the edge of the electrode/insulator interface to the midpoint of the insulator where it begins to contract again as the insulator/solution interface is approached. The radial grid then expands again as distance from the insulator edge is increased. The method for

defining this non-uniform grid is presented.

The results of the simulation address several questions:

(1) How does the thickness of the insulating shield influence the voltammetric response ?

(2) How is steady state recognized at an inlaid disk ?

(3) How can the disk radius and the shield thickness be estimated from the voltammetric response ?

(4) What are the limitations of using the spherical approximation to interpret the voltammetric response of inlaid disk electrodes ?

2.2 EXPERIMENTAL

2.2-1 Electroactive Species and Solvents

Potassium ferricyanide (Baker Co.) and dopamine (Aldrich Chemicals) were used as redox couples in the experimental measurements. Sodium sulfate (anhydrous, reagent: A.C.S., MCB Manufacturing Chemicals, Inc.) and HCl were used as electrolytes for potassium ferricyanide and dopamine, respectively. Distilled water was purified through a Milli-Q, QM-140 (Millipore Corp.).

2.2-2 Electrodes

The working electrode made in the lab was a carbon fiber microdisk, which was shielded by the glass capillary. The radius of carbon fiber was determined by scanning electron microscopy (Hitachi S-570). The thickness of the glass insulator varies with different electrode and was measured by SEM. The process of making these electrode was described in Chapter I, and illustrated in Figure 1-1a. Ag wire was used as a quasi-reference electrode and a 4 cm^2 Pt screen was used as the counter electrode.

2.2-3 Instrument and Measurement

The electrochemical instruments were manufactured by Princeton Applied Research; they were a Model 173 potentiostat and Model 175 universal programmer. All cyclic voltammograms were recorded on a Norland 300 processing digital oscilloscope and an x-y recorder (Soltec.).

The technique employed was cyclic voltammetry. Resistance compensation was used for all measurements. All measurements were carried out at room temperature, and five minutes were allowed between measurements to ensure the system had reequilibrated.

2.3 THEORY

2.3-1 Electrochemical Reaction Model

The model is developed for a reversible heterogeneous electron transfer reaction:

$$A + ne \rightleftharpoons B^{ne-} \qquad [1]$$

The electrode is an inlaid microdisk. As shown in the cross section of Figure 2-1a, the disk, of radius, a, is encircled by an insulator. The surfaces of the disk and insulator are flush. The radius of the entire electrode assembly, including the thickness of the disk and insulator, is b.

The electrode is modeled by the transport equation expressed in cylindrical coordinates without the angular dependence.

$$\frac{\delta c(z,r,t)}{\delta t} = D\left[\frac{\delta^2 c(z,r,t)}{\delta r^2} + \frac{1}{r}\frac{\delta c(z,r,t)}{\delta r} + \frac{\delta^2 c(z,r,t)}{\delta z^2}\right] \qquad [2]$$

where r is defined as the radial coordinate, parallel to the plane of the electrode surface; z is the coordinate perpendicular to the electrode surface. r has a value of zero at the center of the disk. z is zero at the surface of the electrode, positive above and negative below the plane of the electrode, as shown in Figure 2-1b. t is time. c(z,r,t) is the space and time dependent concentration. D is the diffusion coefficient.

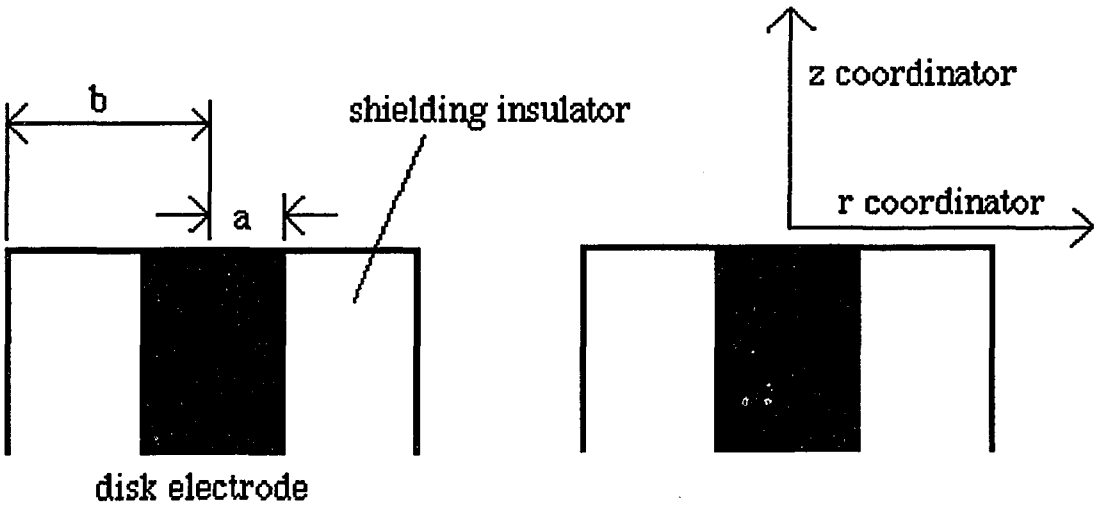

Figure 2-1a Figure 2-1b

Figure 2-1: Schematic Diagram of the Disk Electrode Geometry Used in the Simulation

Based on Faraday's equation, the time dependent current, i(t), is set by the total flux normal to the electrode surface at t,

$$\frac{i(t)}{nFA} = -2\pi D \int_0^a r \left[\frac{\partial c(z,r,t)}{\partial z}\right]_{z=0} dr \qquad [3]$$

where n, F, and A are the number of electron transferred, Faraday's constant, and the electrode area, respectively.

The diffusion coefficients of the oxidized and reduced species are taken as equal. This leads to the equation, $c_A(z,r,t) + c_B(z,r,t) = c^o_A$, which is appropriate in the absence of chemical reactions. c^o_A is the bulk and initial concentration. Given these constraints, the problem is completely specified by considering only the concentration of A. The Nernstian condition is then

specified as:

$$\exp[\frac{-nF(E-E^{o'})}{RT}] = \frac{c_B(0,r,t)}{c_A(0,r,t)} = \frac{c^o_A - c_A(0,r,t)}{c_A(0,r,t)} \qquad [4]$$

where $E^{o'}$ is the formal potential. F/RT is taken as 38.92 V^{-1}, the value appropriate for T = 298 K.

The modeled voltammetric process is linear sweep cyclic voltammetry. The initial potential for the sweep is E_o and the switching potential is E_f. All potentials are in units of volts. For a scan rate, v (V/s), the total time for the sweep is $T_t = 2\,[E_f - E_o\,]/v$. The potential, E(t), at any time during the sweep is then expressed as :

$$E(t) = \begin{cases} E_o + vt & 0 \le t < T_t/2 \\ E_o + v(T_t - t) & T_t/2 \le t \le T_t \end{cases} \qquad [5]$$

The boundary and initial conditions for Equation 2 are as follows:

$r \ge 0, z \ge 0, t = 0$:

$r > b, z < 0, t = 0$: $\quad c_A(z,r,t) = c^o_A \qquad [6]$

$0 \le r < a, z = 0, t > 0$:

$$Flux_A(r) = - D_A [\frac{\partial c_A(z,r,t)}{\partial z}]_{z=0} \qquad [7]$$

$$c_A(0,r,t) = \frac{c^o_A}{1 + \exp[\frac{nF(E^{o'} - E)}{RT}]} \qquad [8]$$

$b > r > a, z = 0, t > 0$:

$$D_A [\frac{\partial c_A(z,r,t)}{\partial z}]_{z=0} = 0 \qquad [9]$$

$r \to \infty, z \to \infty, t > 0$: $\quad c_A(z,r,t) = c^o_A \qquad [10]$

$r > b, \; z \to -\infty, t > 0$: $\quad c_A(z,r,t) = c^o_A \qquad [11]$

$z \geq 0, r = 0$:

$$D_A\left[\frac{\partial c_A(z,r,t)}{\partial r}\right]_{r=0} = 0 \qquad [12]$$

$z < 0, r = b$:

$$D_A\left[\frac{\partial c_A(z,r,t)}{\partial r}\right]_{r=b} = 0 \qquad [13]$$

where $Flux_A(r)$ is the flux of species A normal to the electrode surface at radial position r and z = 0, the surface of the electrode. Note, Equation 8 follows from Equation 4.

2.3-2 Simulation Model

The simulation is carried out by standard explicit finite difference methods. The time coordinate is expressed using an uniform grid, while the spatial coordinates are treated with an exponentially expanding spatial grid (EESG) [18-20]. EESG offers both significantly more rapid computations, and better resolution of concentration profiles at the edges of the micro-electrode. This resolution is important in modeling the transition from linear to radial diffusion observed at inlaid microdisks. Small grid elements are used at edges and near the electrode surface. The grid resolution becomes increasingly coarse as the distance from the electrode surface and edges increases. A schematic of the exponential expanding spatial grid distributed on the electrode surface is shown in the Figure 2-2. Note the high density of small grid elements across the face of the electrode, at the edges between the electrode and the insulator, and around the corner at the insulator/solution interface. We call this spatial grid an irregular EESG. The use of small elements in regions where the concentration gradients are steepest results in more accurate descriptions of the flux, and, thus, the current response. Because edge effects are more important for inlaid electrodes than spherical electrodes, the proper calculation of diffusion flux at the edge of inlaid disk is critical to the simulation. In this work, the flux at

the outer edge of the electrode is better resolved by using finer grids near r = a in the evaluation of Equation 3. At r = b, more elements are needed to model the influence of diffusion from behind the plane of the electrode.

An examination of Figure 2-2 shows the grid in the z coordinate is expanded uniformly about the plane of the electrode.

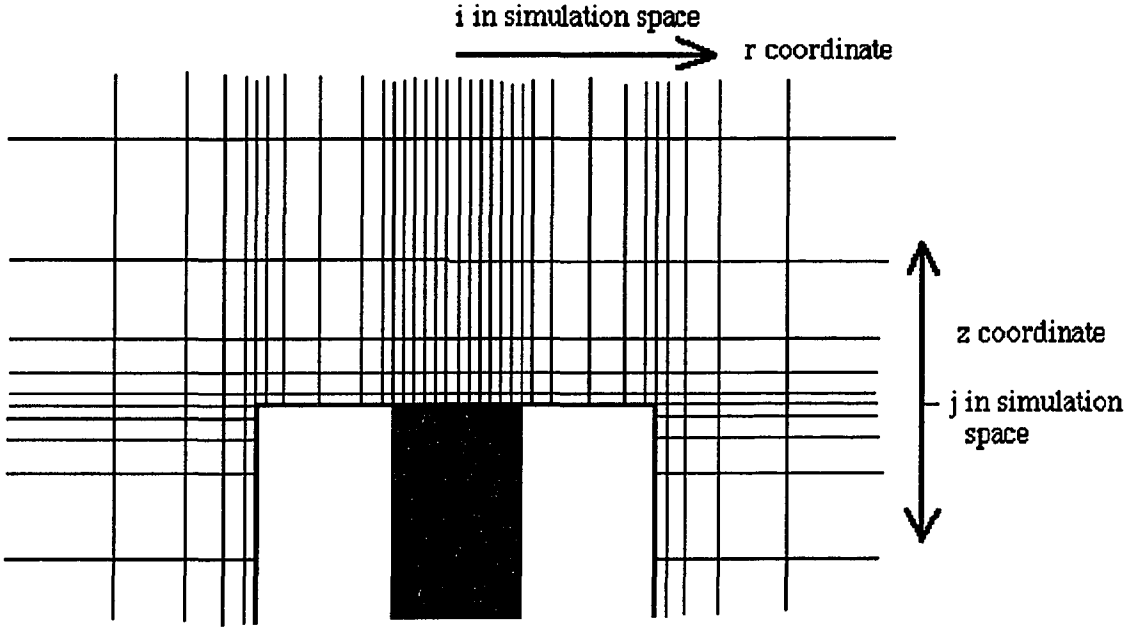

Figure 2-2: Schematic Diagram of the EESG Used in the Simulation

In EESG, a uniform expansion is modeled as: [18-20]

$$\Delta z_j = \Delta z \exp[\beta(|j| - 1)] \qquad [14]$$

where β is the exponential coefficient which sets the rate of spatial expansion. Δz is the size of the smallest grid element in the z coordinate, and j numbers the grid elements in the z coordinate. $j = 0$ in the plane of the electrode, $j < 0$ below the plane of the electrode and $j > 0$ above the plane of the electrode. Δz_j is the thickness of the j^{th} grid element. z_j is the distance from the plane of

the electrode surface to the point in the j^{th} element where the concentration is measured. z_j is calculated as following:

$$z_j = \frac{\exp[\beta|j| - 0.5] - 1}{\exp[\beta] - 1} \qquad [15]$$

As shown in Figure 2-2, the grid in the radial direction is dense across the electrode surface, begins to expand across the insulator and then contracts toward the edge of the shield. The radial grid then begins to expand again as the distance from the edge of the shield increases. This expansion is more complex than that described in the z coordinate. Here, Δr is the size of the smallest grid element in the radial direction, and $\Delta r = \Delta z$ is used through the simulation. i numbers the grid elements radially from the center of the electrode. By analogy to Δz_j and z_j, Δr_j is the thickness of the i^{th} radial element, and r_j is the distance radially from the center of the electrode to the point in the i^{th} element where the concentration is represented. Because the radial grid expands, contracts and expands, the calculation of Δr_j and r_j is more complex than the calculation of Δz_j and z_j. The calculations of these values are summarized in the Appendix A. The electrode lengths, a and b, are $a = N_{ra}\Delta r$ and

$$b = \sum_{i=1}^{N_{rb}} \Delta r_i.$$

N_{ra} and N_{rb} are the number of grid elements across the radius of the active electrode area and the total electrode radius, respectively.

2.3-3 Dimensionless Treatment

To make the simulation most general, the following dimensionless parameters are introduced. The simulation divides the total time, T_t, into k_{max} time steps, where each time step has a length Δt; $\Delta t = T_t/k_{max}$. k is the time counter, such that for any time, t, $t = k\,\Delta t$. Recall, i and j number the grid elements in the r and z coordinates. The dimensionless simulation

parameters are then:

Concentration:

$$AA(j,i,k) = \frac{c_A(z,r,t,)}{c_A^o} \qquad [16]$$

Time:

$$\tau(k) = \frac{t}{T_t} = \frac{k}{K_{max}} \qquad [17]$$

Potential:

$$V(k) = \frac{F}{RT}[E_o + 2(E_f - E^{o'})\frac{k}{k_{max}}]$$

$$0 \le k \le k_{max}/2$$

$$V(k) = \frac{F}{RT}[E_o + 2(E_f - E^{o'})(1 - \frac{k}{k_{max}})]$$

$$k_{max}/2 < k < k_{max} \qquad [18]$$

Diffusion Coefficient:

$$DM = D_A\frac{\Delta t}{\Delta r^2} = D_A\frac{\Delta t}{\Delta z^2} \qquad [19]$$

Current:

$$Z(k) = \frac{i(t)\ a\ \pi}{4nFADc_A^o} = \frac{i(t)}{4nFac_A^o} \qquad [20]$$

where $4nFaDc_A^o = I_{ss}$, the steady state current at a disk inlaid in a semi-infinite insulating plane.

The finite difference representation of Equation (2), based on a central difference in space and a forward difference in time is

$c_A(z_j, r_i, t + \Delta t) = c_A(z_j, r_i, t)$

$$+ D_A \frac{\Delta t}{\Delta z} \left[\frac{c_A(z_{j+1}, r_i, t) - c_A(z_j, r_i, t)}{z_{j+1} - z_j} \right.$$

$$\left. - \frac{c_A(z_j, r_i, t) - c_A(z_{j-1}, r_i, t)}{z_j - z_{j-1}} \right]$$

$$+ D_A \frac{\Delta t}{\Delta r} \left[\frac{c_A(z_j, r_{i+1}, t) - c_A(z_j, r_i, t)}{r_{i+1} - r_i} \right.$$

$$\left. - \frac{c_A(z_j, r_i, t) - c_A(z_j, r_{i-1}, t)}{r_i - r_{i-1}} \right]$$

$$+ 2D_A \frac{\Delta t}{r_i} \left[\frac{c_A(z_j, r_{i+1}, t) - c_A(z_j, r_{i-1}, t)}{r_{i+1} - r_{i-1}} \right] \qquad [21]$$

When the distance coordinates of r and z are converted to i and j, and time t is converted to k in simulation equation, the above equation can be simply written in dimensionless form as:

$$\begin{aligned} AA(j,i,k+1) = {} & AA(j,i,k)+DZ2(j)[AA(j+1,i,k)-AA(j,i,k)] \\ & DZ1(j)[AA(j,i,k)-AA(j-1,i,k)] \\ & DR2(i)[AA(j,i+1,k)-AA(j,i,k)] \\ & DR1(i)[AA(j,i,k)-AA(j,i-1,k)] \\ & DR3(i)[AA(j,i+1,k)-AA(j,i-1,k)] \end{aligned} \qquad [22]$$

where DZ2(j), DZ1(j), DR2(i), DR1(i) and DR3(i) are dimensionless parameters, which combine DM with either Δz_j and z_j or Δr_i and r_i. These EESG dimensionless diffusion coefficients are functions of distance, as indicated by j and i. DZ2(j), DZ1(j), DR2(i), DR1(i) and DR3(i) are evaluated and listed in Table 1. During each time step, Eqn. 22 is evaluated for all i and j, subject to the initial and boundary conditions of Eqns. 5 to 13.

The dimensionless current, Z(k), is then evaluated, as in Eqn. 3 and 20, for all fluxes normal to the electrode surface for $j = 0$ and $i \leq N_{ra}$.

All simulations were performed for $n = 1$, $T = 298$ K, $\beta = 0.3$ and $\alpha = 0.5$. These general parameters are listed in Table 2. The simulation was performed on a VAX-VMS 8600 cluster. The program was written in Fortran 77 language and is listed in Appendix B.

Table 1: Dimensionless Diffusion Coefficients Used in the Expanding Grid Simulations.

Dimensionless Diffusion Coefficient	Formula	Simulation Formula
DZ2(j)	$\frac{D\Delta t}{\Delta z_j}\frac{1}{(z_{j+1}-z_j)}$	$\frac{DM}{\text{Delt z(j)}^*}\frac{1}{[\text{Ave z(j+1)}^{**} - \text{Ave z(j)}]}$
DZ1(j)	$\frac{D\Delta t}{\Delta z_j}\frac{1}{(z_j-z_{j-1})}$	$\frac{DM}{\text{Delt z(j)}}\frac{1}{[\text{Ave z(j)} - \text{Ave z(j -1)}]}$
DR2(i)	$\frac{D\Delta t}{\Delta r_i}\frac{1}{(r_{i+1}-r_i)}$	$\frac{DM}{\text{Delt r(i)}}\frac{1}{[\text{Ave r(i+1)} - \text{Ave r(i)}]}$
DR1(i)	$\frac{D\Delta t}{\Delta r_i}\frac{1}{(r_i - r_{i-1})}$	$\frac{DM}{\text{Delt r(i)}}\frac{1}{[\text{Ave r(i)} - \text{Ave r(i-1)}]}$
DR3(i)	$\frac{D\Delta t}{r_i}\frac{1}{(r_{i+1}-R_{i-1})}$	$\frac{DM}{\text{Delt r(i)}}\frac{1}{[\text{Ave r(i+1)} - \text{Ave r(i-1)}]}$

* Delt z(j) = exp [β(j-1)].
** Ave z(j) = {exp[ß(j - 0.5)] -1.0}/[exp(ß) -1.0].

Table 2: Values of Some Constants Used in the Simulation Program

Constant	Value
Electron Transfer, n	1
Transfer Coefficient, α	0.5
Expanding Coefficient, β	0.3
Temperature, T (K)	298
Faraday Constant, F (F)	96496
Gas Constant, R (J mol^{-1} K^{-1})	8.314

2.4 RESULTS AND DISCUSSION

2.4-1 Evaluation of the Simulation

The validity of the simulation was tested in several ways. First, the program was run for the hemispherical and linear cases; the simulated results matched the known analytical solutions. The difference between the analytical and simulation results was within 0.05%.

Second, the irregular two dimension EESG had been tested in different ways. The difference between the uniform grid and the one dimensional regular EESG approaches zero as the number of time iterations becomes large enough [20-22]. We established our one dimensional uniform EESG yielded the same result as the one dimensional uniform grid for case of linear diffusion to a planar electrode. In a simulation, transport is restricted to linear diffusion by placing simulation elements directly over the electrode; no elements are placed over the insulator. Essentially, the simulation is for a disk in a hole. To ensure that two dimensional problems were well simulated by the program, we ran both the one dimensional uniform and the two dimensional uniform EESG methods for the disk in a hole. The results were

the same within the error of the simulation; this shows the two dimensional uniform EESG is an accurate representation of two dimensional diffusion. The two dimensional uniform EESG and the two dimensional irregular EESG were run for a disk with a semi-infinite shielded. In this case, the steady state current is characterized by the analytical equation, $I_{ss}=4nFDc_A^o$. The results are shown in Table 3. The results from the two different methods were the same within the error of simulation. This is expected for the case where there are no edge effects. In cases where the electrode is small enough for the edge effects to become significant, the irregular two dimensional EESG has better resolution than the regular two dimensional EESG because the irregular EESG places more grid elements near the edges of the insulator, allowing a better approximation of the concentration profiles at the insulator edges.

Table 3: Comparison of Dimensionless Peak Currents Calculated from the Regular EESG and Irregular EESG Methods for a Disk Electrode Embedded in a Semi-Infinite Insulating Shield

Number of Time Iteration (x 10^3)	Dimensionless Peak Current	
	Regular EESG	Irregular EESG
18	1.0564	1.0563
36	1.0333	1.0332
72	1.0181	1.0180
144	1.0078	1.0078
288	0.9998	0.9998

Third, improvement in the simulated results was achieved by increasing the number of elements across the electrode. The choice of grid resolution was found by increasing the number of grid elements until the simulated current did not change significantly upon further increases in the number of grid elements. In Table 4, the relationship between the calculated, dimensionless steady state current, Z_{ss}, and the number of grid elements across the active electrode area, N_{ra}, is shown. The expected dimensionless steady state current for an inlaid disk in a semi-infinite insulating plane is 1. It is obvious that the resolution improves as the number of grid elements increases. However, each time N_{ra} increases by one, the computation time increases approximately two orders of magnitude. In all of the following simulations, the number of grid elements used to represent the active electrode area (N_{ra}) was chosen as 6 because this number was sufficient to reduce the variation in the simulated response to below 0.1% despite further increases in N_{ra}. This choice also allowed the simulation to run within a reasonable amount of computation time.

Table 4: Comparison of the Resolution as a Function of the Number Grid Element, N_{ra}, Used for the Active Area of the Disk Electrode

Number of Element N_{ra}	Dimensionless Steady State Current Z_{ss}	Relative Error %
1	0.75213	24.8
2	0.91624	8.51
3	0.95877	4.12
4	0.97969	2.03
5	0.99154	0.85
6	0.99980	0.02
7	1.00008	-0.008

2.4-2 General Considerations

The purpose of this study is to investigate the cyclic voltammetric responses of microelectrodes for a wide range of b/a values. The response is examined from the linear diffusion regime observed at high scan rates to the radial diffusion regime observed at steady state and slow scan rates. The critical parameters in this study are the characteristic lengths, a and b, and the scan rate, ν. It will be easier to interpret the results of the simulation if the scan rate can be reduced to a length. The length used is the diffusion layer thickness, δ. $\delta = [2Dt]^{1/2}$, where D is the diffusion coefficient and t is the time the diffusion layer has been developing. In a cyclic voltammetric sweep, the range of the potential is $\Delta E = E_f - E_o$. The scan rate (V/s), $\nu = 2\Delta E/T_t$, or the total time for the sweep is $T_t = 2\Delta E/\nu$.

During a cyclic voltammetric experiment where $E^{o'}$ is roughly midway between E_f and E_o, the diffusion layer associated with the conversion of A to B is generated during approximately half of the total time of the experiment. So, t is taken as $T_t/2$ or:

$$\delta = [2D\Delta E/\nu\,]^{1/2} \qquad [23]$$

For $D = 5x10^{-6}$ cm^2/s and $\Delta E = 0.4$ V, $\delta = 2.00x10^{-3}\nu^{-1/2}$. To compare any experimental data to the simulated results of this paper, simply calculate the experimental diffusion length by substituting the experimental D, ΔE and ν into Equation 23. This assumes $E^{o'}$ is roughly midway between E_f and E_o.

In discussing the steady state current, it will be useful to consider the current at a hemispherical electrode of equivalent area. Oldham and Zoski [13] have shown that the steady state current at a hemispherical electrode can be used to approximate the steady state current at an inlaid disk in a semi-infinite insulating shield if an appropriate area correction is introduced. The circumference of a hemispherical electrode is πr_o, where r_o is the radius of

the hemisphere. The steady state current at a hemisphere electrode is embedded in semi-infinite insulating plane is:

$$i^{ss}_{hemi.} = \pi n F r_o D c^{o}_{A} \qquad [24]$$

The diameter of an inlaid disk is 2a, where a is the radius of the disk; the steady state current for a planar electrode, again embedded in a semi-infinite insulating plane, is:

$$i^{ss}_{disk} = 4nFaDc^{o}_{A} \qquad [25]$$

Thus, these are equivalent when $r_o = 4a/\pi$. i^{ss}_{hemi} can be compared to the inlaid disk current with the normalization $(4/\pi)i^{ss}_{hemi}$. $(4/\pi)i^{ss}_{hemi}$ will be called the area corrected hemisphere current. This correction will be used to verify the simulation when $b/a \rightarrow \infty$, and to find the error associated with using the hemispherical equation in evaluating the steady state current at a microdisk in a finite shield ($b/a < \infty$). All currents presented in this simulation are made dimensionless by this area corrected hemisphere current. That is, from Equation 20, $Z(k)=i(t)/4nFac_A^o$. Z(k) is the current normalized to the steady state current response expected for a planar electrode embedded in a semi-infinite insulating plane. So, if at steady state, transport is limited to radial diffusion above the plane of the electrode, Z(k) = 1; that is, hemispherical diffusion has been established.

The range of responses for Nernstian kinetics is completely characterized by three dimensionless length ratios: δ/a, δ/b and a/b. Three distinct transport regimes are possible, and these are characterized by δ/a and δ/b. The linear transport regime is characterized by $\delta/a \ll 1$, as shown in Figure 2-3a. The other two transport regimes are characterized by radial diffusion. The first occurs when $\delta/a \gg 1$, but $\delta/b < 1$. Under this condition, a hemispherical diffusion zone is established as shown in Figure 2-3c. Here, the diffusion field is established solely above the plane of the electrode. The second radial transport regime is established when $\delta/b \gg 1$. As shown in Figure 2-3d, the diffusion field is then established above and below the plane

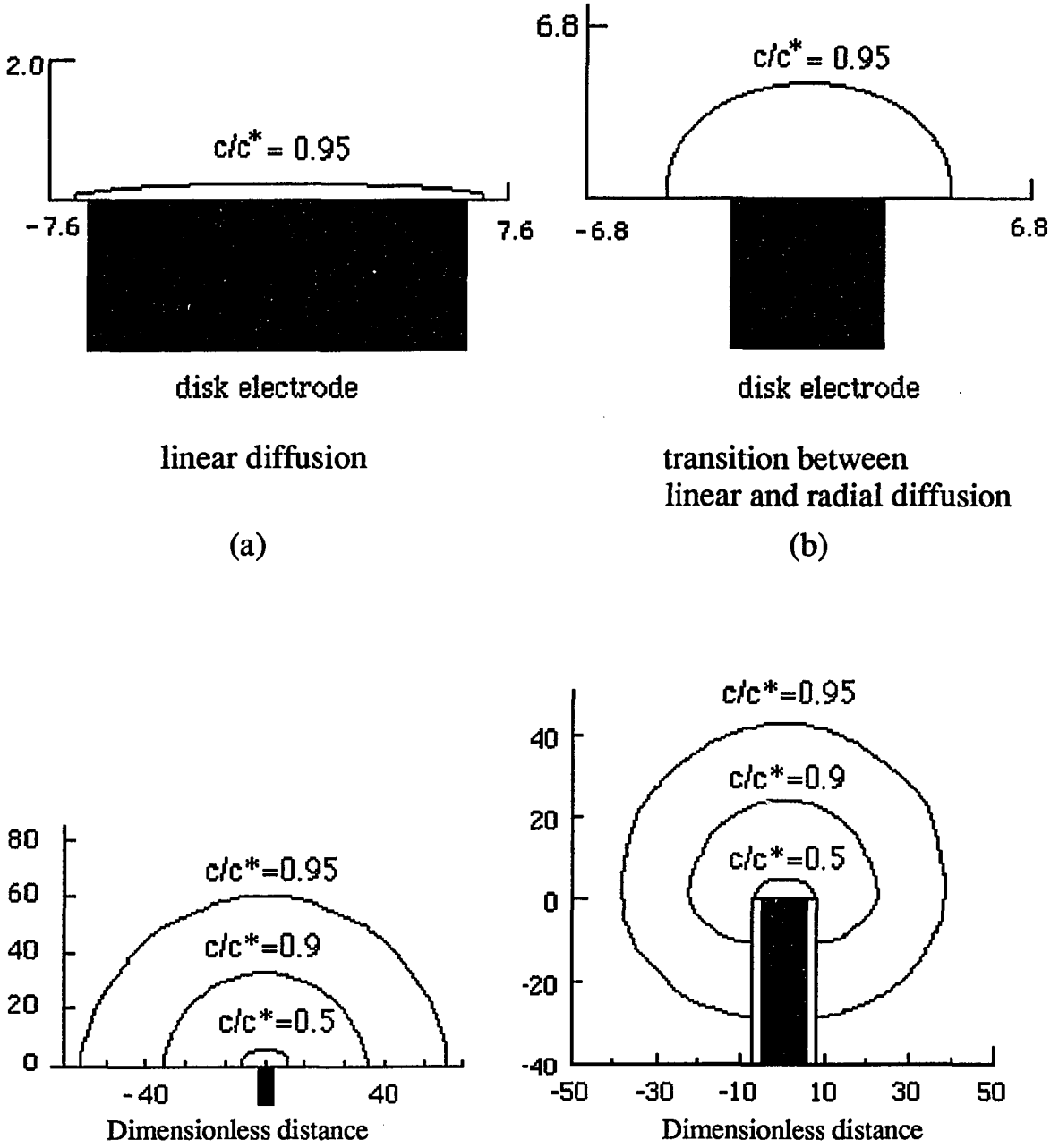

Figure 2-3: Concentration Profiles for Various Transport Regimes.

of the electrode and approaches a spherical profile. As the scan rate slows, b/a will determine whether the hemispherical, spherical or both diffusion zones are reached. When both are reached, the hemispherical regime is the quasi-steady state and spherical regime is the steady state. Figure 2-3 also illustrates a regime of transition between the linear and radial transport regimes. This zone will be of interest in characterizing a and b.

The simulated cyclic voltammetric responses for each of these transport regimes are shown in Figure 2-4. The normal voltammetric response for linear diffusion is shown in Figure 2-4a, where $\delta/a \ll 1$. The sigmoidal responses expected for radial transport processes are shown in Figures 2-4c and d. Note, that while both radial transport processes generate sigmoidal responses, they differ in that the forward and reverse branches of the cyclic voltammogram superimpose for spherical diffusion but not hemispherical diffusion. The transitional response is shown in Figure 2-4b.

Three of the experimental observables are useful in characterizing the geometric parameters of these microelectrodes. The first is the steady state current, i_{ss}. This is the current found when steady state radial diffusion is established. i_{ss} does not vary with scan rate. i_{ss} will be equal to $(4/\pi)i^{ss}_{hemi.}$ if hemispherical diffusion has been established, as in Figure 2-3c, where $\delta \gg a$ and $\delta < b$. i_{ss} will be greater than the area corrected hemispherical current for the steady state spherical diffusion, when sufficient time has been allowed to establish the diffusion profile behind the plane of the electrode, as shown in Figure 2-3d. The higher current arises form the additional flux established from behind the plane of electrode. The experimentally determined i_{ss} is analogous to the dimensionless current, Z_{ss}, shown in Figure 2-4c and d. Whether the steady state is that of hemispherical or spherical diffusion can be determined from the second experimentally useful parameter, $\Delta E_{1/2}$. $\Delta E_{1/2}$ is the difference in potential observed on the forward and reverse branches of a cyclic voltammogram when the current is half the peak current. If hemispherical diffusion has been established, $\Delta E_{1/2}$

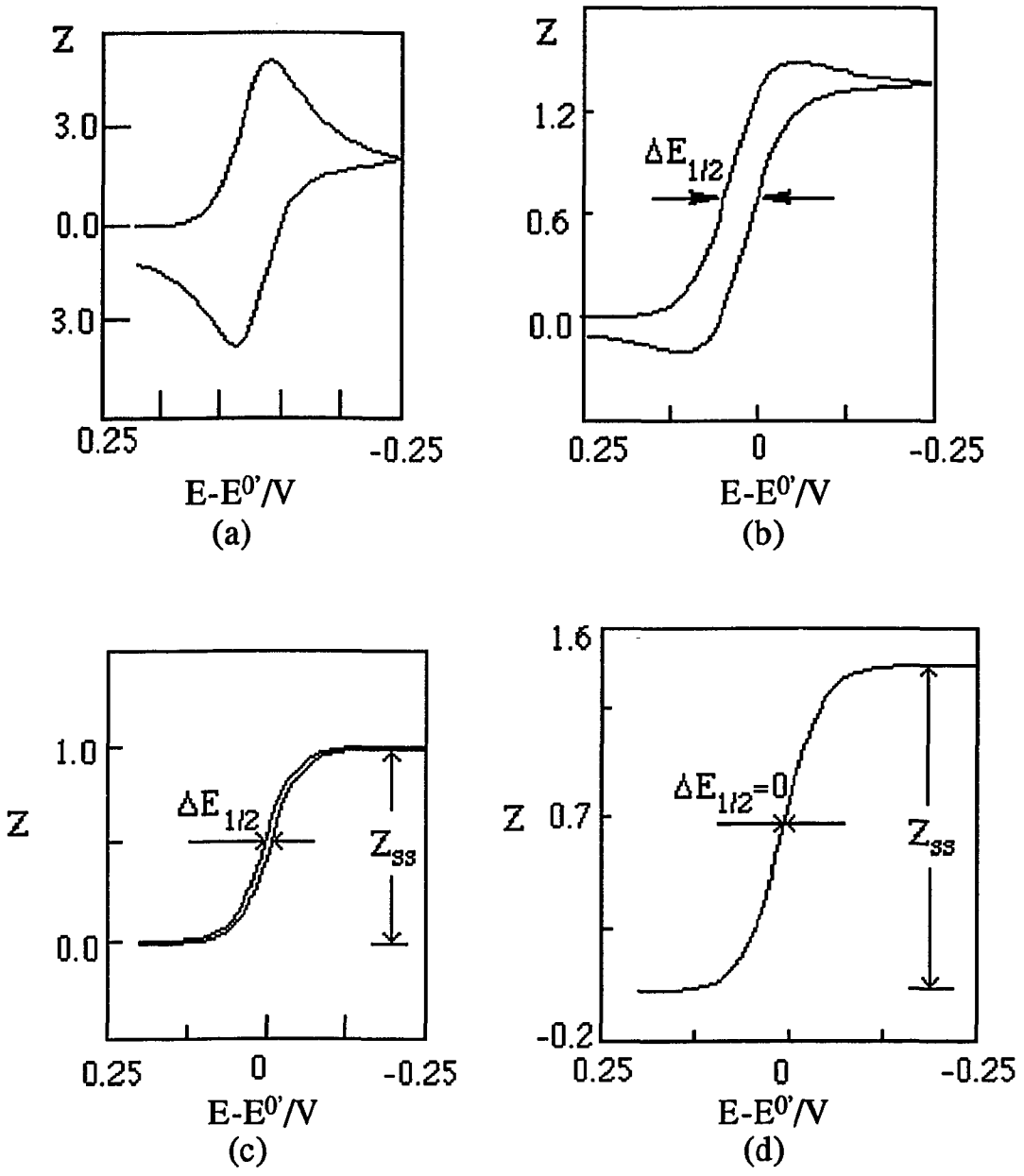

Figure 2-4: Cyclic Voltammograms for Various Cases. (a): $\delta < a$, linear diffusion; (b): $\delta > a$ and $\delta < b$, combination of linear and hemispherical diffusion; (c): $\delta \gg a$ and $\delta < b$, semi-infinite shielding, radial hemispherical diffusion; (d): $\delta \gg a$ and $\delta > b$, finite shielding, radial spherical diffusion.

0. If spherical diffusion has been established, $\Delta E_{1/2} = 0$. The two cases are illustrated in Figure 2-4c and d. The final experimentally parameter is the peak current, Z_p, observed before the response reaches steady state. Z_p is illustrated in Figure 2-4b.

In the following, results will be presented for various values of b/a. The discussion will be broken down into two cases: the finite disk electrode in a semi-infinite shield ($\delta/b < 1$), and the finite disk electrode in a finite shield ($\delta/b > 1$). Note, as along as $\delta/b < 1$, the voltammetric response will be that for an electrode in semi-infinite shield, and the shape of the diffusion field will approach a hemisphere. As δ/b exceeds 1, diffusion from behind the plane of the electrode contributes to the flux, and the diffusion field will approach a sphere.

2.4-3 Disk of Finite Radius in a Semi-Infinite Shield

As δ increases for an inlaid disk electrode with a semi-infinite shield, the diffusion field undergoes a transition from linear to radial diffusion. Because a semi-infinite shield implies $\delta/b < 1$, the steady state diffusion field will be confined above the plane of the electrode and of hemispherical shape. See Figure 2-3b. The cyclic voltammetric curve is expected to undergo a transition from the classical wave shape for linear diffusion to a sigmoidal curve for radial diffusion. The simulation was tested for these conditions and the results are shown in Figure 2-3a,b,c for increasing δ/a (decreasing scan rate). In Figure 2-4a, the classic response for linear diffusion is shown; δ/a is small. As δ increases relative to a and radial diffusion is established above the plane of the electrode, the curve converges on the sigmoidal shape of hemispherical diffusion (Figures 2-4b and c). A residual peak associated with the linear diffusion process is observed in Figure 2-4b. In Figure 2-4c, the peak is gone and the maximum current is the steady state current. $E_{1/2} > 0$.

Steady state is achieved when the peak current has been reduced to the current at the switching potential. Under these conditions, the current is the

steady state current. For purposes of the simulation, the system was taken to be at steady state when i_p was within 0.1 % of i_{ss}. i_{ss} was found to be equal to the area corrected hemisphere current within 0.1 %. At steady state, $\Delta E_{1/2} > 0$. For a point electrode in a semi-infinite shield, no hysteresis is observed. $\Delta E_{1/2} > 0$ characteristic of a flat, inlaid disk of finite radius under hemispherical diffusion conditions.

Hemispherical diffusion occurs when the voltammogram becomes invariant with scan rate, but $\delta/b<1$ and the diffusion field is confined above the plane of the electrode. Hemispherical diffusion is identified by (1) i_{ss} equal to the area corrected hemisphere current; (2) $\Delta E_{1/2} > 0$ at steady state. If a microdisk can be driven into the hemispherical diffusion regime, where $\delta/b < 1$, then the electrode radius, a, is readily determined from the steady state current. $a = i_{ss}/4nFDc^o_A$, where i_{ss} is in amps and c^o_A is the bulk concentration in moles/cm^3.

Alternatively, if the cyclic voltammetric responses can be driven into a linear diffusion regime where $\delta \ll a$, the area of the electrode can be found from the peak current expression for linear diffusion conditions. Linear diffusion is characterized by a linear plot of i_p versus $\nu^{-1/2}$, with a zero intercept. Under these conditions, Nicholson and Shain [23] have shown:

$$i_p = 0.4463nFAc^o_A \left[\frac{nDF\upsilon}{RT}\right]^{1/2} \qquad [26]$$

where A is the electrode area, πa^2. If this method is used, verify the experimentally determined value of a is greater than the longest δ used in the analysis.

It is important to note that a voltammetric response can reach a quasi-steady state when δ is sufficiently large compared to a to establish radial transport from above the plane of the electrode, and yet δ remain less than b. For longer diffusion lengths (slower scan rates), δ may exceed b, and a second transition will be observed. When δ is large compared to b, the true

steady state will be observed with radial diffusion established above and below the plane of the electrode. The hemispherical regime is then a quasi-steady state. The conditions where both a quasi-steady state and a steady state are observed are discussed in the next section.

2.4-4 Disk Electrode of Finite Radius in a Shield of Finite Thickness

When b/a is not infinite, diffusion from behind the plane of the electrode can contribute to the flux at the electrode surface. When this occurs, each of the experimental parameters, i_{ss}, i_p and $\Delta E_{1/2}$, will be affected. Consider each of these in turn.

i_{ss}: When b/a –> ∞, radial diffusion is limited to the plane above the electrode and the steady state current will approach that of the area corrected hemispherical current. Z_{ss}=1. This is illustrated in Figure 2-5, where the response for a semi-infinite shield and a hemispherical electrode of the same area are shown. The forward and reverse branches of the hemispherical electrode superimpose. The forward branch of the inlaid disk with b/a -> ∞, overlays the hemispherical response. The reverse branch is shifted to slightly negative potentials, as is characteristic of a finite inlaid disk in a semi-infinite insulator.

The steady state response for two electrodes with finite values of b/a are also shown in Figure 2-5. At steady state, each of these electrodes has its diffusion field established from both above and below the plane of the electrode. Note, the steady state current increases as b/a decreases. This is consistent with a larger fraction of the total flux coming from below the plane of the electrode as b/a decreases. That is, as b shrinks relative to a, flux around the edges of the insulator to the edges of the electrode becomes increasingly radial, and, therefore, higher. It will be shown below that in the limit of b approaching a, Z_{ss} approaches 1.489; that is, i_{ss} is 1.489 times greater than that predicted by the area corrected hemispherical current or

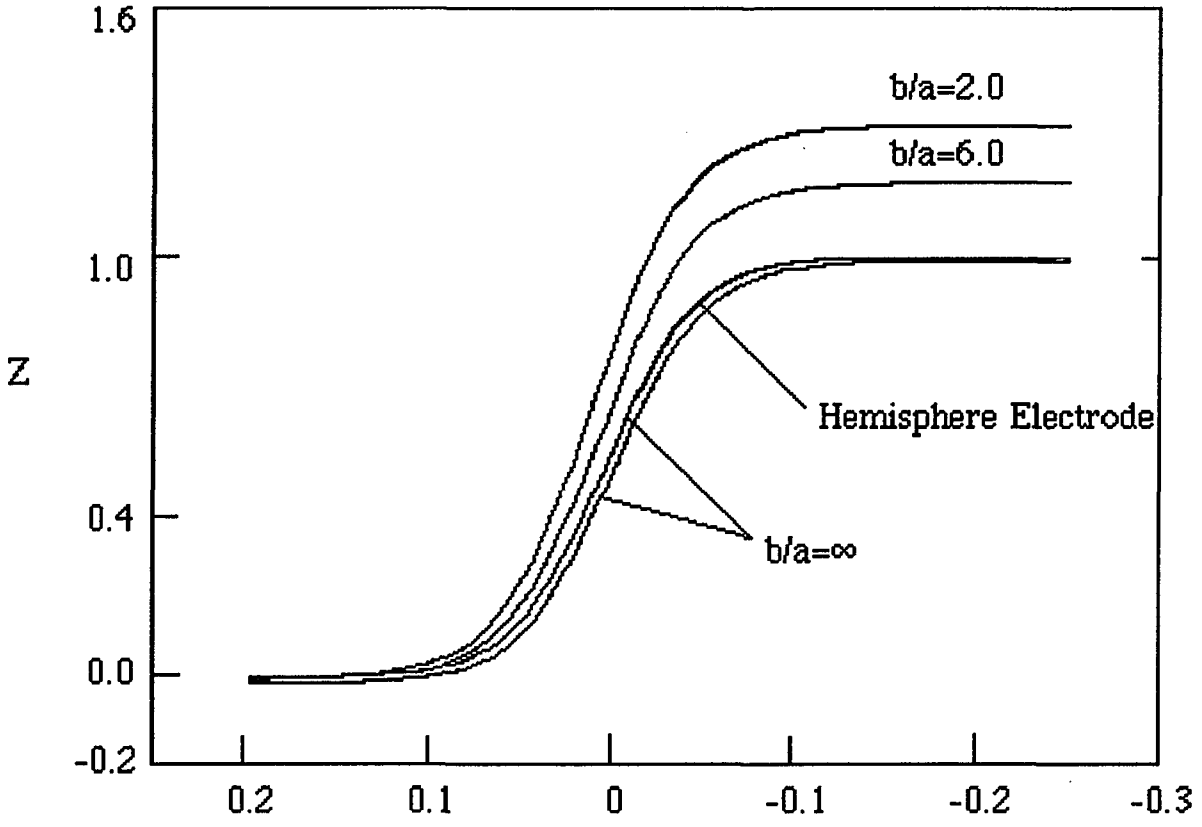

Figure 2-5: Comparison of Simulated Cyclic Voltammograms for Hemisphere Electrode, the Semi-Infinite Shielded Disk Electrode and Two Finite Shielded Electrodes (b/a=2.0 and b/a=6.0).

1.896 $i_{hemi.}^{ss}$. Thus, a substantial error results when the equation for a hemispherical electrode is used to calculate the current response for a disk inlaid in a thin shield. The error approaches a factor of 2 as the shield becomes vanishingly thin. Note, also, that when diffusion is established from behind the plane of the electrode, no hysteresis is observed between the forward and reverse branches of the cyclic voltammogram.

i_p: The simulated current responses for the peak dimensionless current, Z_p, are shown in Figure 2-6 for various values of δ/a and b/a. Z_p is Z_{ss} at steady state. On the plot, all points to the right of the small arrows (Ψ) are restricted to diffusion from above the plane of the electrode ($b > \delta$). For any value of b/a in this regime, Z_p is shown to decrease with decreasing scan rate (increasing δ/a) until $\delta \gg a$, where Z_p equals 1. That is, system has achieved hemispherical diffusion and the maximum current is equal to the area corrected hemispherical current.

All points to the left of the small arrows in Figure 2-6, have some component of radial diffusion from behind the plane of the electrode. As b/a decreases, this flux component contributes an increasing fraction of the total flux to the electrode, and the diffusion field is increasingly spherical. This is increasingly spherical. For a given scan rate, Z_p increases as b/a decreases. This is expected as the system moves from a roughly hemispherical diffusion profile toward a spherical profile. For small values of b/a, note Z_p is scan rate (δ/a) independent. The system is at steady state; $Z_p = Z_{ss}$. Upon taking the convergence of two curves as an indication of the onset of steady state, the system is roughly at steady state once $\delta/a > 5b/a$ or $\delta > 5b$. For $a < \delta < 5b$, Z_p will be a function b/a and δ. As b/a decreases, the system approaches steady state at higher scan rates (smaller δ/a). This means the greater the flux from behind the plane of the electrode, the more quickly the system is driven to steady state. The smaller b/a, the smaller the time window the system spends in transition from linear to radial diffusion, and the less obvious the current peaks associated with the linear diffusion components.

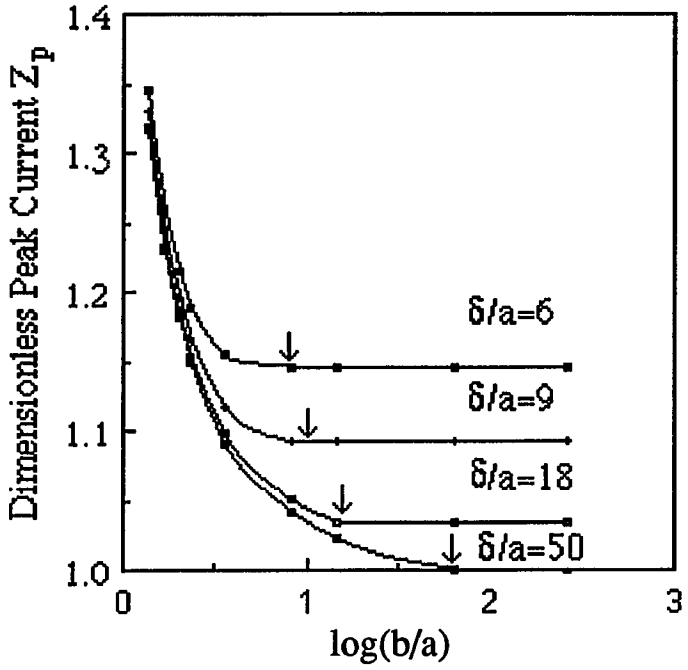

Figure 2-6: The Effect of the Ratio of Shielding Radius to Disk Radius (b/a) on the Dimensionless Peak Current Z_p at the Different Ratios of Scan Rate to Disk Radius δ/a. For fixed a, the scan rate slows as δ/a increases. To the right of the arrow on each curve, diffusion is constrained to above the plane of the electrode because $\delta < b$.

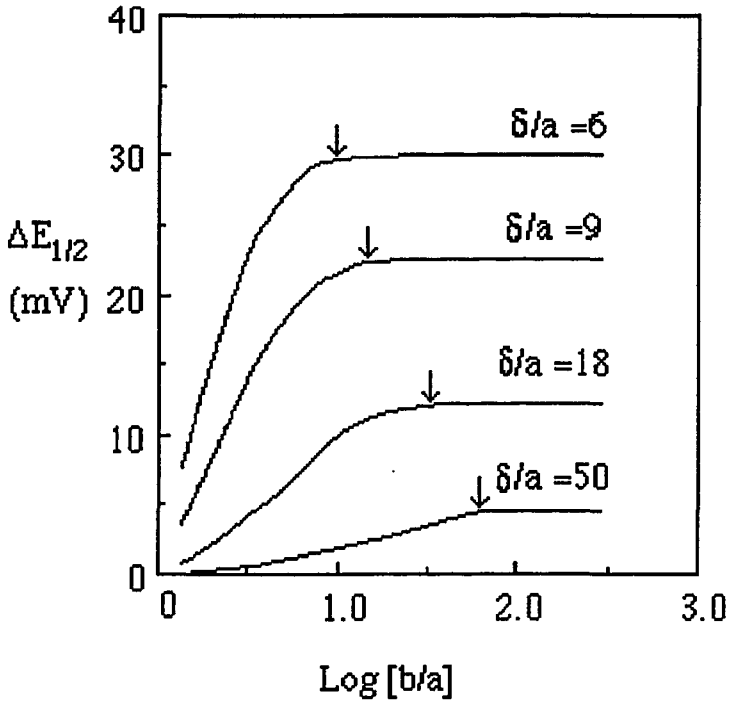

Figure 2-7: The Effect of Ratio of Shielding Radius to Disk Radius (b/a) on $\Delta E_{1/2}$.

$\Delta E_{1/2}$: The variation of $\Delta E_{1/2}$ with δ/a and b/a is shown in Figure 2-7. Again, all the data to the right of the small arrows corresponds to a condition where $b > \delta$. When $b > \delta$, $\Delta E_{1/2}$ decreases as δ/a increases (scan rate decreases) as is expected for the simple transition from linear to hemispherical diffusion. Once δ/a =50, the system is at steady state, but $\Delta E_{1/2}$ is still greater than zero, as expected for hemispherical diffusion and a finite disk radius.

The data to the left of the small arrows corresponds to a regime where some fraction of the total flux to the electrode comes from behind the plane of the electrode. As b/a decreases for fixed δ/a, an increasing fraction of the flux is from behind the plane of the electrode and system has an increasingly spherical diffusion profile. Consistent with this, $\Delta E_{1/2}$ decreases. For a given value of b/a, $\Delta E_{1/2}$ decreases as δ/a increases (scan rate decreases) as the system passes from linear to spherical diffusion. For very small values of b/a, the system approaches spherical diffusion at faster scan rates (smaller δ/a) because the substantial flux from behind the plane of the electrode decreases the time require for transition from linear to radial diffusion. $\Delta E_{1/2}$ approaches 0 as the steady state spherical diffusion profile is established.

2.4-5 Prediction of Inlaid Microdisk Electrode Radii a and b

The simulation results can be used to predict disk radius, a, and the shield length plus disk radius, b, of the inlaid microdisk electrode with a finite shield. From Figures 2-5 and 2-6, the dimensionless steady state current of a disk embedded in a finite shield increases as the ratio of b/a decreases. The current will be enhanced by diffusion not only from the above the plane of the electrode but also from the behind the plane of the electrode. This relationship is illustrated quantitatively in Figure 2-8. In Figure 2-8, when the a/b approaches zero, the system is the inlaid disk embedded in a semi-infinite shield, and Z_{ss} equals 1. The steady state current

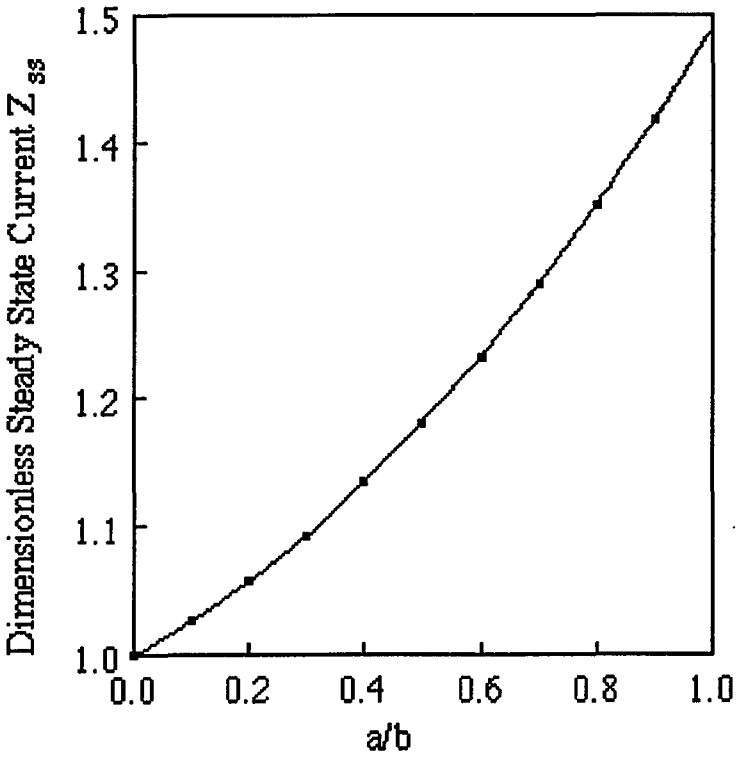

Figure 2-8: The Relationship Between the Dimensionless Steady State Current, Z_{ss}, and the Ratio of Disk to Shielding Radii.

is equal to the steady state current of hemispherical electrode after area correction. See Equation 25. In the limiting case when the a/b approaches 1.0, the shield thickness approaches zero. This corresponds to a concentration profile with the maximum spherical character surrounding the electrode, and the maximum flux to the electrode surface. The maximum dimensionless current will be 1.489. Oldman [24] and coworkers, Myland [25] used conformal mapping to derive an analytical expression for this limiting case. They found a value which corresponds to a maximum dimensionless current of 1.492. The results are within 0.2%.

A second order polynomial fit to the data shown in Figure 2-8, shows the steady state response of an electrode with a finite shield is related to the response for an infinite shield as:

$$\frac{i^{ss}_{inlaid}}{i^{ss}_{inlaid,\ b/a\ ->\infty}} = 1.000 + 0.234[\frac{a}{b}] + 0.255[\frac{a}{b}]^2 \qquad [27]$$

R^2=1.000

Thus, if a is known and the system can be driven to steady state, b is readily determined from the steady state current.

If neither a nor b is known, the relationship developed below will be useful in determining a and b. The method uses both steady state and non-steady state data. The relationship relies on values of i_p, the peak current at a scan rate where the system is not yet at steady state, and i_{ss}, which is scan rate independent. The relationship is parametrized by $(i_p - i_{ss})/i_{ss}$, b/a, and δ. The working curves are shown in Figure 2-9. This Figure shows the percent represented by $(i_p - i_{ss})/i_{ss}$ at two scan rates (δ) can be used to find b/a and (b-a)/δ. i_{ss} can be measured directly at sufficiently slow scan rates; that is, the steady state current is constant independent of further decreases in the scan rate. Now, cyclic voltammograms are recorded at two scan rates, v_1 and v_2,

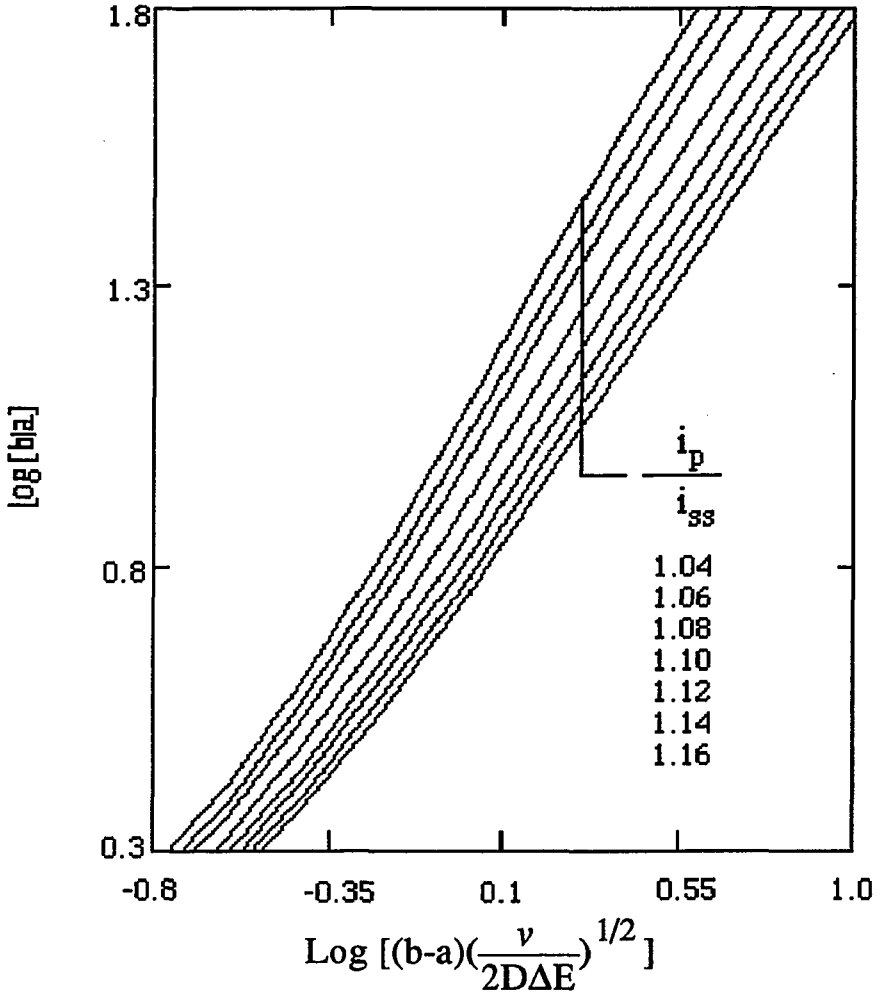

Figure 2-9: Working Curve for the Prediction of the Disk Radius and the Shielding Radius. ΔE is $|E_o - E_f|$, the difference of the initial scanning potential with the formal potential, $E^{o'}$, of an electrode is set as 0.2 V, and the difference of the switching potential in CV with the formal potential is set as 0.25 V in this working curve.

both fast enough that the response shows some peak current. Let $A_1 = (i_{p1} - i_{ss})/i_{ss}$ at ν_1, and $A_2 = (i_{p2} - i_{ss})/i_{ss}$ at ν_2. A_1 and A_2 can be used to find a and b either by an analytical method or by using a working curve.

Consider the analytical method first. A cubic equation has been used to fit each of the curves shown in Figure 2-9. The equations are of the form:

$$\text{Log}[\frac{b}{a}] = B_1 + B_2 \text{Log}[(b-a)(\frac{\nu}{2D\Delta E})^{1/2}] + B_3 \{\text{Log}[(b-a)(\frac{\nu}{2D\Delta E})^{1/2}]^2\}$$

$$+ B_4\{\text{Log}[(b-a)(\frac{\nu}{2D\Delta E})^{1/2}]^3\} \qquad [28]$$

The coefficients, B_o, B_o, B_2 and B_3, are tabulated in Table 5. To find a and b from a set of experimental results, appropriate coefficients are selected based on A_1 and A_2. This results in a pair of simultaneous cubic equations, as shown is Equation 28. With two equations, in two unknowns, b/a and $(b-a)(\nu/(2D\Delta E)^{1/2}$, a and b can be found by solving the equation simultaneously. Usually, Equation 28 will have three real roots, but it is easy to distinguish which is the correct answer. Based on experimental determinations, discussed below, the precision of the method is ± 7%. The equations can be used to arrive at a first approximation to b/a and (b-a), and then the values further refined by fitting the two cubic equations.

Consider the working curve method. A_1 and A_2 are known at ν_1 and ν_2.

$$\log[(b-a)/(\nu_1/(2D\Delta E)^{1/2}] - \log[(b-a)/(\nu_2/(2D\Delta E)^{1/2}] =$$

$$\log[1/(\nu_1/(2D\Delta E)^{1/2}] - \log[1/(\nu_2/(2D\Delta E)^{1/2}] \qquad [29]$$

which corresponds to a certain displacement between the curves that correspond to A_1 and A_2. The working curve is used by sliding down the curve for A_1 until the curve for A_2 is displaced from the curve for A_1 by $\log[1/(\nu_1/(2D\Delta E)^{1/2}] - \log[1/(\nu_2/(2D\Delta E)^{1/2}]$. At this point, the value on the y

axis corresponds to log[b/a], and the value on the x axis for say A_1 corresponds to $\log[(b-a)/(\nu_1/(2D\Delta E)^{1/2}]$. The A_2 curve could be used as well. With this information, b and a can be determined.

Table 5: The Coefficients in Equation 28 to Evaluate b/a and b-a.

i_p/i_{ss}	B_0	B_1	B_2	B_3
1.04	1.0765	1.2359	0.09651	-0.22640
1.05	1.0241	1.2068	0.10448	-0.22957
1.06	0.9800	1.1808	9,11679	-0.22679
1.08	0.90836	1.1330	0.14336	-0.21204
1.10	0.85217	1.0904	0.16497	-0.19445
1.12	0.80895	1.0425	0.16000	-0.14597
1.14	0.77176	1.0104	0.16423	-0.12747
0.16	0.73985	0.98403	0.16740	-0.11424

To summarize, a and b can be determined as follows.

1) If the shield is of infinite thickness and steady state can be reached, a can be found using the area corrected hemispherical current, as in Equation 25.

2) If a is already known, and b is known to be less than δ at steady state ($\Delta E_{1/2}=0$), b can be calculated using Equation 27, or extracted from Figure 2-8.

3) If a and b are both unknown, several steps are needed to find both values. First, take a cyclic voltammogram at a sufficiently slow sweep rate to achieve steady state. If $\Delta E_{1/2} > 0$ at steady state over all scan rates of interest,

the system is characterized by a alone; see Equation 25. If $\Delta E_{1/2} = 0$, then it is necessary to find both a and b. Then, process, as outlined above, to find A_1 and A_2 for two scan rates which are fast enough to generate cyclic voltammograms with peak currents, and use the results with either Equation 28 or Figure 2-9.

2-4.6 Experimental Results

The redox species of potassium ferricyanide (2.0 mM) with sodium sulfate (0.1 M) and dopamine (2.0 mM) with HCl (0.1 M) were used as test solutions to evaluate the simulation results. The test solution had been degased by N_2 for half an hour before the measurement. The CV was run at the different scan rates. Ferricyanide was reduced by one electron and dopamine was oxidized by two electrons. Both reactions are reversible. The diffusion coefficients of two redox couples are 6.5×10^{-6} and 6.4×10^{-6}, respectively. [26,27]

Two finite glass shielded microelectrodes with radii a_1 and a_2, and the different shield radii, b_1 and b_2, were used. The shield radii were determined by scanning electron microscopy. Both steady state and non-steady state cyclic voltammograms were recorded. Values of a and b were determined as outlined above and compared to the known values of a and b. The measured results are summarized in Tables 6 and 7.

From Tables 6 and 7, the simulation results are reasonably close to the experimental results, especially for the data from method 1, where the results are within 2%. It was noted in the SEM the disk was not perfectly. This causes the actual area of the disk to be larger than the calculated area and it disrupts the diffusion field. For method 2, the difference about ±7%, whether the results were calculated by the cubic equation 28 or found from Figure 2-8. 7% reflects the accuracy of determining the experimental steady state current. The theoretical accuracy is limited to the accuracy of the simulation, 0.2%.

Table 6: Comparison of Experiment and Simulation Results for $K_3Fe(CN)_6$ (2.0 mM) in Na_2SO_4 Solution (0.1 M) Using Carbon Fiber Disk Electrode with Glass Shield

Parameters	Experiment Data		Simulation Data	
	SEM	CV	Method 1[1]	Method 2[2]
a (μm)	3.5		3.5	3.2
b (μm)	20.1		21	18.4
a/b	0.174		0.179	0.174
i_{ss} (nA)		1.85	1.83	1.85
Z_{ss}		1.05	1.04	

Table 7: Comparison of Experiment and Simulation Results for Dopamine (2.0 mM) in HCl (0.1 M) Solution Using Carbon Fiber Disk Electrode with Glass Shield.

Parameters	Experiment Data		Simulation Data	
	SEM	CV	Method 1[1]	Method 2[2]
a (μm)	4.0		4.0	4.4
b (μm)	15.0		15	16.0
a/b	0.276		0.276	0.275
i_{ss} (nA)		4.50	4.47	4.50
Z_{ss}		1.09	1.08	

[1] The data were calculated from Equations 27 and Figure 2-8.

[2] The data were calculated from Equation 28 and Figure 2-9.

2.5 SUMMARY

1) The new, two dimensional irregular EESG method has been successfully employed in the simulation of the cyclic voltammetric response of inlaid disks with shields of thickness comparable the electrode radius. This method improves the precision and accuracy of the simulation of the voltammetric response of inlaid microdisk electrode. The improvement arises from a more accurate simulation of the edge effects at the interfaces of the disk and insulator, and insulator and solution.

2) As the ratio of the disk radius, a, to the insulator plus disk radius increases, the normalized steady state current increases. In the limiting of equal disk and insulator radii, the steady state current is 49% higher than the current for a semi-infinite insulator. The relationship between the steady state current and the ratio of the disk to the disk plus insulator radii has been found from the simulation and verified with experimental results.

3) For inlaid disks with shields of finite length, diffusion from behind the plane of the electrode not only affects the magnitude of the steady state current, but also alters the shape of the voltammetric curve. At steady state, flux from behind the plane of the electrode brings the diffusion field closer to a spherical geometry. When the diffusion field is sufficiently spherical, the steady state response exhibits a superposition of the forward and reverse branches of the voltammetric response; $\Delta E_{1/2}$ approaches to zero.

4) The simulation provides two different ways to predict the radius of the inlaid disk, a, and the radius of the insulating shield plused disk, b, from simple experimental results. The accuracy, within 7%, is limited by the precision in determining the experimental current.

CHAPTER III
Surface Diffusion in a Microstructured, Ion Exchange Matrix: Nafion/Nuclepore Composite Membranes

3.1 INTRODUCTION

The development of systems with controlled chemical architecture has been an area of interest, especially among electrochemists, for the last several years. In these systems, the goal is to engineer devices with dimensions ranging from submicron to those approaching molecular. Efforts along these lines include the charge separation devices of Mallouk and coworkers [1-4]. In these systems, clay particles are modified in such a way that a photon captured on one side of the particle is converted to an electron and the electron is effectively shuttled to the other side of the particle to collect the energy and reduce recombination losses. Wrighton and coworkers [5-11] have been detailing the individual steps necessary to the construction of molecular transistors. Because of their small dimensions, molecular electronic devices would both speed computations and increase the density of stored electronic information. Faulkner and coworkers [12-13] have been working in the area of microstructured matrices on electrodes. The technical problems of building ultramicroelectrodes have been addressed. Band electrodes as small as 0.5 nm have been built by White and coworkers [14], and disks of nanometers have been built by Lewis and coworkers [15]. Such small electrodes provide some interesting substrates for designing microstructured reactors.

In these systems, the focus has been on how to build small structures and how to shuttle electrons in a structured matrix where the molecular species are immobilized. If notions of systems with controlled chemical architecture are extrapolated to their limit, dynamic devices will be developed. That is,

instead of switches and electron collectors, microstructured chemical reactors will be considered. Such reactors have the additional complexities of arranging selective transport of desired reactants and products as well as facile transport of these species through the micro-structured matrix.

Here, we reported on a microstructured system which can serve as a prototype and model system for selective, molecular pipes. The system is formed by adsorbing Nafion, a perfluorinated, sulfonic acid cation exchange polymer, into the straight, cylindrical pores of Nuclepore membranes [16]. The pores, produced by neutron track etching, are available with well-controlled diameters of 15, 30, 50, 80, 100 and 600 nm. The flux of cations through these composites is monitored by steady state voltammetry. The selectivity of these composites is governed by the Nafion while the pores in the Nuclepore membranes provide a pipe like structure through which transport occurs.

In all of these systems, as structures decrease in size, the ratio of surface area to volume increases. Thus, interfacial processes which are not important in bulk systems may come to play a major role in dictating the behavior of microstructural systems. The interfacial processes most likely to be important in microstructural systems are those which generate a steep but short range gradient at the interface. Examples include electrostatic effects, migration, magnetic gradients, surface tension and surface diffusion. In designing microstructured transport systems, these interfacial effects can be capitalized upon to build systems of rapid and selective transport.

For pores of 30 nm or greater, we find the flux through the Nafion-filled pores of the Nafion/Nuclepore composites increases as the diameter of the pores decreases. We propose that this increase in flux is due to surface diffusion along the pore walls of the Nuclepore support. Nafion acts as an extraction matrix, which concentrates cations within the pores. Transport rates in Nafion are relatively slow (of the order of $10^{-8}cm^2/s$). If transport along the pore walls is more facile than transport in Nafion, then the

following can be envision as a description of the environment within the composites. The concentration of ions near the wall will be depleted more rapidly than in the Nafion in the center of the pore. This will create a concentration gradient which will drive the redox species to move radially to the wall, where they are rapidly shuttled through the composite to the electrode by surface diffusion. Thus, the flux enhancement observed in these membranes is a two component process: Nafion drives up the concentration of cations by partitioning redox species into the pores and effective transport is supplied as surface diffusion along the pore walls of the Nuclepore support. This model is illustrated in Figure 3-1.

Based on this description, two things can be anticipated. First, that transport through the Nafion portion of the composites is more rapid than transport through a simple Nafion film. This is observed. Second, as the pore size shrinks, a diameter must be found where the volume of Nafion which extracts cations is optimized for the pore surface area available for surface diffusion. This is also observed. A mathematical description of this combination of partitioning and surface diffusion is presented to model the experimental system. Some notions are outlined about what can be done to optimize transport and selectivity in these composites and in similar systems where surface diffusion plays a role. Interfacial gradients are pointed out as a unique asset of microstructural systems. If we are clever, we will capitalize on these interfacial effects in engineering tailored transport and selectivity into systems of controlled chemical architecture.

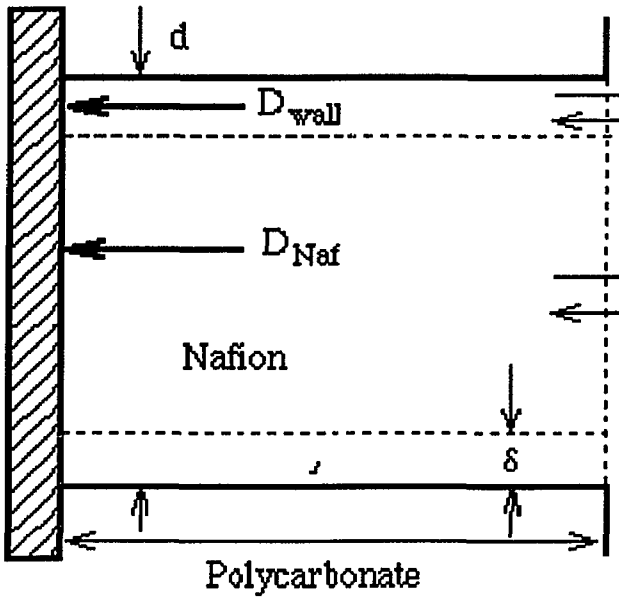

(a)

$$J_{bulk} = \frac{\varepsilon c^{*} \kappa_{Naf} D_{Naf}}{l}$$

$$J_{wall} = \frac{A_{wall}}{A_{pore}} \frac{\varepsilon c^{*} \kappa_{wall} D_{wall}}{l}$$

$$\frac{A_{wall}}{A_{pore}} \approx \frac{2\pi r_o \delta}{\pi r_o^2} = \frac{2\delta}{r_o}$$

$$J_{wall} = \frac{4\delta \varepsilon c^{*} \kappa_{wall} D_{wall}}{d l}$$

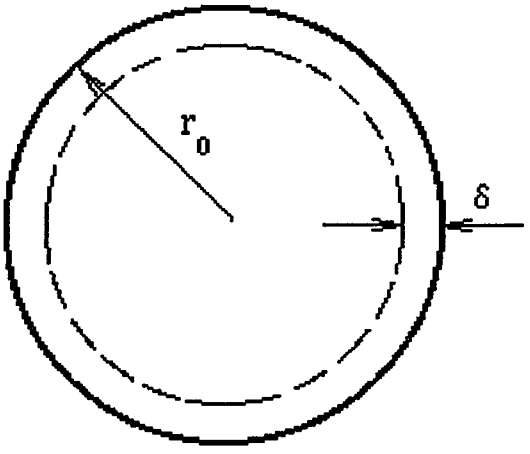

(b)

Figure 3-1: Diagram Illustrating the Transport and Selectivity Parameters Used in the Proposed Model of Flux Through the Pores of the Nafion /Nuclepore Composites. (a) a cross section through the length of the pore; (b) a radial cross section of the pore.

3.2 EXPERIMENTAL

3.2-1 Formation of Composites

Composites were formed by adsorbing Nafion into Nuclepore neutron track etched polycarbonate membranes. These membranes are transversed by numerous, parallel, small diameter cylindrical pores. The nominal pore diameters used here were 15, 30, 50, 100 and 600 nm, as reported by Nuclepore. The membranes were soaked for 30 minutes in a commercially available suspension of Nafion in a mixture of water and alcohols (Solution Technologies). The concentration of Nafion is 5 g per 100 ml of solution. As shown previously [16], no additional Nafion is sorbed into the Nuclepore membrane after 30 minutes. Unlike the previous studies of these composites, the composites were blotted briefly upon removal from the soaking solution to remove the excess Nafion suspension adhering to the outer surfaces of the membrane. The composites were then dried overnight in a vacuum desiccator.

3.2-2 Formation of Nafion Films

In some studies, transport rates through the composites were compared to transport through simple Nafion films. Nafion films were formed by pipeting 10 μl of Nafion suspension onto the glassy carbon electrode and allowing the solvent to evaporate. The modified electrode was then placed in a solution of electrolyte and redox species to perform the electrochemical studies. The density of wetted Nafion is 1.58 g/cm^3 [33]. For an electrode area of 0.458 cm^2, 10 μl of Nafion suspension yields a film thickness of 6.9 μm. This thickness is comparable to the thickness of the Nuclepore membranes.

3.2-3 Electrochemical Measurements

A plastic cap with a whole in its center was used to mount the composites on a glassy carbon disk (area = 0.458 cm^2) inlaid in teflon. The composites

were examined in an aqueous solution of 2.0 mM dopamine hydrochloride (Aldrich Chemicals) and 0.1 M nitric acid. At this concentration of acid, the dopamine remains a protonated cation, Dop^+. The membranes were allowed to equilibrate overnight with the redox solution. Cyclic voltammetric sweeps were performed to ensure the quality of the composite. Mass transport rates through the composites were determined by the steady state oxidation of dopamine at a rotating disk. Rotation speeds between 200 and 1500 rpms were employed. Dop^+ was electrolyzed for 30 minutes through the film before the steady state values were recorded. The measurements were made with a Pine ASR Rotator, PAR 273 Potentiostat, and Norland IQ 400 Digital Processing Oscilloscope. No positive feedback was employed. Similar measurements were made previously [16], and will discussed here. These include the following redox systems: 4 mM hydroquinone (H_2Q, Baker Chemicals) in 0.1 M HNO_3, 4 mM H_2Q in 0.1 H_2SO_4, 2 mM trimethyl-amminomethyl ferrocene (FeN^+, Alfa Products) in 0.1 H_2SO_4. These studies were similar to the dopamine studies except not effort was made remove the excess Nafion from the surface of the composites, the composites were dried in air, not vacuum, over night, and feedback compensation was employed.

3.3 RESULTS

3.3-1 General Consideration

Numerous studies of transport through thin films and polymer layers have been performed by steady state rotating disk voltammetry [17-31]. The advantage of steady state rotating disk studies is the ready interpretation of the results. If a redox species is moving through a film at steady state and it undergoes no chemical reactions or physical interactions which cause its concentration gradient normal to the surface of the electrode to deviate from a constant value, then the Koutecky-Levich plot, i_{lim}^{-1} versus $\omega^{1/2}$, will be linear [17-21;27]. i_{lim} is the steady state current measured at the electrode

surface at a given rotation rate, ω, reported in radians per second.

Under these conditions, i_{lim} is expressed as follows,

$$\frac{1}{i_{lim}} = \frac{1}{i_{memb}} + \frac{1}{i_{soln}} \qquad [1]$$

where, i_{memb} is characteristic of transport in the film, and i_{soln} is characteristic of transport in the solution. i_{memb} is rotation rate independent. i_{soln} is the steady state current measured at the same electrode in the absence of a film.

$$i_{soln} = 0.620nFAD_s^{1/2} \nu^{-1/6} c^* \omega^{1/2} \qquad [2]$$

Thus, a plot of i_{lim}^{-1} versus $\omega^{-1/2}$ will have a slope related to the solution parameters: c^* is the solution concentration (moles/cm^3), ν is the kinetic viscosity (cm^2/s), and D_s is the diffusion coefficient of the redox species in the solution (cm^2/s). n, F, and A, are, respectively, the number of electron transferred, Faraday's constant and the electrode area. The intercept of the Koutecky-Levich plot will be characteristic of transport in the film. The structure of the film and the nature of the transport processes within the film will determine how i_{memb} is expressed parametrically. i_{memb} is most readily parametrized when the structural features of the film are small compared to the thickness of the hydrodynamics boundary layer. This condition is met by all the systems studied here. That is, $r_o, N^{-1/2} \ll 1.61 D_s^{1/3} \omega^{1/2} \nu^{-1/6}$ in all cases, where r_o is the radius of the pores in the Nuclepore membranes. N is the number of pores per squared centimeter, so $N^{-1/2}$ is the average distance between adjacent pores. Under these conditions, the layer modifying the electrode surface is effectively a homogeneous transport zone characterized by transport rates and concentrations different from those in solution. The flux of a redox species moving from the solution to the electrode through the modifying layer is not disrupted by local geometric features. The concentration gradient through the film remains constant, and is

characterized by an effective transport rate and an effective concentration.

Note, that when the value of i_{memb} becomes extremely small, i_{memb}^{-1} » i_{soln}^{-1}. Under these conditions, i_{soln}^{-1} may become comparable to the noise in the measurement of i_{lim}^{-1}, and the Koutecky-Levich plot may appear to be rotation rate independent. In the following studies, when this occurred i_{memb} was taken as the average of i_{lim} recorded at all rotation rates. When the average was used, it will be noted. In all cases, the average was within 10 % of the intercept.

3.3-2 Experimental Studies

The steady state, rotating disk studies were performed on dopamine under the experimental conditions outlined in Table 1. Similar conditions are also summarized for the four systems studied previously. In all cases, the electrolyte concentration was 0.1 M. For all five systems, the measurements at an unmodified electrode yielded Koutecky-Levich plots with intercepts of zero, as expected. The solution diffusion coefficients, D_s, were calculated from the slopes of these plots. The averaged results are also reported in Table 1.

Table 1: Solution Parameters

	Dop^+ HNO_3	H_2Q H_2SO_4	H_2Q H_2SO_4	$FerN^+$ HNO_3	RuN^{3+} HNO_3
c^* (μmoles/cm^3)	2.0	4.0	4.0	2.0	2.0
n	2	2	2	1	1
D_s (10^{-6} cm^2/s)	6.47	9.38	9.27	6.7	7.32

3-3.3 Porosity (ε) and Thickness (*l*) Measurements

To interpret the data for the composites, it will be necessary to know the porosity of these membranes. Nuclepore membranes with pore diameters of 15, 30, 50, 80, 100 and 600 nm were employed in these studies. When no Nafion is present in the membrane, the pores are filled with the bulk solution and the redox species will have the same diffusion coefficient as in bulk solution and the redox species will have the same diffusion coefficient as in bulk solution. Under these conditions, the porosity can be determined from the Koutecky-Levich plot, where i_{memb}, determined from the intercept, is interpreted as

$$i_{No\ Naf} = \frac{nFAD_s c^* \varepsilon}{l} \qquad [3]$$

where $i_{No\ Naf}$ is characteristic of transport through the pore in the absence of Nafion (A), l is the thickness of the membrane, and ε is the porosity.

l, tabulated in Table 2, was determined previously [16] by interference fringes in the infrared spectra. For all membranes with $2r_o \leq 100$ nm, the membranes have a nominal thickness of 6 μm. The membranes thin as the etching process widens the pores. The experimentally determined thicknesses for diameters of 15, 30 and 100 nm vary linearly with the corresponding thickness. For r_o and l expressed in microns, linear regression yields the following equation with a correlation coefficient of 0.999.

$$5.902 - 8.073\ r_o = l \qquad [4]$$

Then, l for the 50 and 80 nm diameter pore membranes are approximated as 5.70 and 5.58 μm, respectively. Once l is known, the porosity can be determined from the steady state rotating disks measurements, according to Equation 3. For straight cylindrical pores, $\varepsilon = N\pi r_o^2/cm^2$, where N is the number of pores/cm^2 and r_o is the radius of the pore. The experimentally determined values of ε and N are also cited in Table 2.

Table 2: Membrane Parameters

$2r_0$ (nm)	15	30	50	80	100	600
l (μm)[a]	5.85	5.77	5.70[b]	5.58[b]	5.50	9.68
ε [c]		0.02022	0.0568		0.0595	0.1423
ε [d]	0.0086	0.0104		0.075	0.063	0.115
N [e] (10^9pores/cm^2)		0.715	0.723		0.189	0.0126

a) Found previously [16], by interference fringes in the infrared.

b) Values approximated from Equation 4, as discussed in the text.

c) Porosity found from steady state rotating disk measurements, according to Equation 3.

d) Porosity found in Ref. 16, which is appropriate to H_2Q, RuN and FerN analysis.

e) $N = \varepsilon/\pi r_o^2$, and applies to the dopamine system studied here.

3.3-4 Nafion Films

Transport through a Nafion film is parametrized by the film thickness (l), diffusion coefficient of the redox species in Nafion (D_{Naf}), and a partition coefficient, (κ_{Naf}). When Nafion is hydrated, it forms a microstructured matrix because the hydrophobic fluorocarbon backbone segregates from the hydrophilic sulfonic acid sites [32]. However, because these microstructural features are small compared to the thickness of the hydrodynamics layer in solution, the film can be treated as effectively homogeneous under steady state rotating disk conditions. $\varepsilon = 1$. For a Nafion film, i_{memb}, taken from the intercept of the Koutecky-Levich plot, is interpreted as

$$i_{Naf} = \frac{nFAD_{Naf}c^{*}\kappa_{Naf}}{l} \qquad [5]$$

l was calculated from the volume of the Nafion solution used to prepare the film, the concentration of the Nafion solution, the density of wet Nafion (1.59 g/cm^3) [33], and the area of the electrode. For films formed with 10 µl of Nafion suspension, film thicknesses were taken as 6.9 µm. The steady state rotating disk studies of simple Nafion films yielded values of $D_{Naf}\kappa_{Naf}$, as shown in Table 3 under the label Nafion films.

3-3.5 Composite Membranes

Steady state rotating disk studies were made for the composite membranes with pore sizes ranging from 15 to 600 nm. The intercept of the Koutecky-Levich plot for the composites is denoted i_{comp}. The normalization by l, n, and ε is necessary if the flux characteristics of the composites are to be compared for different pore radii and different redox systems. The appropriate normalization is $i_{comp}l/nFAc^{*}\varepsilon$, which has units of cm^2/s, consistent with a transport rate. The detailed interpretation of this value is presented in the Model and Discussion sections. Essentially, this

normalization yields a parameter characteristic of transport and extraction in the Nafion filled regions of the pore; it corrects for the polycarbonate portion of the membrane which is impermeable precludes flux enhancement. Values of $i_{comp}l/nFAc^{*}\varepsilon$ for dopamine as a function of r_o are summarized in Table 3. Each reported values is the average of 3 to 6 determinations, with a relative standard deviation of less than 20%, except for 50 nm composites where the relative standard deviation is 33%. Such variation are typical of polymer measurements is general and composites in particular. Results are also summarized for the previously studied systems. $i_{comp}l/nFAc^{*}\varepsilon$ versus the $\log(r_o)$ is ploted in Figure 3-2. Note, the Figure also contains the normalized current for the simple Nafion films. These values are plotted on the right, where the pore radius is effectively thought of as infinite.

Table 3: Values of $i_{comp}l/nFAc^{*}\varepsilon$ (10^{-6} cm^2/s): Extracted from the Intercepts of the Koutecky Levich Plots

$2r_0$ (nm)	Dop^+ HNO_3	H_2Q HNO_3	H_2Q H_2SO_4	$FerN^+$ HNO_3	RuN^{3+} HNO_3
15		6.37	5.44	1.47	2.77
30	5.85	14.70	13.33	1.78	5.86
50	2.94				
80		5.39	7.82		
100	0.487			1.23	1.89
600	0.703	1.21	0.58	0.51	0.71
Nafion Film	4.36	0.16	0.51	0.16	0.58

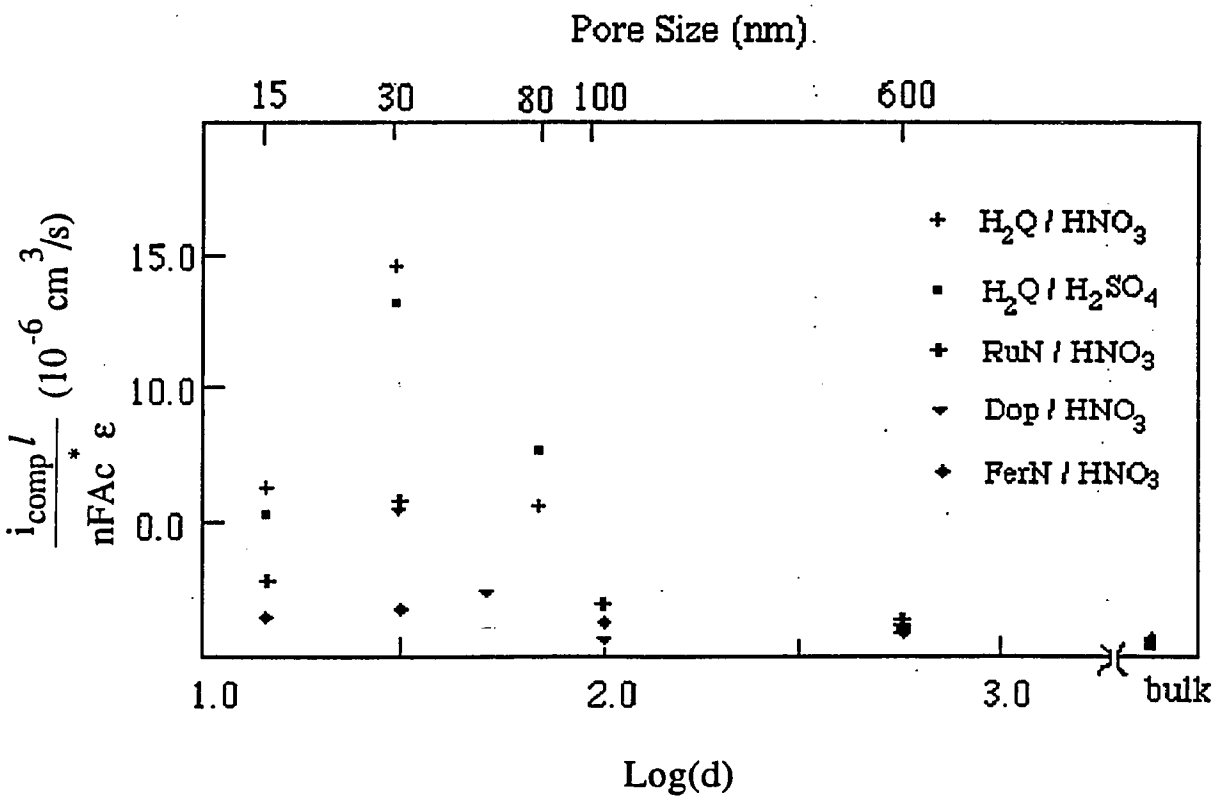

Figure 3-2: A plot of the intercepts of the Koutecky-Levich plots as a function of log(d). The intercepts are normalized as, $i_{comp}l/nFAc^{*}\varepsilon$ (10^{-6} cm^2/s), so all membranes can be compared on the same scale. For each composite, $i_{comp}l/nFAc^{*}\varepsilon$ is normalized for porosity; each point is proportional to the flux through the Nafion portion of the composite. For comparison, the results for Nafion films are also included at the points marked bulk.

From Figure 3-2, it is apparent that substantial flux enhancements are observed as the pore size decreases toward a diameter of 30 nm. At larger pore diameter, the transport characteristics are similar to those of a simple Nafion film. As the diameter shrinks toward 30 nm, the normalized current increases relative to that for the Nafion film. For hydroquinone in a 30 nm pore, the normalized current roughly twenty times higher than that of the Nafion film. For the 15 nm pore, the normalized current falls below the normalized current for the 30 nm pore.

3-4 PROPOSED MODEL

A phenomenalogical model is proposed to account for the observed enhancement of flux with decreasing pore radii. The model is based on a facile transport zone along the surface of the pore wall. The proposed model is illustrated in Figure 3-1. The zone within the pore is conceptualized in two parts: a Nafion-filled surface diffusion zone along the pore wall and a larger central region where the pore is filled with Nafion. Each portion of the pore is characterized by a transport rate and a partition coefficient. The wall zone is characterized by D_{wall} and κ_{wall}, the mass transport rate and partition coefficient for the wall zone, respectively. The central portion of the pore is similarly characterized by the transport and selectivity parameters for bulk Nafion, D_{Naf} and κ_{Naf}. Both diffusion coefficients are expressed in cm^2/s. The partition coefficients are ratios of the concentration of the redox species inside the pore to the bulk solution concentration before the onset of electrolysis; $\kappa_{wall} = c_{wall}/c^*$, and $\kappa_{Naf} = c_{pore}/c^*$. These can also be expressed under steady state electrolysis conditions as $\kappa_{wall} = c(r_o,l^-)/c(r_o,l^+)$, and $\kappa_{Naf} = c(r,l^-)/c(r,l^+)$. The wall zone is of thickness, δ, while the pore is of radius, r_o, or diameter, d. The pore is of length, l.

Mechanistically, redox material partitions into the Nafion portion of the composite because of electrostatic and organophillic interactions. The

concentration of redox species in the Nafion portion of the composite is likely to be high because partition coefficients for organic cations in Nafion are high. Values of 1000 and higher have been found [34]. However, transport rates in bulk Nafion are slow compared to transport in water. If molecules have higher transport rates along the surface of the pore walls than through the bulk of Nafion, the wall may serve as an "express lane" for the transport of molecules and ions to the electrode surface. Under these condition, the intercept of the Koutecky-Levich plot is composed of two additive components.

$$i_{comp} = i_{wall} + i_{bulk} \qquad [6]$$

where i_{wall} is transport along the wall and i_{bulk} is transport through the bulk Nafion in the pore. By analogy with the expression for i_{Naf}, i_{bulk} is written with a simple correction for the porosity. Assume the zone of transport near the pore wall is not large compared to r_o; that is, $\delta \ll r_o$. Then [16],

$$i_{bulk} = \frac{nFAD_{Naf}c^{*}\kappa_{Naf}\varepsilon}{l} \qquad [7]$$

where $A\varepsilon$ is the open cross sectional area of the pores in contact with the electrode of area, A. To relate the measured current to the gradient which created it, it is necessary to normalize the current to the cross sectional area through which the gradient is established. $A\varepsilon$ is the correct area term because the gradient being established at the electrode surface is through the cross section of area of the pores in contact with the electrode surface.

The gradient through the wall zone for a single pore is being established through a cross sectional area A_{wall}, where A_{wall} is the area of the wall zone for a single pore. See Figure 3-1b. The number of pores in contact with an electrode of area A is NxA. Thus, the total cross sectional area through which flux to the electrode surface is established through the wall zone is

AxN_xA_{wall} is units of square centimeters. Thus,

$$i_{wall} = \frac{nFA_xN_xA_{wall}D_{wall}c^{*}\kappa_{wall}}{l} \qquad [8]$$

A_{wall} is expressed as follows.

$$A_{wall} = \pi [r_o^2 - (r_o - \delta)^2] = \pi [2r_o\delta - \delta^2] \qquad [9]$$

For $\delta << r_o$, $A_{wall} \approx 2\pi r_o\delta$. Upon substituting this into Equation 8, and noting $\varepsilon = N\pi r_o^2$, Equation 6 can be expressed as

$$\frac{i_{comp}\, l}{nFAc^{*}\varepsilon} = \frac{2\delta\kappa_{wall}D_{wall}}{r_o} + \kappa_{Naf}D_{Naf} \qquad [10]$$

Thus, a plot of $i_{comp}l/(nFAc^{*}\varepsilon)$ versus r_o^{-1} should be a straight line. The intercept will describe transport through the Nafion in the center of the pore. The slop will be equal to $2\delta\kappa_{wall}D_{wall}$, which is the characteristic parameter for the surface diffusion process.

3.5 DISCUSSION

3.5-1 Discussion of the Qualitative Aspects of the Data

Some qualitative observations can be made based on the data presented in Figure 3-2 and Table 3. First, for large pores ($r_o \approx 300$ nm), the normalized flux is comparable to that of a simple Nafion film. As the pore size decreases toward a 30 nm diameter, the normalized flux increases. The flux enhancements are of the order of ten fold for the 30 nm pore relative to the simple film. Thus, the composite is able to support substantially higher flux through Nafion than the film. In fact, for hydroquinone, the normalized

flux through 30 nm pore relative to the simple composite is higher than in solution. The normalized flux in Table 3, units of cm^2/s, with the diffusion coefficients in solution is shown in Table 1. This enhancement is due to a combination of surface transport and increased concentration driven by partitioning. As the pore size diameter decreases to 15 nm, the normalized flux again decrease. Qualitatively, this suggests the surface area available for transport is adequate, but the amount of redox species the composite is able to provide is inadequate to sustain a large flux to the electrode surface. This will be discussed in greater detail below.

3.5-2 Quantitative Analysis of the Data By the Suggested Model Equation, Equation 10

The results presented in Figure 3-2 and Table 3 are to be analyzed quantitatively according to the model equation, Equation 10. Plots of $i_{comp}l/(nFAc^*\varepsilon)$ versus r_o^{-1} for each redox system are shown in Figure 3-3. Slopes, intercepts, and correlation coefficients found by linear regression are shown on the plot. These are summarized in Table 4. Note, the regression analysis was done excluding the 15 nm pore datum for each system. These points are included on the plot for comparison. An alternative expression of Equation 10 is to use the definition of A_{wall} expressed in Equation 9. This yields a second order equation in δ/r_o. Attempts to fit the data to this second order equation were unsuccessful. Values were found for δ of the order of 12 nm, larger than $r_o = 7.5$ nm for the smallest pores. The data for $r_o = 7.5$ nm are the least precise. However, to exclude these data leaves too few points to do a legitimate second order analysis.

Physically, one expects that as the pore radii grows large, the normalized flux should approach that of bulk Nafion. This expectation is born out by the proposed model, as summarized in Equation 10. Infinite pore radius corresponds to a simple Nafion film. Thus, a plot of the normalized flux versus r_o^{-1} will have an intercept of $\kappa_{Naf}D_{Naf}$.

Table 4: Results of Analysis According to Equation 9.

	Dop^+ HNO_3	H_2Q HNO_3	H_2Q H_2SO_4	$FerN^+$ HNO_3	RuN^{3+} HNO_3
Slope (10^{-12} cm^3/s) ($2\delta\kappa_{wall}D_{wall}$)	8.77	21.44	19.20	1.83	8.21
Intercept (10^{-6} cm^2/s) ($\kappa_{Naf}D_{Naf}$)	-0.348	0.311	1.16	0.63	0.36
Correlation Coefficient	0.956	0.9994	0.967	0.941	0.993
$\delta\ \kappa_{wall}D_{wall}$ (10^{-12} cm^3/s)	4.39	10.72	9.60	0.915	4.10
If $\delta \cong 1$ nm, then					
$\kappa_{wall}D_{wall}$ (10^{-6} cm^3/s)	40	100	100	9	40

Thus, the first test of the model is whether the experimentally determined intercepts correlate well with the values of $\kappa_{Naf}D_{Naf}$ found for simple Nafion films. As shown in Table 4, all the intercepts except dopamine are positive and of the order of 10^{-7} to 10^{-6} cm^2/s. This is consistent with the values of $\kappa_{Naf}D_{Naf}$ found for Nafion films based on Equation 5 and summarized in Table 3. This level of agreement between the value of $\kappa_{Naf}D_{Naf}$ found for the composites and that found for the simple Nafion films is acceptable. The analysis of the composite data to find $\kappa_{Naf}D_{Naf}$ involves several sequential analyses: first, take the intercept of the Koutecky-Levich plots for each pore size to find the normalized flux through the pores; second, plot the intercepts against the reciprocal pore radii; and, third, use the intercept of this plot to find $\kappa_{Naf}D_{Naf}$. The correlation coefficients for some of the plots reflect the propagation of errors associated with this multiplicity of steps. the analysis of the flux through the simple Nafion films is limited by the approximation of the film thickness from the density of wet Nafion and the amount pipeted onto the electrode surface. Given the propagation of errors in this analysis, the order of magnitude agreement between the values of $\kappa_{Naf}D_{Naf}$ is acceptable.

The dopamine data requires a few additional comments. The source of the slightly negative intercept for the dopamine is not known, but given the poor correlation coefficient for the plot, it is not unexpected. In addition, the value found for $\kappa_{Naf}D_{Naf}$ in the simple Nafion films is notably higher for dopamine than for the other redox species. Based on values of D_{Naf} of $1.5x10^{-9}$ cm^2/s [35] and a selectivity coefficient for dopamine over sodium ion of 5000 [34], $\kappa_{Naf}D_{Naf}$ for the bulk film can be approximated as $1x10^{-6}$ cm^2/s. This value is about half an order of magnitude smaller than the value found here. The difference may arise from inaccuracies in the calculated film thickness.

In general, however, the similarity of $\kappa_{Naf}D_{Naf}$ for Nafion in the composites and the films suggests the microstructure of Nafion in the pores is

similar to the structure of Nafion in cast films.

The physical picture of the model suggests the flux enhancement associated with the surface of the pores will depend on the surface area of the pores, which is $2\pi r_o N l$. As i_{comp} is normalized by ε, the surface area is expressed as $2\varepsilon l/r_o$. Thus, the flux is expected to increase with surface area, and the normalized flux will increase with r_o^{-1}. This expectation is met by each of the redox couples presented here for $d \geq 30$ nm. In each case, the normalized flux decreases as the pore size increases. Thus, based on Equation 10, the model predicts the normalized flux will fall linearly with r_o^{-1}, and the slope of $i_{comp} l$ /nFAc*ε versus r_o^{-1} will be $2\delta\kappa_{Naf}D_{Naf}$, which is characteristic of transport along the wall.

The slopes of the plots of $i_{comp} l$ /nFAc*ε versus r_o^{-1} shown in Figure 3-3 are summarized in Table 4. $\delta\kappa_{Naf}D_{Naf}$ ranges between 10^{-12} and 10^{-11} cm^3/s. The wall transport is most rapid for the neutral hydroquinone systems. dopamine, which is similar in size to hydroquinone but positively charged, exhibits a wall transport rate more similar to the smaller but more positively charged RuN^{+3}, than to its structurally analogous hydroquinone. $FerN^{+}$, the largest of the redox species at 0.8 nm, exhibits the slowest wall transport rate.

It would be of interest to evaluate the individual terms in $\delta\kappa_{Naf}D_{Naf}$, but a detailed evaluation is difficult. There are complexities in separating κ and D in bulk polymer matrices because of uncertainties in thickness and homogeneity. In the pores of the composites, the problems of evaluating κ_{Naf} and D_{Naf} are complicated by very small samples inside the pores and residual Nafion on the exterior of the composites. To attempt to separate $\delta\kappa_{Naf}$ and D_{Naf}, parameter characteristic of a smaller zone within the pore is even more complex. It should be possible to get a rough estimate of the product, $\delta\kappa_{Naf}D_{Naf}$, however, given an estimate of δ.

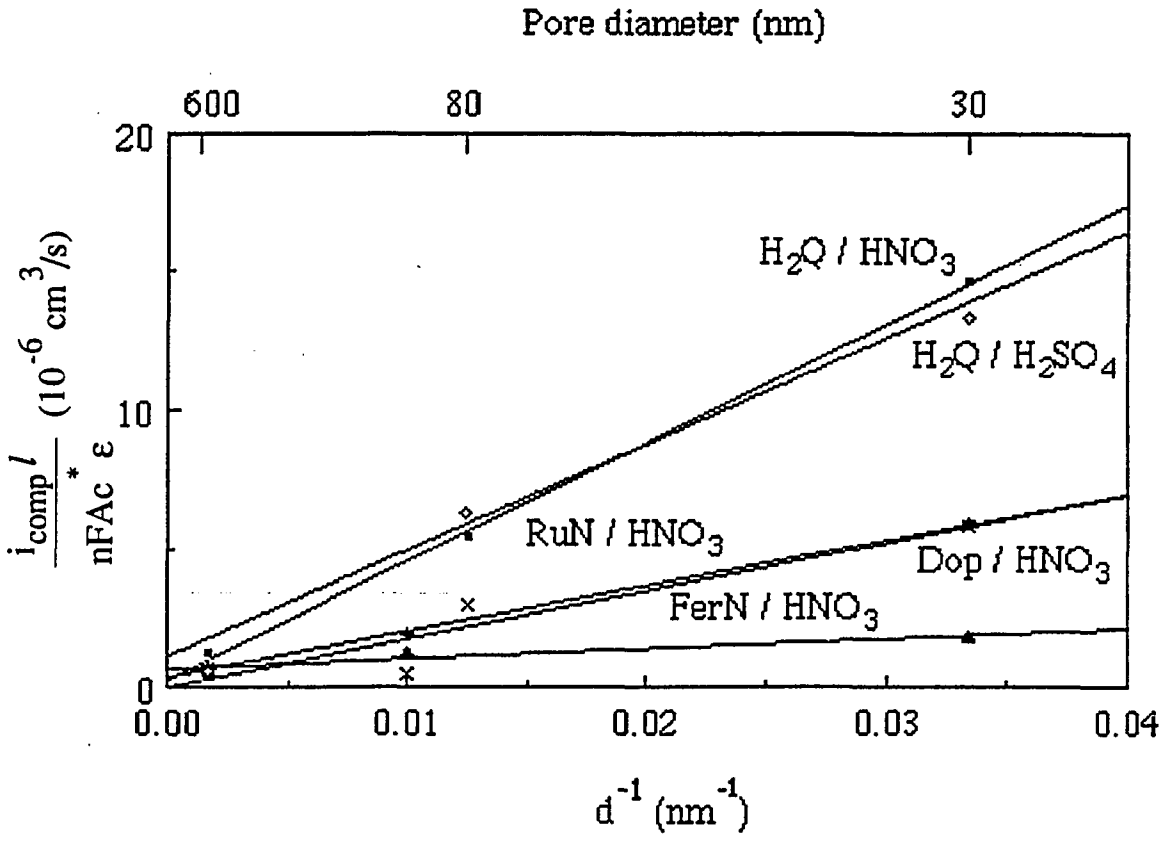

Figure 3-3: Plots of $i_{comp}l$ /nFAc*ε versus d^{-1}, as according to Equation 10. Lines are determined by linear regression for all d>30 nm. Points for 7.5 nm composites are also included on the plot for comparison. The statistical results for these plots are summarized in Table 4.

3-5.3 Estimation of the Thickness the Surface Diffusion Zone, δ

The value of δ can be approximated based on the following considerations. First, the zone for interfacial diffusion must be at least as large as the diffusing molecule. The redox species examined here range in size from 0.5 to 0.8 nm. Second, assume that δ is the same for all redox species. This sets a lower limit on δ of 0.5 nm. Third, in deriving Equation 10, the approximation was made in Equation 9 that $r_o << \delta$. The model holds for pore radii as small as 15 nm, as indicated by the linear regression lines in Figure 3-3. For the lines to have correlation coefficients of 0.999, as they do for hydroquinone in nitric acid and RuN^+, δ should be less than roughly 10 % of r_o; that is, $\delta \leq 1.5$ nm. These approximations bracket the thickness of the interfacial diffusion zone, such that $0.5 < \delta < 1.5$ nm. As discussed in more detail below, this range of values is also consistent with the physical picture of the surface zone.

By taking δ as 1 nm, values of $\kappa_{wall}D_{wall}$ were calculated and tabulated in Table 4. $\kappa_{wall}D_{wall}$ values are of the order 10^{-5} and 10^{-4} cm^2/s. Inherent in the development of the model was the assumptions that for transport along the wall to be an effective mode of transport, flux along the surface must be large compared to that through bulk Nafion. This assumption is consistent with these results. Upon comparing the values of $\kappa_{wall}D_{wall}$ in Table 4 with values $\kappa_{Naf}D_{Naf}$ found either for Nafion films (Table 3) or the composites (the intercepts in Table 4), $\kappa_{wall}D_{wall}$ is greater than $\kappa_{Naf}D_{Naf}$ by roughly two orders of magnitude.

It is interesting to note that $\kappa_{Naf}D_{Naf}$ denotes a flux which is roughly ten times higher than the flux of species in solution at millimolar concentrations; the solution flux is the represented by D_s, the diffusion coefficient in solution. It is unlikely that diffusion along the wall would be more facile than diffusion through solution. This sets an upper limit on D_{wall} of D_s. If D_{wall} is taken as D_s, κ_{wall} ranges between about 1.5 for $FerN^+$ and 10 for H_2Q. If

D_{wall} is smaller, κ_{wall} will higher. It is difficult to envision a system where κ_{wall} is substantially greater than κ_{Naf}. Physically, it is probable that the Nafion in the center of the pore concentrates the redox species, and the wall zone is fed by redox species from the center of the pore. Thus, as an upper limit, κ_{wall} can be approximated by κ_{Naf}. κ_{Naf} is known to be 5000 for dopamine. If κ_{wall} is the same as κ_{Naf}, then D_{wall} is 8 x 10^{-9} cm^2/s which represents a lower limit estimate for D_{wall}.

Comments on the nature of the interfacial zone are speculative. At a molecular level, δ of 1.5 nm is an interesting length. Previous work [16] has shown that the sulfonic acid sites of the Nafion are adsorbed at roughly monolayer coverage on the walls of the pores. The sulfonic acid sites are attached to the fluorocarbon backbone of the Nafion by pendant side chains which are 1.7 nm in length. If the arrangement of the pendant side chains is similar to that observed in a Langmuir Blodgett film, δ may characterize the interfacial zone created by an ordered, somewhat closely packed array of the surfactant like side chains. If that is the case, transport through this zone would resemble transport through assembled monolayers.

Anson and coworkers [31] had proposed a model at the molecular level to account for the higher partitioning of organic materials than inorganic ions into cast poly(lysine) film. They speculated that the transport channels in poly(lysine) represented unique transport zones with different degrees of hydrophobicity. Metal cations would be extracted into the water filled zone. On approaching the edge of the channel where there is hydrophobic and organophilic material, the water and ion content drops, as does the dielectric. This zone favors partitioning of organic redox species. If the relative fraction of highly ionic zones is small compared to the organophilic zones, then higher κ might be anticipated for organic redox species. Transport of metal cations would be through the water filled zones while the organic materials would move in the organophilic zones, which exist at the interface between the organic material and water filled regions. The model proposed

here is microstructural analog of Anson's molecular scale model. That is, on the scale of nanometers as opposed to the tenth of nanometer scales in the molecular model of Anson.

3-6 CONCLUSION

Thoughts about these interfacial zones and their associated surface gradients pose some interesting questions about how microstructured matrices can be designed to facilitate transport and selectivity. A first approximation about a microstructured matrix packed with a viscous polymer is that it would not be able to support the same flux as a standard electrochemical solution. These results show that the composite cannot only support the flux, but it can begin to exceed that in solution. In addition to sustaining the flux, the composites can be viewed as selective microstructural pipes. Molecular or microstructural reactors could be designed which would capitalize on this selectivity and transport.

Finally, the model proposed here, while accounting for the results, is a phenomenalogical model. It does not account for any possible extraction from the Nafion in the center of the pores into the wall zone. This can be an important effect in the design of molecularly engineered systems. In designing molecularly engineered systems, it will be important optimize the selectivity and transport. That is, there is an optimum ratio between pore surface area for facile transport and volume of Nafion driving the extraction. If the volume of Nafion is very large, the concentration of redox species is high, but it has too far to diffuse through the Nafion to reach the pore wall and the transport is not effective. If the pore is too small, transport is effective but the concentration of redox species is not high enough to sustain the flux. It is likely that the results for the 7.5 nm pores fall into this case: there is more surface area available for transport than there is Nafion available to extract redox material and sustain the flux to the pore wall.

Thus, while the model represented by Equation 10 provides a good phenomenalogical description of the composite system, it does not provide a mechanism for designing optimized ratios of surface area for transport and volume for extraction. We are currently working on a more sophisticated model which will allow us to parameterize the optimization.

APPENDIX A

The Constraints of Developing the Irregular Expanding Grid

Conditions	Grid Size Δz, Δr, $\Delta z=\Delta r$	Central Point of Grid z_j, r_i
$-\infty < z < \infty$		
$-\infty < j < \infty$	$\Delta z_j=\Delta z \exp[\beta(\|j\|-1)]$	$z_j=\Delta z \dfrac{\exp[\beta(\|j\|-0.5)]-1.0}{\exp[\beta]-1.0}$
$0 < r_i \le a$ [1]		
$0 < i \le N_{ra}$	$\Delta r_i=\Delta r$	$r_i=(i-0.5)\Delta r \quad (a=N_{ra}\Delta r)$
$a < r_i \le (b-a)/2$ [2]		
$N_{ra} < i \le M$ [2]	$\Delta r_i=\Delta r \exp[(\beta(i-N_{ra}-1)]$	$r_i= \Delta r \{\dfrac{\exp[\beta(i-N_{ra}-0.5)]-1.0}{\exp(\beta)-1.0}+N_{ra}\}$
$(b-a)/2 < r_i \le b$		
$M < i \le L$ [2]	$\Delta r_i=\Delta r \exp[(\beta(L-i)]$	$r_i= \sum_{i=1}^{L} \Delta r_i - \Delta r \dfrac{\exp[\beta(i-N_{ra}-0.5)]-1.0}{\exp(\beta)-1.0}$
$b < r_i < +\infty$		
$L < i < +\infty$	$\Delta r_i=\Delta r \exp[(\beta(i-L-i)]$	$r_i= \sum_{i=1}^{L} \Delta r_i + \Delta r \dfrac{\exp[\beta(i-L-0.5)]-1.0}{\exp(\beta)-1.0}$

[1]: $a=N_{ra}\Delta r$. Δr is the basic and first grid and N_{ra} is the grid number used in the disk electrode area.

[2]

$$b = a + 2\sum_{i=N_{ra}+1}^{M} \Delta r_i = \sum_{i=1}^{L} \Delta r_i$$

where L is the grid number for the shielding and electrode area, $L=2M-N_{ra}$. M is the grid number for the half shielding area and the electrode area. See schematic diagram below.

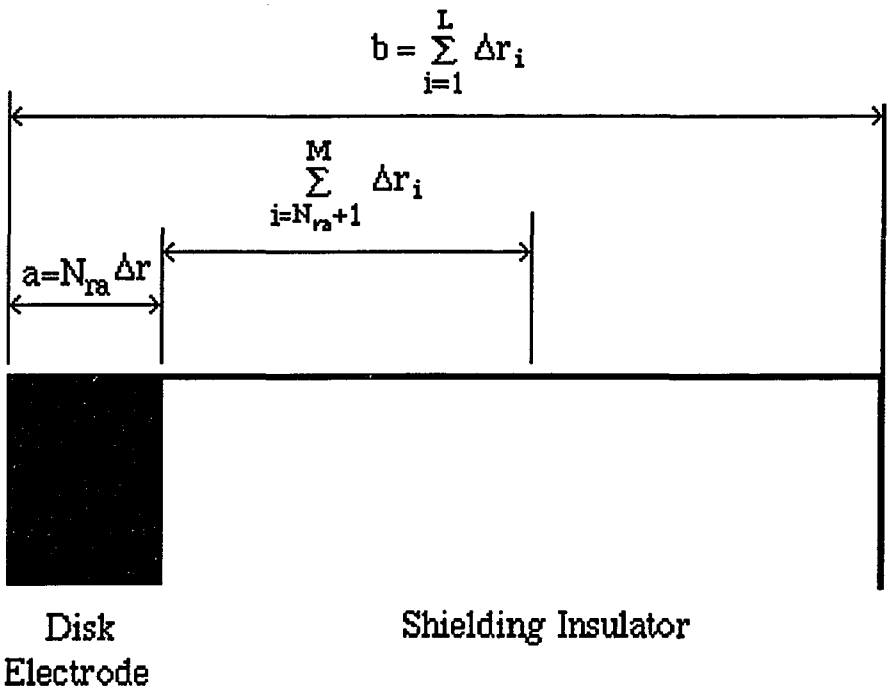

APPENDIX B

The Fortran Program Which Calculates the Cyclic Voltammograms For Semi-Infinite and Finite Shielding Disk Electrode

The following Fortran program, Disk.For, calculates the cyclic voltammetric parameters, including dimensionless peak current Z_p, dimensionless steady state current Z_{ss}, peak potential E_p, differential peak potential ΔE_p, differential potential at the half peak current $E_{1/2}$, concentration profile and current profile corresponding to the applied potential. The program runs on a Digital Corporation VAX 8000 computer using the Fortran compiler as well as the Fortran and system libraries. The inputs are prompted either using direct enter or data files. Output arrays are stored. The results are selected to be printed.

```
C     The name of this program is called SIMULATION1.FOR.
C     The program is used to calculate the CV for disc electrode
C     with semi-infinite shielding situation at EC reaction.*********
C     The reaction is a reversible electrochemical reaction coupled
C     with a first order irreversible chemical reaction
C
C     AO,AN,BO,BN ---The concentrations for species A and B, old and
                     new
C     AVEX or AVEY-- The distance from center of disc to grid center
C     BETA     -----  The expanding grid coefficient
C     CUR      -----  The dimensionless current.
C     DISX or DISY---- The distance from center of disk to grid edge
C     DELTX, DELTY--The length of grid
C     DJ       -----  The expanding grid diff. coeff. in Y direction
C     DM       -----  The uniform grid diff. coeff.
C     DN       -----  The expanding grid diff. coeff. in R direction
C     DR       -----  The expanding grid radial diff. coeff.
C     EFINAL   -----  The final scan potential
C     ESTART   -----  The start scan potential
C     EZERO    -----  The standard potential of the simulated reaction
C     FLUX     -----  The dimensionless concentration flux
C     FRT      -----  The multipled constant of F and RT
C     L        -----  The iteration number
C     NELE or N4 ----  The # of boxes for disk electrode radius
C     PI       -----  The PI constant
C     POTNOR   -----  The dimensionless potential
C     RKB      -----  The dimensionless backward hetero. rate constant
C     RKF      -----  The dimensionless forward heter. rate constant
C     RKS      -----  The dimensionless standard heter. rate constant

      implicit double precision (A-H)
      implicit double precision (O-Z)
      dimension AN(61,51), BN(61,51), AO(61,51), BO(61,51), DJ2(51),
     $DJ1(51), DN2(61), DN1(61), CUR(144001), DR(61), AVEX(61),
     $DELTX(61), DISX(61), AVEJ(51), DELTJ(51), FLUX(100),
     $POTNOR(144001)

      open(unit=6, status='new', carriagecontrol='list')

      read(5,*) RLAMDA, NELE, L, RT

C     The direct input form
```

```
C       Rlamda=1.0D05
C       nele=6
C       nn=20
C       l=720
C       RT=0.0d00

C       Set-up the basic data

        FRT=3.892039d+1
        PI=3.1415927d00
        BETA=0.3d00
        L2=2*L
        DM=0.16d00
        dma=dm
        dmb=dm
        ESTART=0.2d00
        EESTART=ESTART*FRT
        EFINAL=-0.25d00
        EEFINAL=EFINAL*FRT
        EZERO=0.0d00
        EEZERO=EZERO*FRT

        N4=NELE
        N5=N4+1

C       Calculate some constants

        BETA2=2.0d00*BETA
        BETA1=1.0d00/BETA
        BETA3=BETA/2.0d00
        ETERM=6.0d00*(dexp(BETA)-1.0d00)
        SC=(ESTART-EFINAL)/dfloat(L)
        ENM=(ESTART-EZERO)
        RKS=RLAMDA*dsqrt(DM/dfloat(L))

C       Write some input constants.

        write(6,730)
        write(6,732) L,L2
        write(6,734) DMA, DMB, BETA
        write(6,736) N4
        write(6,456)
```

```
      write(6,*) ESTART,EFINAL,EZERO
      write(6,457)
      write(6,*)RLAMDA
      write(6,458)
      write(6,459)RT

C     Initiation

      do 111 I=1,L2+1
      CUR(I)=0.0d00
      POTNOR(I)=0.0d00
111   continue

      do 1 J=1,51
      do 2 N=1,61
      AO(N,J)=1.0d00
      AN(N,J)=1.0d00
      BN(N,J)=0.0d00
      BO(N,J)=0.0d00
2     continue
1     continue

      do 586 N=1,100
      FLUX(N)=0.0d00
586   continue

      do 587 N=1,61
      DN1(N)=0.0d00
      DN2(N)=0.0d00
      DR(N)=0.0d00
      DISX(N)=0.0d00
      AVEX(N)=0.0d00
      DELTX(N)=0.0d00
587   continue

      do 588 N=1,51
      DJ2(N)=0.0d00
      DJ1(N)=0.0d00
      AVEJ(N)=0.0d00
      DELTJ(N)=0.0d00
588   continue

C     Calculation of expanding grid diff. coeff. in J direction
```

```
      do 201 J=1,3
      DELTJ(J)=1.0D00
      AVEJ(J)=DFLOAT(J)-0.5D00
201   continue

      do 14 J=4,51
      AVEJ(J)=3.0D00+(dexp(BETA*(dfloat(J-3)-0.5d00))-1.0d00)
     $/(dexp(BETA)-1.0d00)
      DELTJ(J)=dexp(BETA*(dfloat(J-4)))
14    continue

      do 15 J=2,50
      DJ1(J)=DM/DELTJ(J)/(AVEJ(J)-AVEJ(J-1))
      DJ2(J)=DM/DELTJ(J)/(AVEJ(J+1)-AVEJ(J))
15    continue

      DJ2(1)=DM/DELTJ(1)/(AVEJ(2)-AVEJ(1))

C     Calculation of expanding grid diff. coeff. in N direction

      do 12 N=1, N4+1
      AVEX(N)=dfloat(N)-0.5d00
      DELTX(N)=1.0D00
12    continue

      XX=dfloat(N4+1)

      do 155 N=2,61-N4
      AVEX(N+N4)=XX+(dexp(BETA*(dfloat(N-1)-0.5d00))-1.0d00)
     $/(dexp(BETA)-1.0d00)
      DELTX(N4+N)=dexp(BETA*(dfloat(N-2)))
155   continue

      do 23 N=2,60
      DN1(N)=DM/DELTX(N)/(AVEX(N)-AVEX(N-1))
      DN2(N)=DM/DELTX(N)/(AVEX(N+1)-AVEX(N))
      DR(N)=DM/AVEX(N)/(AVEX(N+1)-AVEX(N-1))
23    continue

C     SET-UP THE SPECIAL DIFFUSION COEFFICIENTS

      DJ1(1)=0.0d00
```

```
      DN1(1)=0.0d00
      DN2(1)=DM
      DR(1)=DM

C     Set-up some iteration constants

      NMAX=0
      IMAX=1
      IMIN=1
      JMAX=0

C     Start the iteration calculation

      DO 19 I=1,L2

C     Calculation of the number of box which will be pertubated by
      diffusion

      if(I.lt.L) then
      POTNOR(I)=ENM-dfloat(I)*SC
      else
      POTNOR(I)=ENM-dfloat((L2-I))*SC
      endif

93    JMAX=4.0+BETA1*dlog(ETERM*dsqrt(DM*I+1.0))

      NMAX=N4+JMAX

78    do 440 J=2,Jmax
      do 460 N=1,Nmax
      TEMP1=AO(N,J)
      TEMP2=BO(N,J)

      if(N.eq.1) then
      R1=DR(N)*(AO(N+1,J)-TEMP1)
      R2=DR(N)*(BO(N+1,J)-TEMP2)
      else
555   R1=DR(N)*(AO(N+1,J)-AO(N-1,J))
      R2=DR(N)*(BO(N+1,J)-BO(N-1,J))
      endif

556   AN(N,J)=TEMP1
      $+DJ2(J)*(AO(N,J+1)-TEMP1)
```

```
      $+DJ1(J)*(AO(N,J-1)-TEMP1)
      $+DN2(N)*(AO(N+1,J)-TEMP1)
      $+DN1(N)*(AO(N-1,J)-TEMP1)
      $+R1

      B=TEMP2
      $+DJ2(J)*(BO(N,J+1)-TEMP2)
      $+DJ1(J)*(BO(N,J-1)-TEMP2)
      $+DN2(N)*(BO(N+1,J)-TEMP2)
      $+DN1(N)*(BO(N-1,J)-TEMP2)
      $+R2
      BN(N,J)=B-B*RT/dfloat(L)
460   continue
440   continue

C     Calculation of the first layer box

      RKF=RKS*dexp(-0.5d00*FRT*POTNOR(I))
      RKB=RKS*dexp(0.5d00*FRT*POTNOR(I))

      Z=0.0d00

      do 477 N=1,NMAX
      TEMP1=AO(N,1)
      TEMP2=BO(N,1)

      FLUX(N)=(RKF*TEMP1-RKB*TEMP2)
      $/(1.0d00+(RKF/2.0D00/DM)
      $+(RKB/2.0D00/DM))

      if(N.lt.N5) then
34    if(N.eq.1) then
67    R5=DR(N)*(AO(N+1,1)-AO(N,1))
      R6=DR(N)*(BO(N+1,1)-BO(N,1))
      else
81    R5=DR(N)*(AO(N+1,1)-AO(N-1,1))
      R6=DR(N)*(BO(N+1,1)-BO(N-1,1))
      endif

82    AN(N,1)=TEMP1-FLUX(N)
      $+DJ2(1)*(AO(N,2)-TEMP1)
      $+DN2(N)*(AO(N+1,1)-TEMP1)
      $+DN1(N)*(AO(N-1,1)-TEMP1)
```

```
      $+R5
      B=TEMP2+FLUX(N)
      $+DJ2(1)*(BO(N,2)-TEMP2)
      $+DN2(N)*(BO(N+1,1)-TEMP2)
      $+DN1(N)*(BO(N-1,1)-TEMP2)
      $+R6
      BN(N,1)=B-B*RT/dfloat(L)

      else

73    AN(N,1)=TEMP1
      $+DJ2(1)*(AO(N,2)-TEMP1)
      $+DN2(N)*(AO(N+1,1)-TEMP1)
      $+DN1(N)*(AO(N-1,1)-TEMP1)
      $+DR(N)*(AO(N+1,1)-AO(N-1,1))

      B=TEMP2
      $+DJ2(1)*(BO(N,2)-TEMP2)
      $+DN2(N)*(BO(N+1,1)-TEMP2)
      $+DN1(N)*(BO(N-1,1)-TEMP2)
      $+DR(N)*(BO(N+1,1)-BO(N-1,1))
      BN(N,1)=B-B*RT/dfloat(L)

      endif

477   continue

C     Calculation of fluxes across the electrode area

      do 497 N=1,N4-1
      Z=Z+2.7D01*(2.0D00*dfloat(N)-1.0D00)*FLUX(N)
497   continue

      Z=Z+FLUX(N4)*(4.2D01*dfloat(N4)-2.1D01)
      $+(6.0D00*dfloat(N4)-1.0D00)*FLUX(N4+1)
      $+FLUX(N4-1)*(6.0D00*dfloat(N4)-5.0D00)

      CUR(I)=Z*PI/1.08D02/dfloat(N4)/DM

C     Reinitialization of concentrations

343   do 330 J=1,JMAX
      do 340 N=1, Nmax
```

```
      AO(N,J)=AN(N,J)
      BO(N,J)=BN(N,J)
340   continue
330   continue

C     Find out the peak currents and peak potentials

118   if(I.gt.100.and.I.lt.L.and.CUR(I).gt.CUR(IMAX))IMAX=I
      if(I.gt.L.and.CUR(I).lt.CUR(IMIN)) IMIN=I

19    continue

C     Search the back- and for-ward scan curves potential separation

      MIN=L*3/8
      MAX=L*5/8
      SEARCH2=1000.D00
      SEARCH3=1000.D00
      AVECUR=(CUR(IMAX)+CUR(1))/2.0D00
      do 36 I=MIN,MAX
      SEARCH=dabs(AVECUR-CUR(I))
      SEARCH1=dabs(AVECUR-CUR(I+L))
      if(SEARCH.gt.SEARCH2) goto 38
      SEARCH2=SEARCH
      MMIN=I
38    if(SEARCH1.gt.SEARCH3) goto 36
      SEARCH3=SEARCH1
      MMAX=I+L
36    continue

      EDELT=-(dfloat(MMIN)-(dfloat(2*L-MMAX)))*(4.5D02/dfloat(L))

      DELPOT=(POTNOR(IMIN)-POTNOR(IMAX))*1.0D03

C     Write some calculated resultes

      write(6,11)
      POMAX=POTNOR(IMAX)
      POMIN=POTNOR(IMIN)
      CMAX=CUR(IMAX)
      CMIN=CUR(IMIN)
      write(6,41)
      write(6,*)CMAX,CMIN
```

```
      write(6,22)CUR(L),CUR(L2)
      write(6,43)
      write(6,*)POMAX,POMIN, DELPOT
      write(6,448)EDELT
      write(6,900)N4

C     Type out the relationship between potential and current for selected
      points.

      write(6,45)
      if(l-1000) 87,88,89
87    NUM=10
      goto 331
88    NUM=20
      goto 331
89    if(l-3000) 366,366,377
366   NUM=40
      goto 331
377   if(l-20000) 388, 388, 399
388   NUM=100
      goto 331
399   if(l-100000)856, 557, 558
856   NUM=500
      goto 331
557   NUM=1000
      goto 331
558   NUM=2000

331   do 333 K=1, L2, NUM
      write(6,444)K,POTNOR(K),CUR(K)
333   continue

11    format(/,'PLEASE PAY ATTENTION FOR FOLLOWING DATA')
22    format(/,'CURRENT AT L AND L2=',D20.15,D20.15)
41    format(/,6X,'MAXIUM CURRENT',10X,'MINIMUN CURRENT')
441   format(/,6X,'MAXIUM CURRENT1',10X,'MINIUM CURRENT1')
42    format(/,6X,D20.15,6X,D20.15)
43    format(/,6X,'LARGEST POTEN',10X,'SMALLEST POTEN',
      $10X,'DELTA POTEN(mV)')
443   format(/,6x,'LARGEST POTEN1',10X,'SMALLEST POTEN1',
      $10X,'DELTA POTEN1(mV)')
44    format(4X,D20.15,6X,D20.15,6X,D20.15)
45    format(/,1X,'ITERATION #',8X,'POTEN',17X,'CUR:RADIU',17X,
```

```
      $'CUR:COTT')
46    format(6X,I8,8X,D20.15,12X,D20.15)
47    format(/,6X,'SCAN RATE=',D20.15)
444   format(2X,I9,5X,E15.6,8X,E15.6)
448   format(/,6x,'THE SEPARATED CURVE POTENTIAL
      $(mV)=',D20.10)
449   format(/,6x,'THE SEPARATED CURVE POTENTIAL1
      $(mV)=',D20.10)
456   $format(/,9X,'START POTEN. FINAL POTEN. ZERO POTEN.')
457   format(/,8X,'DIMENSIONLESS KINETIC PARAMETER')
458   format(/,8X,'THIS IS THE SEMI-INFINITE DISC ELECTRODE
      $RESULT')
459   format(/,8X,'THE DIMENSIONLESS CHEM. REAC. RATE.
      $=',D20.10)
730   format(/,' MICROELECTRODE ARRARY SIMULATION')
732   format(//,' ITERATION NUMBER=',I8,6X,I8)
734   format(//,' DMA=',D20.10,3X,'DMB=',D20.10,
      $3X,'BETA=',D20.10)
736   format(//,' RADIUS DIVIDED BOX NUMBER=',I5)
738   format(//,' ES=',D10.6,6X,'EF=',D10.6,6X,'EO=',D10.6)
900   format(/,6X,'BOX # OF ELECTRODE=',I10)
1990  format(//,' THIS IS THE CONCENTRATION PROFILE DATA')
1996  format(6X,D15.10,6x,D15.10,6X,D15.10)
      close(unit=6)
      stop
      end
```

Reference

Introduction

1. M. Fleischmann, S. Pons, D.R. Rolison, and P.P. Schmidt (Eds.), Ultramicroelectrode, Datatech Systems, Morgantown, N.C., 1987.

2. A.M. Bond, M. Fleischmann, and J. Robinson, *J. Electroanal. Chem.*, **180** (1984) 257-263.

3. J.C. Jernigan, C.E.D. Chidsey, and R.W. Murray, *J. Am. Chem. Soc.*, **107** (1985) 2824-2826.

4. L. Geng, R.A. Redd, M.-H. Kim, T.T. Wooster, B.N. Oliver, J.Egekeze, R.T. Kennedy, J.W. Jorgenson, J.F. Parcher, and R.W. Murray, *J. Am. Chem. Soc.*, **111** (1989) 1614-1619.

5. J.F. Parcher, C.J. Barbour, and R.W. Murray, *Anal. Chem.*, **61** (1989) 584-589.

6. R.L. Cook, R.C. MacDuff, and A.F. Sammells, *J. Electrochem. Soc.*, **135** (1990) 1470-1471.

7. R.L. Cook, R.C. MacDuff, and A.F. Sammells, *J. Electrochem. Soc.*, **137** (1990) 187-189.

8. A.J. Appleby and F.R. Foulkes, Fuel Cell Handbook, Van Nostrand Reinbold, New York, 1989, p. 284-296.

9. J. Leddy and N.E. Vanderborgh in J.W. Van Zee and R.E. White (Eds.), *Proceedings of the Symposium on Diaphragms, Separators, and Ion Exchange Membranes*, Electrochemical Society, Pennington, N. J., 1986, p. 15-27.

10. J. Leddy, A.E. Iverson and N.E. Vanderborgh, in J.R. Selman and H.C. Maru (Eds.), *Symposium on Electrochemical and Thermal Modeling of Battery, Fuel Cell and Photoenergy Conversion Systems*, Electrochemical Society, Pennington, N. J., 1986, p. 310-322.

11. J. Ghoroghchian, F. Sarfarazi, T. Dibble, J. Gassidy, J.J. Smith, A. Russell, G. Dunmore, M. Fleischmann and S. Pons, *Anal. Chem.*, **58**

(1986) 2278-2282.

12. R. Brina, S. Pons, and M. Fleischmann, *J. Electroanal. Chem.*, **24** (1988) 81-90.

13. R. Brina and S. Pons, *J. Electroanal. Chem.*, **264** (1989) 121-130; **296** (1990) 299-315.

14. S.W. Feldberg, *J. Electroanal. Chem.*, 222 (1987) 101-106; **290** (1990) 81-90.

15. C.D. Baer, M.J. Stone and D.A. Sweigart, *Anal. Chem.*, **60** (1988) 188.

16 A.M. Bond, D. Luscombe, K.B. Oldham and C.G. Zoski, *J. Electroanal. Chem.*, **249** (1988) 1-14.

17. D.R. Rolison in M. Fleischmann, S. Pons, D.R. Rolison and P.P. Schmidt (Eds.), Ultramicroelectrode, Datatech Systems Publishers, Morganton, N. C., 1987, p. 65.

18. R.M. Wightman and D.O. Wipf in A.J. Bard (Ed.). Electroanalytical Chemistry, Vol. **15**, P267-354, Marcel Dekker, 1989.

19. K. Potje-Kamloth, J. Janata, and M. Jofowicz, *Ber. Bunsen-Ges. J. Phys. Chem.*, **93** (1989) 1480-1485.

20. K.B. Oldham and C.G. Zoski, *J. Electroanal. Chem.*, **256** (1988) 11-
21,

K.B. Oldham, *J. Electroanal. Chem.*, **297** (1991) 317-348.

22. J.C. Myland and K.B. Oldham, *J. Electroanal. Chem.*, **288** (1990) 1-14.

23. C.A. Amatore, M.R. Deakin and R.M. Wightman, *J. Electroanal. Chem.*, **200** (1988) 23-35.

24. C.A. Amatore, B. Fosset, M.R. Deakin and R.M. Wightmam, *J. Electroanal. Chem.*, **225** (1987) 33-48.

25 A.J. Bard and L.R. Faulkner, Electrochemical Methods, Ch. 5, 6, and 11, Wiley, 1980.

26. S.W. Feldberg, *J. Electroanal. Chem.*, **296** (1990) 299-310.

27. J.S. Krueger, J.E. Mayl, and T.E. Mallouk, *J. Am. Chem. Soc.*, **110** (1988) 8232-4 .

28. L. Persaud, A.J. Bard, A. Campion, M.A. Fox, T. E. Mallouk, S.W. Webber, and J.M. White, *Inorg. Chem.*, **26** (1987) 3825-7.

29. Z. Li and T.E. Mallouk, *J. Phys. Chem.*, **91** (1987) 643-8; L. Persaud, A.J. Bard, A. Campion, M.A. Fox, T.E. Mallouk, S.W. Webber, and J.M. White, *J. Am. Chem. Soc.*, **109** (1987) 7309-18.

30. C.F. Shu and M.S. Wrighton, *J. Phys. Chem.*, **92** (1988) 5221-9.

31. P. Baeuerle, M.S. Wrighton, O.M.R. Chyan, and C.W. Spangler, *Ber. Bunsen Ges. Phys. Chem.*, **91** (1987) 889.

32. P.J. Kulesza and L.R. Faulkner, *J. Am. Chem. Soc.*, **110** (1988) 4905-13.

33. P.J. Kulesza and L.R. Faulkner, *J. Electroanal. Chem.*, **248** (1988) 305-320.

34. J. Leddy and N.E. Vanderborgh, *J. Electroanal. Chem.*, **235** (1987) 299-315.

Chapter I

1. J. Ghoroghchian, F. Sarfarazi, T. Dibble, J. Cassidy, J.J. Smith, A. Russell, G. Dunmore, M. Fleischmann, and S. Pons, *Anal. Chem.*, **58** (1986) 2278-2282.

2. R. Brina, S. Pons, and M. Fleischmann, *J. Electroanal. Chem.*, **244** (1988) 81-90.

3. R. Brina and S. Pons, *J. Electroanal. Chem.*, **264** (1989) 121-130.

4. J.C. Jernigan, C.E.D. Chidsey, and R.W. Murray, *J. Am. Chem. Soc.*, **107** (1985) 2824-2826.

5. L. Geng, R.A. Redd, M.-H. Kim, T.T. Wooster, B N. Oliver, J. Egekeze, R.T. Kennedy, J.W. Jorgenson, J.F. Parcher, and R.W. Murray, *J. Am. Chem. Soc.*, **111** (1989) 1614-1619.

6. J.F. Parcher, C.J. Barbour, and R.W. Murray, *Anal. Chem.*, **61** (1989) 584-589.

7. R.L. Cook, R.C. MacDuff, and A.F. Sammells, *J. Electrochem. Soc.*, **135** (1988) 1470-1471.

8. R.L. Cook, R.C. MacDuff, and A.F. Sammells, *J. Electrochem. Soc.*, **137** (1990) 187-189.

9. A.J. Appleby and F.R. Foulkes, Fuel Cell Handbook, Van Nostrand Reinhold, New York, 1989, p. 284-296.

10. J. Leddy and N.E. Vanderborgh in J.W. Van Zee and R.E. White (Eds.), *Proceedings of the Symposium on Diaphragms, Separators, and Ion Exchange Membranes*, Electrochemical Society, Pennington, N. J., 1986, p.15-27.

11. J. Leddy, A.E. Iverson, N.E. Vanderborgh, in J.R. Selman and H.C. Maru (Eds.), *Symposium on Electrochemical and Thermal Modeling of Battery, Fuel Cell and Photoenergy Conversion Systems*, Electrochemical Society, Pennington, N. J., 1986, p. 310-322.

12. H-J. Huang, P. He, and L.R. Faulkner, *Anal. Chem.*, **58** (1986) 2889-2891.

13. T.D. Gierke and W.Y. Hsu in A. Eisenberg and H.L. Yeager (Eds.), Perfluorinated Ionomer Membranes, American Chemical Society, Series Number 180, Chapter **13**, ACS, Washington, D.C., 1982, p. 299-306.

14. CRC Handbook of Chemistry and Physics, 64th Edition, (1984) p-46.

15. E.F. Caldin and G. Long, *J. Chem. Soc.* (1954) 3737.

16. L.S. Guss and I.M. Kolthoff, *J. Am. Chem. Soc.* **62** (1940) 1494.

17. H. Goldschmidt, Z. *Physik. Chem.* **89** (1914) 129.

18. I.M. Kolthoff and S. Ikeda, *J. Phys. Chem.* **65** (1961) 1020.

19. I.M. Kolthoff and M.K, Chantooni, Jr., *J. Am. Chem. Soc.* **90** (1968)

3320.

20. J.A. Dean, Lange's Handbook of Chemistry 11th. Edition, (1973) 6-32 6-33.

21. I.M. Kolthoff and T.B. Reddy, *Inorg. Chem.* **1** (1962) 189.

22. J. March, Advanced Organic Chemistry, Second Edition, McGraw-Hill Book Company, New York, 1977, p. 227-229.

23. A.J. Bard and L.R.Faulkner, Electrochemical Methods, John Wiley and Sons, New York, 1980, p. 488-511.

24. R. Parsons in P. Delahay and C.W. Tobias (Eds.), Advances in Electrochemistry and Electrochemical Engineering, Volume **1**, Interscience, New York, 1961, p. 1-64.

25. L.R. Faulkner in T. Kuwana (Ed.) Physical Methods of Modern Chemical Analysis, Volume **3**, Academic Press, 1983, p. 137-168.

26. L.D. Goodhue and R.M. Hixon, *J. Am. Chem. Soc.* **56** (1934) 1329.

27. A.J. Bard and L.R. Faulkner, Electrochemical Methods, John Wiley and Sons, New York, 1980, p. 540-542.

28. R.A. Malmsten, C.P. Smith and H. S. White, *J. Electroanal. Chem.*, **215** (1986) 223-235.

29. K.B. Oldham in M. Fleischmann, S. Pons, D.R. Rolison, and P.P. Schmidt (Eds.), Ultramicroelectrode, Datatech System Morgantown, N.C., 1987, p.276-287.

Chapter II

1. T. Dibble, S. Bandyopadhyay, J. Ghoroghchian, J.J. Smith, F. Sarfarazi, M. Fleischmann, and S. Pons, *J. Phys. Chem.* **90** (1986) 5275-5277.

2. J. Cassidy, S.B. Khoo, S. Pons, and M. Fleischmann, *J. Phys. Chem.* **89** (1985) 3933-3935.

3. A.M. Bond and P.A. Lay, *J. Electroanal. Chem.* **199** (1986) 285-295.

4. A.M. Bond, M. Fleischmann, and J. Robinson, *J. Electroanal.Chem.* **168** (1984) 299-312.

5. J.O. Howell and R.M. Wightman, *Anal. Chem.* **56** (1984) 524-529.

6. A.M. Bond, M. Fleischmann, and J. Robinson, *J. Electroanal. Chem.* **180** (1984) 257-263.

7. J. Ghoroghchian, F. Sarfarazi, T. Dibble, J.Cassidy, J.J. Smith, A. Russell, G. Dunmore, M. Fleischmann, and S. Pons, *Anal. Chem.*, **58** (1986) 2278-2282.

8. R. Brina, S. Pons, and M. Fleischmann, *J. Electroanal. Chem.*, **244** (1988) 81-90.

9. R. Brina and S. Pons, *J. Electroanal. Chem.*, **264** (1989) 121-130.

10. J.C. Jernigan, C.E.D. Chidsey, and R.W. Murray, *J. Am. Chem. Soc.*, **107** (1985) 2824-2826.

11. L. Geng, R.A. Redd, M.-H. Kim, T.T. Wooster, B.N. Oliver, J. Egekeze, R.T. Kennedy, J.W. Jorgenson, J.F. Parcher, and R.W. Murray, *J. Am. Chem. Soc.*, **111** (1989) 1614-1619.

12. J.F. Parcher, C.J. Barbour, and R.W. Murray, *Anal. Chem.*, **61** (1989) 584-589.

13. K.B. Oldham and C.G. Zoski, *J. Electroanal. Chem.*, **256** (1988) 11-19.

14. A.J. Bard and L.R. Faulkner, Electrochemical Methods, Ch. 5, 6, and 11, Wiley, 1980.

15. L. Meites, Polarographic Technique, Interscience, N.Y. (1955) p. 51-55

16. R.M. Penner, M.J. Heben, T.L. Longin, and N.S. Lewis, *Science*, **250** 1118-1121 (1990).

17. K. Potje-Kamloth, J. Janata, and M. Jofowicz, *Ber. Bunsen-Ges. J. Phys. Chem.*, **93** (1989) 1480-1485.

18. S.W. Feldberg, *J. Electroanal. Chem.*, **127** (1981) 1-10.

19. A.M. Bond, D. Luscombe, K.B. Oldham and C.G. Zoski, *J. Electroanal. Chem.*, **249** (1988) 1-14.

20. S.W. Feldberg, *J. Electroanal. Chem.*, **222** (1987) 101-106.

21. S.W. Feldberg, *J. Electroanal. Chem.*, **290** (1990) 49-65.

22. S. A. Lerke, D. H. Evans, and S.W. Feldberg, *J. Electroanal. Chem.*, **296** (1990) 299-315.

23. R.S. Nicholson and I. Shain, *Anal. Chem.*, **36** (1964) 706.

24. K.B. Oldham, *J. Electroanal. Chem.*, **297** (1991) 317-348.

25. J.C. Myland and K.B. Oldham, *J. Electroanal. Chem.*, **288** (1990) 1-14.

26. R.N. Adams, Electrochemistry at Solid Electrodes, Marcel Dekker, N.Y. 1969, p219-222.

27. C.A. Amatore, M. R. Deakin and R.M. Wightman, *J. Electroanal. Chem.*, **200** (1988) 2226.

Chapter III

1. J.S. Krueger, J.E. Mayl, and T.E. Mallouk, *J. Am. Chem. Soc.*, **110** 8232-4 (1988).

2. L. Persaud, A.J. Bard, A. Campion, M.A. Fox, T.E. Mallouk, S.W. Webber, and J. M. White, *Inorg. Chem.*, **26** (1987) 3825-7.

3. Z. Li and T.E. Mallouk, *J. Phys. Chem.*, **91** (1987) 643-8.

4. L Persaud, A.J. Bard, A. Campion, M.A. Fox, T.E. Mallouk, S.W. Webber, and J.M. White, *J. Am. Chem. Soc.*, **109** (1987) 7309-18.

5. C.F. Shu and M.S. Wrighton, *J. Phys. Chem.*, **92** (1988) 5221-9.

6. P. Baeuerle, M.S. Wrighton, O. M.R. Chyan, and C.W. Spangler, *Ber. Bunsen Ges. Phys. Chem.*, **91** (1987) 889.

7. D. Belanger and M.S. Wrighton, *Anal. Chem.*, **59** (1987) 1426-32.

8. S. Chao and M.S. Wrighton, *J. Am. Chem. Soc.*, **109** (1987) 2197-9.

9. E.T.T. Jones, O.M. Chyan and M.S. Wrighton, *J. Am. Chem. Soc.*, **109** (1987) 5526-8.

10. M.S. Wrighton, J.W. Thackery, M.J. Nata, D.K. Smith, G.A. Lane, and D. Belanger, *Philos. Trans. R. Soc.* London B **316** (1987) 13-30.

11. S. Chao and M.S. Wrighton, *J. Am. Chem. Soc.*, **109** (1987) 6627-31.

12. P.J. Kulesza and L.R. Faulkner, *J. Am. Chem. Soc.*, **110** (1988) 4905-13.

13. P.J. Kulesza and L.R. Faulkner, *J. Electroanal. Chem.*, **248** (1988) 305-320.

14. R.B. Morris, D.J. Franta, and H.S. White, *J. Phys. Chem.*, **91** (1987) 3559-64.

15. R.M. Penner, M.J. Heben, T.L. Longin, and N.S. Lewis, *Science* **250** (1990) 1118-1121.

16. J. Leddy and N.E. Vanderborgh, *J. Electroanal. Chem.*, **235** (1987) 299-315.

17. C.P. Andrieux, J.M. Dumas-Bouchiat and J.M. Saveant, *J. Electroanal. Chem.*, **131** (1982) 1.

18. C.P. Andrieux and J.M. Saveant, *J. Electroanal. Chem.*, **134** (1982) 163-166.

19. C.P. Andrieux and J.M. Saveant, *J. Electroanal. Chem.*, **142** (1982) 1

20. C.P. Andrieux, J.M. Dumas-Bouchiat and J. M. Saveant, *J. Electroanal. Chem.*, **169** (1984) 9.

21. C.P. Andrieux and J.M. Saveant, *J. Electroanal. Chem.*, **171** (1984) 65.

22. F.C. Anson, J.M. Saveant, and K. Shigehara, *J. Phys. Chem.*, **87** (1983) 214.

23. D.A. Gough and J.K. Leypoldt, *Anal. Chem.*, **51** (1979) 439.

24. D.A. Gough and J.K. Leypoldt, *Anal. Chem.*, **52** (1980) 1126.

25. D.A. Gough and J. K. Leypoldt, *A.I. ChE. J.* **26** (1980) 103.

26. D.A. Gough and J.K. Leypoldt, *J. Electrochem. Soc.*, **127** (1980) 1278.

27. J. Leddy, A.J. Bard, J.T. Maloy, and J.M. Saveant, *J. Electroanal. Chem.*, **187** (1985) 205-227.

28. J. Leddy and A.J. Bard, *J. Electroanal. Chem.*, **153** (1983) 223.

29. A.E. Ewing, B.J. Feldman, R.W. Murray, *J. Phys. Chem.*, **89**(1985) 1263.

30. T. Ikeda, R. Schmehl, P. Denisovich, K. Willman, and R.W. Murray, *J. Am. Chem. Soc.*, **104** (1982) 2683.

31. F.C. Anson, T. Oshaka, and J.M. Saveant, *J. Phys. Chem.*, **87** (1983) 640.

32. W.Y. Hsu and T.D. Gierke, J. Memb. *Science*, **13** (1983) 307.

33. K.A. Mauritz, C.J. Hora, and A.J. Hopfinger, Polym. Prepr. Am. Chem. Soc. Div. Polym. Chem. **19** (1978) 324.

34 G. Nagy, G. Gerhardt, A.F. Okee, M.E. Rice, R.N. Adams, R.B. Moore III, M.N. Szentirmay, and C.R. Martin, *J. Electroanal. Chem.*, **188** (1985) 85-94.

35 Eric W. Kristensen, Werner G. Kuhr, and R.M. Wightman, *Anal. Chem.*, **59** (1987) 1752-1757.

Glossary

A	Area of electrode (cm^2)
AA(j,i,k)	Dimensionless concentration of species A at space coordinators, j and i, and time coordinator, k
a	Radius of disk (cm)
B	Redox species in simulation
b	Radius of shielding plus disk (cm)
C	Capacitance (F)
c	Concentration (mol/cm^3)
$c_{\pm}(x_2)$	concentration of either the anions or the cations at x_2 in chapter I (mol/cm^3)
$c_A(z,r,t)$	concentration of specie A at space z and t, and time t
c^*	Total concentration of cations or anions in bulk solvent (mol/cm^3)
c_A^o	Bulk concentration of species A (mol/cm^3)
c_b	Bulk concentration of pure redox solutions (mol/cm^3)
c_{pore}	Concentration of redox species in membrane pore (mol/cm^3)
c_{wall}	Concentration of redox species in the interface between the membrane and Nafion (mol/cm^3)
$c(r_o,l^-)$	Concentration of species at the space of the pore wall and inside outer edge of the composite under steady state electrolysis (mol/cm^3)
$c(r_o,l^+)$	Concentration of species at the space of the pore wall and outside the outer edge of the composite under steady state electrolysis (mol/cm^3)
D	Diffusion coefficient (cm^2/s)
DM	Dimensionless diffusion coefficient, $D\Delta t/\Delta x^2$
DR1(i)	Dimensionless diffusion coefficient at inside radial

	coordinate, i
DR2(i)	Dimensionless diffusion coefficient at outside radial coordinate, i
DR3(i)	Dimensionless diffusion coefficient at middle radial coordinate, i
DZ1(j)	Dimensionless diffusion coefficient at inside perpendicular coordinate, j
DZ2(j)	Dimensionless diffusion coefficient at outside perpendicular coordinate, j
D_{Naf}	Diffusion coefficient of redox species in Nafion (cm^2/s)
D_{wall}	Diffusion coefficient of redox species in Nafion at the pore wall in the composite (cm^2/s)
E(t)	Time dependent applied potential (V)
E_f	Switching potential in cyclic voltammetry (V)
E_o	Initial potential in cyclic voltammetry (V)
$E^{o'}$	Formal potential of an electrode (V)
$\Delta E_{1/2}$	difference in potential observed on the forward and reverse branches of a cyclic voltammogram when the current is half the steady state current (V)
e	electronic charge (esu)
EESG	Exponentially expanding spatial grid in simulation
F	Faraday constant
GCS	Gouy-Chapman-Stern theory
i	Current (A)
	Dimensionless radial coordinate in simulation (Chapter II)
i(t)	Time dependent current (A)
i_{inlaid}^{ss}	Steady state current of the inlaid disk electrode (A)
i_{hemi}^{ss}	Steady state current of the hemisphere electrode (A)
i_{lim}	Steady state current for rotating disk voltammetry (A)
i_p	Peak current at voltammetric response (A)

i_{ss}	Steady state current at a microelectrode (A)
j	Dimensionless perpendicular coordinate in simulation
J_{bulk}	Flux of species through the bulk Nafion (mol cm^{-2} s^{-1})
J_{wall}	Flux of species along the wall of the composite (mol cm^{-2} s^{-1})
K	Absolute temperature (K)
k	Boltzmann's constant (J/K)
	Time counter in simulation (Chapter II)
	Dimensionless time coordinate in simulation (Chapter II)
K_{auto}	Autoprotolysis constant
K_a, K_b	Disassociation constants for organic solutes in water
$K_{a,HS}$, $K_{b,HS}$	Acidity and basicity constants for water in the organic solvents
k_m^o	Measured standard heterogeneous rate constant (cm/s)
k^o	Standard heterogeneous rate constant (cm/s)
k_{max}	Maximum number of time steps
l	Distance between working and aux-ref electrode (cm)
	Pore length of the membrane (cm)
n	Number of electrode transferred
N	Pore density of membrane (pores/cm^2)
N_A	Avogadro's number
N_{ra}	Number of grid elements across the disk radius
N_{rb}	Number of grid elements across total electrode radius.
R	Gas constant (J $mol^{-1}K^{-1}$)
r	Radial coordinate in simulation
r_o	Radius of hemisphere electrode (cm) (Chapter II)
	Radius of pore in membrane (cm) (Chapter II)
SEM	Scanning electron microscopy
T	Absolute temperature (K)
T_t	Total time (s) $T_t=(aD\Delta E/v)$

t	Time (s)
$V(k)$	Dimensionless potential at time counter, k
w	Concentration of free ions in chapter I (mol/cm^3)
x	Concentration of hydroxide ion generated in the acid reaction (mol/cm^3)
x_1	Distance of the IHP from the electrode surface (cm)
x_2	Distance of the OHP from the electrode surface (cm)
y	Concentration of hydronium ion generated in the base reaction (mol/cm^3)
z	Charge number
	Perpendicular coordinate (Chapter II)
$Z(k)$	Dimensionless current at time counter, k
Z_p	Dimensionless peak current
Z_{ss}	Dimensionless steady state current
α	electron transfer coefficient
β	exponential coefficient in EESG method
ε	Dielectric constant
	Porosity in membrane $Nr_o^2\pi$ (Chapter II)
ε_o	Permittivity of free space ($C^2N^{-1}m^{-2}$)
κ_{Naf}	Partition coefficient of the redox species in Nafion
κ_{wall}	Partition coefficient of the redox species along the wall of the composite
κ^{-1}	Debye length
ϕ'	Absolute electrostatic potential (V)
ϕ_o	Total potential drop across the solution side of the double layer (V)
ϕ_s	Potential at the OHP with respect to bulk solution (V)
δ	Diffusion length (cm) $\delta = (2Dt)^{1/2}$
	Thickness of adsorbed layer in chapter I (cm)
	thickness of the wall zone of the composite (cm)

$\tau(k)$	Dimensionless time at time counter, k
υ	Scan rate (V/s)
	Kinetic viscosity (cm^2/s)
ω	Angular frequency of rotation; 2π x rotation rate (s^{-1})